

UNCLASSIFIED

AD NUMBER

AD867179

LIMITATION CHANGES

TO:

Approved for public release; distribution is unlimited.

FROM:

Distribution authorized to U.S. Gov't. agencies and their contractors; Critical Technology; JAN 1970. Other requests shall be referred to U.S. Army Aviation Materiel Laboratories, Fort Eustis, VA 23604. This document contains export-controlled technical data.

AUTHORITY

USAAMRDL ltr, 23 Jun 1971

THIS PAGE IS UNCLASSIFIED

AD

AD 867179

USAALABS TECHNICAL REPORT 69-91

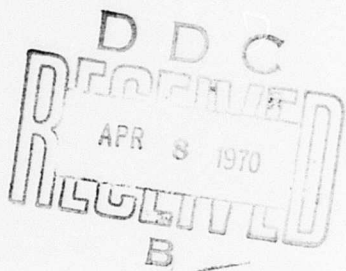
AN INVESTIGATION OF TURBINE BLADE/DISK ATTACHMENT METHODS FOR SMALL, COOLED GAS TURBINES

By

J. L. Helmbrecht

R. F. Kirby

F. Weber



January 1970

U. S. ARMY AVIATION MATERIEL LABORATORIES
FORT EUSTIS, VIRGINIA

CONTRACT DA AJ02-68-C-0119
THE AIRESEARCH MANUFACTURING
COMPANY OF ARIZONA
PHOENIX, ARIZONA

This document is subject to special export controls, and each transmittal to foreign governments or foreign nationals may be made only with prior approval of US Army Aviation Materiel Laboratories, Fort Eustis, Virginia 23604.



Reproduced by the
CLEARINGHOUSE
for Federal Scientific & Technical
Information Springfield Va. 22151

188

Disclaimers

The findings in this report are not to be construed as an official Department of the Army position unless so designated by other authorized documents.

When Government drawings, specifications, or other data are used for any purpose other than in connection with a definitely related Government procurement operation, the United States Government thereby incurs no responsibility nor any obligation whatsoever; and the fact that the Government may have formulated, furnished, or in any way supplied the said drawings, specifications, or other data is not to be regarded by implication or otherwise as in any manner licensing the holder or any other person or corporation, or conveying any rights or permission, to manufacture, use, or sell any patented invention that may in any way be related thereto.

Trade names cited in this report do not constitute an official endorsement or approval of the use of such commercial hardware or software.

Disposition Instructions

Destroy this report when no longer needed. Do not return it to the originator.



DEPARTMENT OF THE ARMY
U. S. ARMY AVIATION MATERIEL LABORATORIES
FORT EUSTIS, VIRGINIA 23604

The research described herein was conducted by the AiResearch Manufacturing Company of Arizona under the terms of Contract DAAJ02-68-C-0119. The work was performed under the technical management of Mr Edward T. Johnson, Propulsion Division, U.S. Army Aviation Materiel Laboratories.

The object of this research effort was the investigation, through analytical studies and experimental testing, of several blade-to-disk attachment concepts and airfoil shell-to-strut attachment concepts to determine the optimum concept for use on future small, high-temperature turbine rotors.

Appropriate technical personnel of the U.S. Army Aviation Materiel Laboratories have reviewed this report and concur with the conclusions contained herein.

The findings and recommendations outlined herein will be taken into consideration in the planning of future axial turbine programs.

Task 1G162203D14413
Contract DAAJ02-68-C-0119
USAALABS Technical Report 69-91
January 1970

**AN INVESTIGATION OF TURBINE BLADE/DISK ATTACHMENT
METHODS FOR SMALL, COOLED GAS TURBINES**

Final Report

By

**J. L. Helmbrecht
R. F. Kirby
F. Weber**

Prepared by

**The AiResearch Manufacturing
Company of Arizona
Phoenix, Arizona**

for

**U.S. ARMY AVIATION MATERIEL LABORATORIES
FORT EUSTIS, VIRGINIA**

This document is subject to special export controls, and each trans-
mittal to foreign governments or foreign nationals may be made only
with prior approval of US Army Aviation Materiel Laboratories,
Fort Eustis, Virginia 23604.

ABSTRACT

This report describes the analytical, experimental, and developmental efforts that were conducted to design, fabricate, test, and evaluate turbine-rotor blade to rotor disk (blade/disk) attachment methods for an air-cooled turbine rotor in a small gas turbine engine. This investigation was launched because the combination of factors that are necessary to satisfy the design requirements of a small cooled gas turbine has made it increasingly difficult to utilize conventional blade attachment means. Specifically, the program was directed toward achieving a suitable attachment method for an axial turbine with an inlet temperature of 2400°F, an airflow rate of 4.0 lb/sec, a tip speed of 1500 ft/sec, and matched to a compressor having a 10:1 pressure ratio.

Detailed aerothermodynamic design activities were conducted to determine a turbine design that would provide optimum specific fuel consumption (SFC) and specific horsepower (sp hp). The design included an optimization study to obtain the best compromise of turbine efficiency, cooling geometry, blade and disk stress effects, and fabrication considerations.

Detailed mechanical design activities were conducted in parallel with fabrication technology development efforts to establish the materials, designs, joining methods, and fabrication techniques necessary to determine feasible means of blade/disk attachment. Results of these activities showed that diffusion-bonding, brazing, and electron-beam-welding blade/disk attachment methods possess the greatest potential for application in the subject turbine design.

A secondary purpose of the mechanical design and fabrication development activities was to study the feasibility of developing the strut-supported sheet metal blade (shell/strut attachment) that was revealed by the aerodynamic optimization study to be the most effective blade cooling configuration. Full evaluation of the shell/strut attachment was beyond the scope of this program; however, it was determined that both diffusion-bonding and cast-bonding concepts of joining could be considered as feasible methods to develop for the purpose of shell/strut attachment.

A final fabrication and test activity was conducted to complete evaluations of the three blade/disk attachment methods. Final specimens were designed, fabricated, inspected, and subjected to tensile, stress-rupture, and low-cycle fatigue testing at 1200°F.

Evaluation of the final specimen test results revealed that (a) the diffusion-bonding method of joining was unsatisfactory for blade/disk attachment due to insufficient joint strength, (b) the brazing method of joining produced a joint strength approaching design requirements and could be considered as a candidate method for rotational test evaluation, and (c) the electron-beam-welding method of joining produced a joint strength that exceeded design requirements. Further evaluation will be necessary to resolve microcracking in the weld joint before rotational test evaluations can be considered.

FOREWORD

This final report describes a turbine blade/disk fabrication investigation that was conducted in fulfillment of Contract DAAJ02-68-C-0119, Task 1G162203D14413. The investigation was performed by the AiResearch Manufacturing Company of Arizona, a division of The Garrett Corporation, under the control of the United States Army Aviation Materiel Laboratories (USAAVLABS), Fort Eustis, Virginia.

The engineering project that implemented this program was the Propulsion-Engine Advanced Technology Project headed by F. Weber. The program manager, responsible to Mr. Weber, was J. L. Helmbrecht. Additional investigators were G. W. Bowers, Dr. R. F. Kirby, J. A. Pyne, R. H. Sargent, Dr. W. F. Waterman, and A. E. Wilson. In addition, the guidance of Mr. E. Johnson of USAAVLABS is gratefully acknowledged.

TABLE OF CONTENTS

	<u>Page</u>
SUMMARY	iii
FOREWORD	v
LIST OF ILLUSTRATIONS	x
LIST OF TABLES	xvii
LIST OF SYMBOLS	xix
1. INTRODUCTION	1
1.1 Problem Statement	1
1.2 Approach	3
2. AEROTHERMODYNAMIC DESIGN	4
2.1 Optimization Study	4
2.1.1 Cycle Analysis	4
2.1.2 Cooling Considerations	6
2.1.2.1 Vane Band Film Cooling	8
2.1.2.2 Vane Cooling - Internal	8
2.1.2.3 Blade Cooling - Internal	8
2.1.2.4 Disk Cooling, Impingement, and Radial Flow	11
2.1.2.5 Shroud Cooling	11
2.1.3 Analysis Technique and Optimization Procedure	11
2.1.4 Results of Optimization Study	18
2.1.4.1 Phase I	18
2.1.4.2 Phase II	21
2.1.4.3 Phase III	21
2.1.5 Design Selection	25
2.2 Aerodynamic Design	27
2.2.1 Stage Efficiency Analysis	29
2.2.2 Detailed Blading Design and Analysis	33
2.2.2.1 Stator	34
2.2.2.2 Rotor	37
3. MECHANICAL DESIGN AND ANALYSIS	38
3.1 Mechanical-Design Objectives	38
3.2 Final Design of Blade	39
3.2.1 Final Cooling Configuration	40
3.2.2 Blade Heat-Transfer Analysis	42
3.2.3 Blade Stress Analysis	43

	<u>Page</u>
3.3 Blade/Disk Attachment Concepts	47
3.3.1 Mechanical Concepts	48
3.3.2 Diffusion Bonding	53
3.3.3 Brazing	56
3.3.4 Electron-Beam Welding	58
3.4 Turbine Rotor Design	61
3.4.1 Rotor Temperature Distribution	62
3.4.2 Stress Analysis	64
 4. FABRICATION TECHNOLOGY DEVELOPMENT	71
4.1 Selection of Materials	72
4.1.1 Disk Materials	72
4.1.2 Strut Materials	72
4.1.3 Sheet Metal Blade Materials	72
4.2 Preliminary Test Evaluations	77
4.2.1 Diffusion Bonding	77
4.2.1.1 Experimental Procedure	77
4.2.1.2 Test Results and Conclusions	78
4.2.2 Brazing	88
4.2.2.1 Experimental Procedure	88
4.2.2.2 Test Results and Conclusions	88
4.2.3 Electron-Beam Welding	96
4.2.3.1 Experimental Procedure	96
4.2.3.2 Test Results and Conclusions	96
4.2.4 Cast Bonding	106
4.2.4.1 Experimental Procedure	106
4.2.4.2 Test Results and Conclusions	107
4.3 Selection of Final Candidate Joining Processes	114
4.3.1 Strut/Disk Attachment	114
4.3.2 Shell/Strut Attachment (Feasibility Study)	114
 5. FINAL SPECIMEN FABRICATION AND TESTING	115
5.1 Specimen Design	115
5.1.1 Diffusion-Bonded Specimen Design	115
5.1.2 Braze Specimen Design	117
5.1.3 Electron-Beam-Welded Specimen Design	117
5.2 Specimen Fabrication	120
5.2.1 Diffusion-Bonded Specimen Fabrication	122
5.2.2 Braze Specimen Fabrication	127
5.2.3 Electron-Beam-Welded Specimen Fabrication	131
5.3 Inspection of Final Specimens	138
5.3.1 Diffusion-Bonded Specimens	138
5.3.2 Braze Specimens	138
5.3.3 Electron-Beam-Welded Specimens	141

	<u>Page</u>
5.4 Final Specimen Testing	145
5.4.1 Tensile Testing	145
5.4.2 Stress-Rupture Testing	149
5.4.3 Low-Cycle Fatigue Testing	154
6. CONCLUSIONS	158
7. RECOMMENDATIONS	161
8. LITERATURE CITED	162
APPENDIX -- LITERATURE SURVEY	163
DISTRIBUTION	166

LIST OF ILLUSTRATIONS

<u>Figure</u>		<u>Page</u>
1	Turbine Stage Cooling	7
2	Candidate Stator-Vane Cooling Configurations	9
3	Candidate Rotor-Blade Cooling Configurations	10
4	Assumed Combustor Radial Profile	16
5	Blade Cross-Section Area Distribution . .	16
6	Phase I Results of Optimization Study . .	19
7	Phase II Results of Optimization Study .	22
8	Phase III Results of Optimization Study .	24
9	Effects of Stator- and Rotor-Cooling and Increased Blade Taper	26
10	Turbine Vector Diagrams	28
11	Turbine Meridional Flow Path	29
12	Local Loss Characteristics	31
13	Stage Efficiency Versus Hub-Tip Ratio . .	31
14	Overall Stage Efficiency	31
15	Vane Channel Velocity Distribution . .	35
16	Blade Channel Velocity Distribution . .	36
17	Chordwise-Flow Blade Configuration . .	41
18	Blade Metal Temperatures for Chordwise Flow Configuration	44
19	Gas Profile and Estimated Average Strut Temperature	45
20	Centrifugal Stress Distribution of Blade .	45

<u>Figure</u>		<u>Page</u>
21	Comparison of MAR-M 246 and IN-100 Rupture Strength	46
22	MAR-M 246 Stress-Rupture Life	46
23	Stress Locations of Fir-Tree Disk Attachment Design	50
24	Diffusion-Bonded Design	54
25	Brazed-Joint Design	57
26	Electron-Beam-Welded Design	60
27	Rotor Isotherms, Diffusion-Bonded Design	63
28	Rotor Isotherms, Brazed Design	63
29	Rotor Isotherms, Electron Beam Welded Design	63
30	Nominal Centrifugal Stress Distribution for Diffusion-Bonded Design	65
31	Nominal Centrifugal Stress Distribution for Brazed-Joint Design	66
32	Nominal Centrifugal Stress Distribution for Electron-Beam-Welded Design	67
33	Ultimate Tensile Strengths for Candidate Materials	74
34	Yield Strengths (0.2% Offset) for Candidate Materials	75
35	1000-Hr Stress-Rupture Strengths for Candidate Materials	76
36	Pressing Die and Plunger Arrangement Used for Diffusion Bonding of Sheet Specimens .	79
37	Vacuum Hot Press Furnace Used for Fabrication of Diffusion-Bonded Specimens	80
38	Test Fixture Used to Shear Test Diffusion-Bonded and Cast-Bonded Overlap Specimens .	81

<u>Figure</u>		<u>Page</u>
39	Diffusion-Bonding Specimen (Final Test Size)	86
40	Die Used for Diffusion Bonding of Figure 39 Specimens	86
41	Diffusion-Bonded Specimens Simulating the Final Test Design	87
42	Typical Diffusion-Bonded Joint Produced With Parameters Selected for Final Test Specimens	87
43	Brazing Test Specimen	90
44	Fixture Used During Tack Welding of the Brazing Specimens	91
45	Brazing Specimens Before (Top) and After (Bottom) Final Machining	91
46	Typical Failed Joint Between Inconel 718 and MAR-M 246 With Nicrobraz 150 Brazing Alloy	93
47	Typical Failed Joint Between Inconel 718 and MAR-M 246 With Nicrobraz 30 Brazing Alloy	93
48	Typical Failed Joint Between Inconel 718 and MAR-M 246 With Palniro 49TX Brazing Alloy	94
49	Stress-Rupture Data for Nicrobraz 30 Brazed Joints	95
50	Electron-Beam-Welding Test Specimens . . .	98
51	Electron-Beam-Welding Specimen After Welding and After Final Machining . . .	99
52	Preliminary Electron-Beam-Welding Specimens (Half-Size)	99
53	Typical Cracks in Electron-Beam Welds Joining AF2-1DA to MAR-M 246	100
54	Electron-Beam-Welded Joint Produced by Welding From Both Sides	104

<u>Figure</u>		<u>Page</u>
55	Electron-Beam-Welded Joint Produced by Welding From Both Sides	104
56	Single-Pass Electron-Beam-Welded Joint Developed for the Final Weld Specimens	105
57	Example of the Minimum Amount of Cracking Achieved in Specimens Simulating Final Test Specimens. The Material Combination is MAR-M 246/Waspaloy	105
58	Die Arrangement for Forming Cast-Bonding Test Specimens	108
59	Die Arrangement and Specimen Produced by Cast Bonding With Preplaced Molybdenum Wires	109
60	Vacuum Induction Furnace	110
61	Photomicrograph of the Interface of a Cast Bond Showing Cracking in the Cast Material Typical of That Resulting from Insufficient Preheat of the Sheet Material	111
62	Examples of Cast-Bonded Joints Produced Using Final Casting Parameters	112
63	Diffusion-Bonded Final Specimen Design .	116
64	Brazed Final Specimen Design	118
65	Electron-Beam-Welded Final Specimen Design	119
66	Machined Diffusion-Bond Final Specimen Elements Before Assembly	123
67	Diffusion-Bonded Final Specimen Assembled in Vice With Shim Installed Prior to Tack Welding	124
68	Diffusion-Bonded Final Specimen With Shim Removed and Tack Welding Complete . . .	124

<u>Figure</u>		<u>Page</u>
69	Two Views of the Graphite Die Assembly Used During the Diffusion Bonding Operation on the Final Specimen	125
70	Diffusion-Bonded Final Specimen After Completion of Bonding Operation and Final Machining	126
71	Clevis Assembly Used for Testing of the Diffusion-Bonded Specimens	126
72	Component Parts of the Brazed Final Specimen After Final Machining	128
73	Assembly Jig With the Brazed Final Specimen in Place	128
74	Spacers Tack-Welded in Place on Brazed Final Specimen	129
75	Final Specimen After Completion of Braze Operation	129
76	Brazed Final Specimen Ready for Testing (Spacers Have Been Cut)	130
77	Machined Waspaloy Block That Simulated the Disk Element of the Electron-Beam-Welded Final Specimen	133
78	Section Through Single-Pass Weld of Electron- Beam-Welded Final Specimen Disk Element .	133
79	Elements of Electron-Beam-Welded Final Specimens Prior to Joining	134
80	Elements of Electron-Beam-Welded Final Specimens Clamped in Welding Jig	134
81	Electron-Beam-Welded Final Specimen With Backup Strip in Place	135
82	Front View of an Electron-Beam-Welded Final Specimen With Weld Backup Strip Removed	135
83	Back View of an Electron-Beam-Welded Final Specimen With Weld Backup Strip Removed	136

<u>Figure</u>		<u>Page</u>
84	Electron-Beam-Welded Final Specimen After Completion of Final Machining	136
85	Front View of Joint-Test Section of an Electron-Beam-Welded Final Specimen	137
86	Back View of Joint-Test Section of an Electron-Beam-Welded Final Specimen	137
87	Photomicrographs of a Typical Bonded Joint of a Diffusion-Bonded Final Specimen Showing No Defects	139
88	Photomicrographs of a Typical Bonded Joint of a Diffusion-Bonded Final Specimen Showing Defects	140
89	Photomicrograph of a Typical Joint of a Braze Final Specimen	141
90	Example of Indications Revealed by Dye-Penetrant Inspection of an Electron-Beam-Welded Final Specimen	142
91	Typical Weld Spike Produced in an Electron-Beam-Welded Final Specimen (Depth Penetration 0.790 Inch)	143
92	Typical Cracking at the Weld Zone Interface of an Electron-Beam-Welded Final Specimen	143
93	Photomicrograph of the Most Severe Cracking Found in an Electron-Beam-Welded Final Specimen	144
94	Tensile Failure of a Diffusion-Bonded Final Specimen	147
95	Tensile Failure of a Braze Final Specimen	147
96	Tensile Failure of Electron-Beam-Welded Final Specimen	148
97	Fracture Surfaces of Two Electron-Beam-Welded Final Specimens Showing Variation of Fracture Appearance in Tensile Failure	148

<u>Figure</u>		<u>Page</u>
98	Stress-Rupture Data Plotted as Stress Versus Rupture Time	151
99	Stress-Rupture Data Plotted as Load Versus Rupture Time	152
100	Typical Example of Fracture Surfaces Resulting From Stress Rupture Failure of Electron-Beam-Welded Final Specimen	153
101	Stress-Rupture Failure of Electron-Beam-Welded Final Specimen Showing Smooth Fracture Face Corresponding to Waspaloy/Weld Zone Interface	153
102	Low-Cycle Fatigue Failure Data for Three Types of Final Specimens	156
103	Two Modes of Low-Cycle Fatigue Failure of Brazed Final Specimens	157
104	Low-Cycle Fatigue Failure of Electron-Beam-Welded Final Specimen--Smooth Fracture Surface is Shown on Left and Coarse Fracture Surface is Shown on Right	157

LIST OF TABLES

<u>Table</u>		<u>Page</u>
I	Sequential Logic Flow Chart of the Conducted Program	2
II	Parameters Used in Cycle Analysis (Sea-Level, Standard Day)	5
III	Computer Program Flow Diagram for Cooled Turbine Design Optimization	12
IV	Optimization Study Phases	15
V	Design Point Input Parameters Common to All Three Study Phases	17
VI	Vector Diagram Conditions	30
VII	Fir-Tree Stress Summary	49
VIII	Summary of Safety Margins	52
IX	Weights, Polar Moments of Inertia, and Bore Widths for the Three Rotor Designs .	70
X	Nominal Chemical Compositions for Candidate Alloys	73
XI	Material Combinations Evaluated Initially for Diffusion-Bonded Joints	82
XII	Lap/Shear Tests of Diffusion-Bonded Specimens	83
XIII	Summary of Shear-Test Results on Diffusion-Bonded Specimens	85
XIV	Nominal Compositions of the Brazing Alloys Selected for Evaluation	89
XV	Stress-Rupture Data on Brazing Specimens .	92
XVI	Tensile Test Results of Electron-Beam-Welded Specimens	101
XVII	Summary of Tensile-Test Results on Electron-Beam-Welded Specimens	103

<u>Table</u>		<u>Page</u>
XVIII	Results of Shear Testing Cast-to-Sheet Bonded Specimens	113
XIX	Certified Compositions for Materials Used in the Final Test Specimens	121
XX	Electron-Beam-Welding Parameters Used for Final Test Specimens	132
XXI	Tensile Test Results	146
XXII	Stress-Rupture Test Results	150
XXIII	Fatigue Test Data	155

LIST OF SYMBOLS

A_o	external surface area, sq ft
acr'_2	sonic velocity (abs) rotor inlet, ft/sec
acr'_3	sonic velocity (abs) rotor exit, ft/sec
acr''	sonic velocity (rel) rotor exit, ft/sec
D_s	suction surface diffusion
D_p	pressure surface diffusion
F_{tu}	average ultimate tensile strength of disk material, psi
h_o	external film coefficient of heat transfer, Btu/hr-sq ft-°F
I_p	power moment of inertia, lb/in./sec ²
K	reaction ratio
K_c	tip clearance parameter, in.
N_B	burst speed, ft/sec
N_D	design speed, ft/sec
q_o	surface heat transfer, Btu/hr
T'_1	turbine inlet temperature, °F
T_{aw}	adiabatic wall temperature of gas, °F
T_c	coolant temperature, °F
T_w	wall temperature, °F
U_H	turbine hub speed, ft/sec
V	absolute velocity
V_u	tangential component of absolute velocity
W	compressor bleed flow, lb/sec
W_c	compressor through-flow, lb/sec

w_{hs}	stator hub shroud cooling flow, lb/sec
\bar{w}_r	rotor-cooling flow fraction of turbine inlet flow, lb/sec
\bar{w}_s	stator-cooling flow fraction of turbine inlet flow, lb/sec
w_{stator}	total stator-cooling flow, lb/sec
w_{ted}	stator trailing-edge discharge flow, lb/sec
w_{ts}	stator tip shroud cooling flow, lb/sec
w_t/w	total stage cooling flow
x	directed fraction of stator cooling
$\alpha_{2,H}$	stator hub exit-flow angle, deg
$\Delta H/\theta$	specific work, Btu/lb
ΔH_t	stage work, Btu/lb
η_{aero}	aerodynamic efficiency
η_{cool}	stage efficiency with cooling penalties
η_i^*	stage efficiency
η_T	turbine efficiency
$\theta_t/1m$	momentum thickness loss
λ_s	stage work coefficient
σ_B	blade root centrifugal stress, psi
σ_t	average tangential stress at design speed, psi
ϕ	hub-tip ratio

1. INTRODUCTION

This report describes a USAAVLABS-sponsored program that was directed to determine a suitable method of turbine blade/disk attachment. The program comprised four major efforts:

1. Aerothermodynamic Design
2. Mechanical Design and Analysis
3. Fabrication Technology Development
4. Final Specimen Fabrication and Testing

Table I presents a sequential logic flow chart that portrays the scope of the overall program that was conducted, shows the interrelationship of the individual activities, and in addition, lists the section number where appropriate discussion can be found in this report.

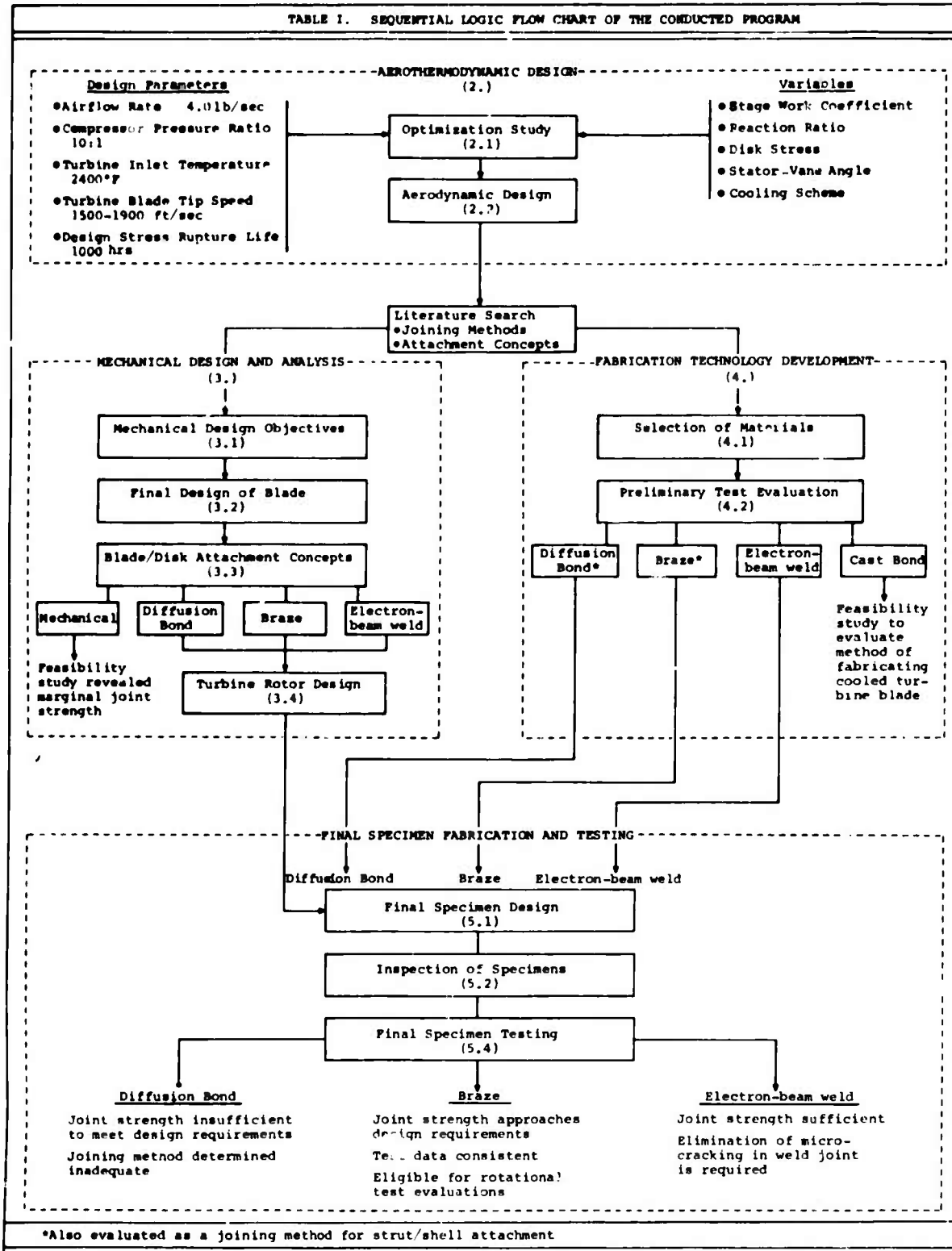
1.1 PROBLEM STATEMENT

The desire to obtain higher performance from small gas turbine engines has made it necessary to utilize air-cooled turbine components in order to realize the high cycle temperature required. Recent development activity in this area has revealed problems associated with small cooled turbines that have not been significant in the design of large cooled turbine components. The problem dealt with in this program involves the attachment of the turbine blade to the disk.

The high work requirement, the blade design compromises required to ensure adequate cooling of the small blades, and the requirement to maintain high efficiency are the basic factors associated with the attachment problem. These factors create a condition that requires high solidity, and hence, close blade spacing, combined with high stress levels in the attachment region.

To provide effective cooling of the blade leading edge, inlet relative Mach numbers must be reasonably low to lessen heat-transfer coefficients in the region of the stagnation point. This requirement dictates a high tip speed, and therefore, high blade-root and disk stresses in the attachment area.

TABLE I. SEQUENTIAL LOGIC FLOW CHART OF THE CONDUCTED PROGRAM



Additionally, relatively large trailing edges are usually required, either because of the geometry of the internal cooling passages, or because of the necessity to provide coolant discharge at the trailing edge or vicinity. The large trailing edges increase passage blockage, and to maintain blockage values at acceptable levels the blade pitch must be increased. This, however, is in opposition to the requirement of high solidity, and the only alternative is to increase the axial chord. Increased axial chord results in reduced blade aspect ratios that increase end wall and secondary flow losses. The relatively large chord and the high stresses in the attachment region combine to create a difficult attachment problem.

Use of a more conventional attachment, such as a fir tree, results in either excessively wide, and hence, heavy disks, or, depending upon the severity of factors involved, unacceptably low stress-rupture life for the attachment.

1.2 APPROACH

In view of the aforementioned difficulties, the technical approach that was taken by this program to evolve a suitable method of blade/disk attachment included:

1. An aerothermodynamic trade-off study to establish an optimized turbine design
2. A literature survey and analytical study to select several candidate turbine blade/disk attachment concepts and joining processes
3. Experimentation to determine and refine the most acceptable attachment method(s) from the selected candidates
4. Testing to substantiate the integrity of the final refined attachment method(s)

2. AEROTHERMODYNAMIC DESIGN

To make a realistic evaluation of the turbine blade/disk attachment, it is first necessary to generate a blade design that incorporates geometry consistent with the aerothermodynamic requirements of the assumed turbine. For the small air-cooled turbine, realization of high efficiency values becomes difficult because of blade design compromises dictated by cooling-geometry requirements.

The objective of the aerothermodynamic design activity was to establish a small air-cooled axial-flow turbine design optimized to obtain the best balance between the lowest possible specific fuel consumption (SFC) and the highest possible specific horsepower (sp hp). To accomplish this goal, an extensive study was conducted to determine the best compromise of (a) turbine efficiency, (b) cooling geometry and hence cooling airflow rate, (c) blade stress, (d) disk stress, and (e) blade/disk fabrication considerations.

The single-stage axial-flow turbine analyzed was assumed to drive the compressor in a small gas turbine engine having a free power turbine. Design-point parameters were as follows:

1. Airflow rate	4.0 lb/sec
2. Compressor pressure ratio	10:1
3. Turbine inlet temperature	2400°F
4. Turbine adiabatic efficiency (goal)	0.83 - 0.85
5. Turbine tip speed	1500-1900 ft/sec
6. Stress-rupture life	1000 hr

2.1 OPTIMIZATION STUDY

The optimization study was initiated by a cycle analysis of the engine in which the turbine component was assumed to have application.

2.1.1 Cycle Analysis

The basic turbine configuration assumed for the cycle analysis included a single-stage gas generator turbine with the capability of driving a 10:1 pressure ratio compressor having an airflow rate of 4 lb/sec. (Either a single- or two-stage free-power turbine can be assumed downstream of the gas generator.) It was assumed that the power turbine design would be

selected so that no blade or vane cooling would be required.

Specific cycle parameters used in the analysis are shown in Table II. As indicated in Table II, the cycle analysis was undertaken for constant cycle pressure and temperature ratio over a range of compressor bleed fractions and gas generator turbine efficiencies.

TABLE II. PARAMETERS USED IN CYCLE ANALYSIS
(SEA-LEVEL STANDARD DAY)

Type	Value
Turbine inlet temperature, °F	2400
Compressor pressure ratio	10.0
Compressor airflow, lb/sec	4.0
Compressor efficiency	0.80
Compressor bleed flow for turbine cooling, lb/sec	Variable
Combustor efficiency	0.98
Combustor loss - $\Delta P/P$	0.05
Cycle leakage	0.0
Lower heating value of fuel - Btu/lb	18,400
Gas generator turbine efficiency	Variable
Interstage duct loss - $\Delta P/P$	0.02
Power turbine efficiency (total-to-static)	0.87
Mechanical efficiency	0.98
Accessory horsepower	0.0

It was assumed that the compressor bleed air used for cooling the gas generator turbine re-enters the mainstream gas flow ahead of the power turbine.

The relationship of SFC and sp hp versus compressor bleed fraction (W/W_C) for various values of turbine efficiency (η_T) was determined. With the turbine design assumed to be in the region of $\eta_T = 0.84$ and $W/W_C = 0.12$, the following influence coefficients were found to prevail:

$$\frac{\Delta SFC/SFC}{\Delta \eta_T \eta_T} W/W_C = -0.89 \quad (1)$$

$$\frac{\Delta W/W_C}{\Delta \eta_T \eta_T} SFC = 1.30 \quad (2)$$

$$\frac{\Delta sp\ hp/sp\ hp}{\Delta \eta_T \eta_T} W/W_C = 0.95 \quad (3)$$

$$\frac{\Delta W/W_C}{\Delta \eta_T \eta_T} sp\ hp = 0.51 \quad (4)$$

These partial derivatives indicated the relative importance of gas generator turbine efficiency and cooling flow for maintaining a given SFC or sp hp. Thus, a favorable trade-off in SFC can be achieved if cooling-flow requirements do not increase more rapidly than 1.3 times the turbine efficiency increase for a given design change. Similarly, an increase in sp hp can be realized if the cooling requirement does not increase more rapidly than 0.51 times the turbine efficiency increase.

2.1.2 Cooling Considerations

To perform the optimization study, existing analysis procedures and computer programs were used where available; however, analysis procedures and subroutines had to be written so that turbine cooling-flow requirements could be included in the study. Procedures were written to provide an estimation of cooling-flow requirements for the turbine stage as shown in Figure 1.

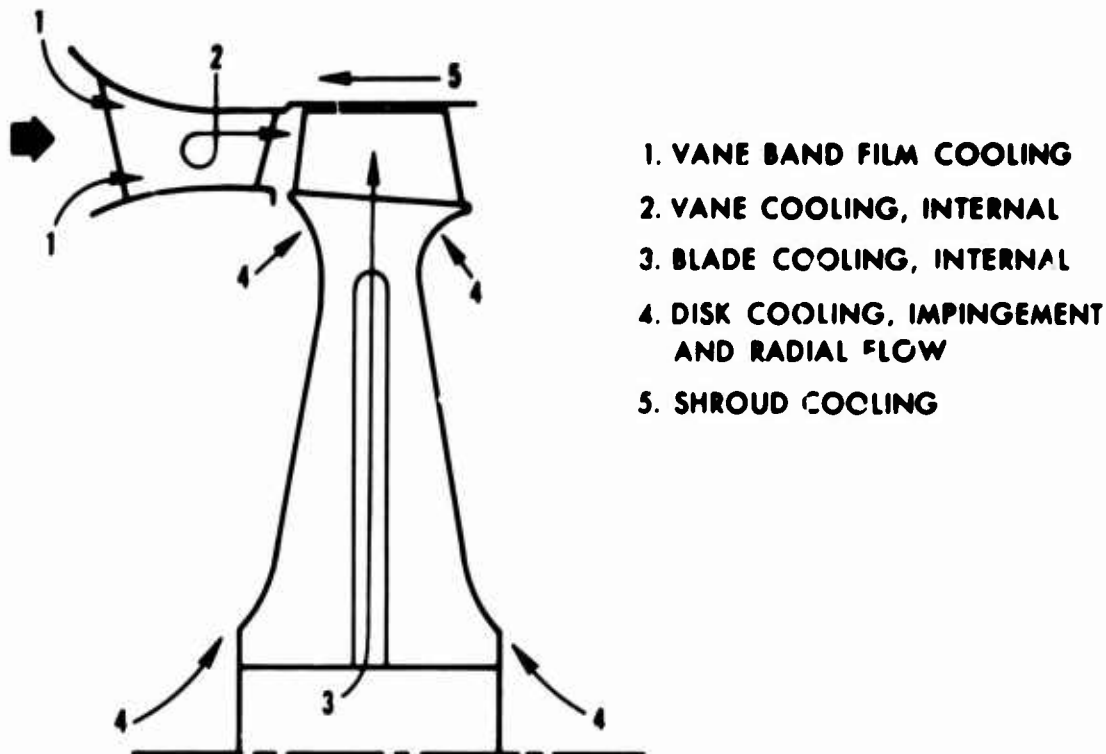


Figure 1. Turbine Stage Cooling.

An adequate description of heat transfer to the surface is needed to determine the cooled-component coolant flow requirement. In general, heat transfer to the surface, q_o , may be written as

$$q_o = h_o A_o (T_{aw} - T_w) \quad (5)$$

where h_o = the external film coefficient of heat transfer

A_o = the external surface area

T_{aw} = the adiabatic wall temperature of the gas

T_w = the wall temperature

The routines were written such that the coolant flow rate was determined iteratively by matching desired and actual wall temperatures. The desired wall temperature was determined from both stress considerations and material oxidation limits. The adiabatic wall temperature included the effects of both radial- and circumferential-temperature profiles, as required. The external film coefficient and surface area were computed in the turbine sizing routine. The turbine stage cooling

considerations contain approximations which, while believed to be realistic, require detailed design and subsequent experimental confirmation. Brief descriptions of the turbine stage cooling considerations are presented in subsequent paragraphs.

2.1.2.1 Vane Band Film Cooling

Vane bands are most readily cooled to acceptable oxidation limit values by use of film-cooling techniques. In film cooling, the coolant is injected into the main gas stream in a direction essentially tangent to the surface to be cooled.

The required adiabatic wall temperature with film cooling was based upon a relation derived from an equivalence of external and internal heat-transfer rates on the film-cooled surface. Values for internal film coefficients were chosen to be consistent with moderate cold-side cooling. The external film coefficient was computed from the turbulent flat-plate, heat-transfer correlation. The film-cooling flow rate was then computed from these quantities and a film-cooling correlation.

2.1.2.2 Vane Cooling - Internal

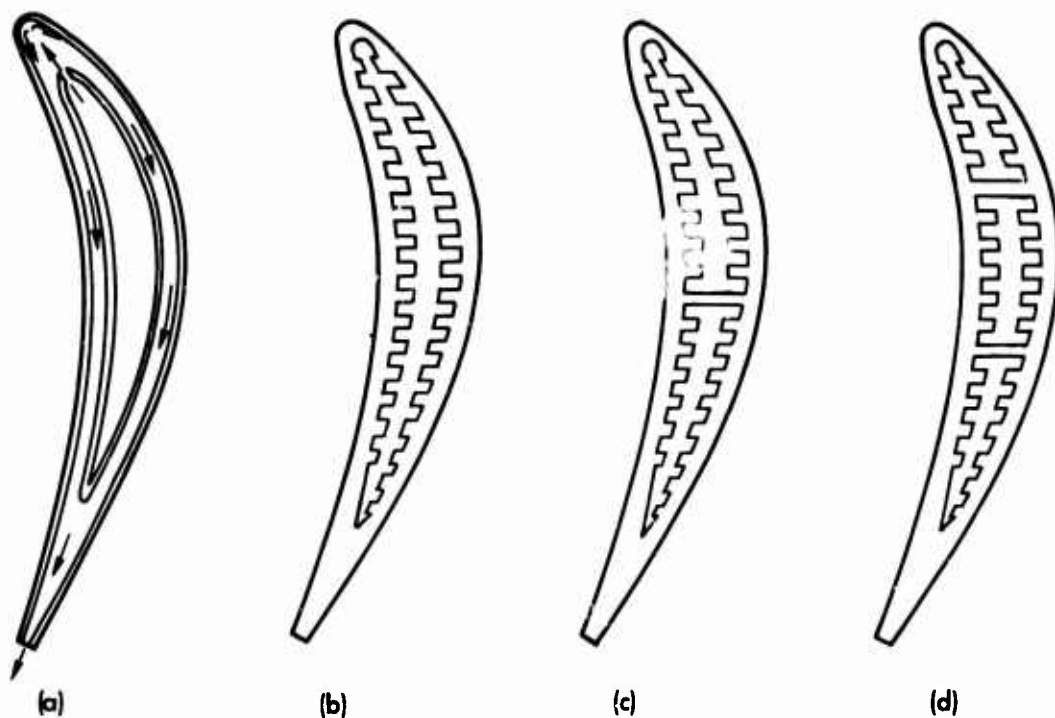
Procedures were written and programmed to define four different stator-vane cooling configurations. Those considered are shown schematically in Figure 2. Where possible, realistic geometric approximations for each of the four stator-vane cooling configurations were based on existing designs.

To prevent the occurrence of difficult cooling problems associated with small leading-edge diameters and large values for external film coefficients, a check was incorporated in the program to warn against external film coefficients exceeding 1000 Btu/hr-sq ft-°F. Wall temperature was controlled as a function of the oxidation limit of the selected vane material. The coolant flow rate required was compared with choking conditions at the discharge of the vane.

2.1.2.3 Blade Cooling - Internal

Procedures were written and programmed to define four different rotor-blade cooling configurations. Those considered are shown schematically in Figure 3.

Comments regarding the stator analysis are applicable to the rotor except that the discussion on wall temperature applies to the sheet metal shell at the tip and at the trailing edge in Configuration (a) only. The metal temperatures of the other blade configurations and of the strut of Configuration (a) were controlled by matching wall temperature with allowable temperature consistent with 1000-hour stress-rupture life characteristics of the selected blade material.



CONFIGURATION (a) :

IMPINGEMENT-COOLED LEADING EDGE
CHORDWISE FLOW IN MID-CHORD REGION
TRAILING-EDGE COOLANT DISCHARGE

CONFIGURATION (b) :

SINGLE-PASS RADIAL FLOW

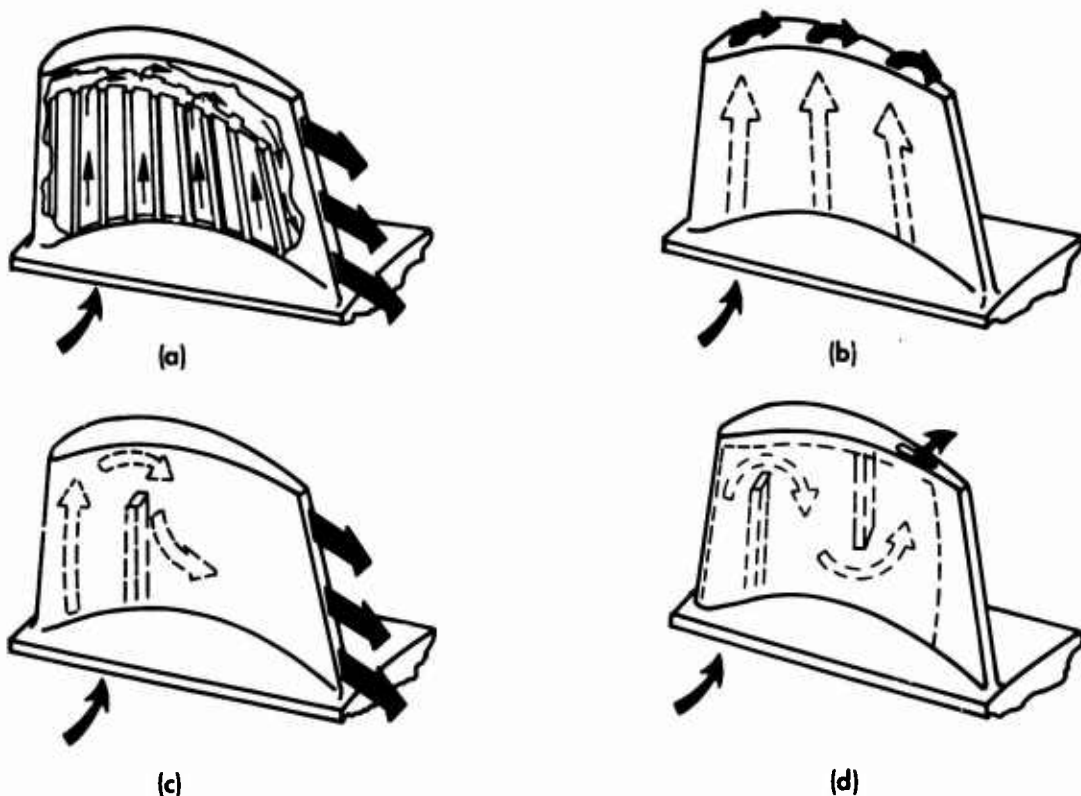
CONFIGURATION (c) :

TWO-PASS RADIAL FLOW
TIP COOLANT DISCHARGE

CONFIGURATION (d) :

THREE-PASS RADIAL FLOW
COOLANT DISCHARGE AT INNER BAND

Figure 2. Candidate Stator-Vane Cooling Configurations.



CONFIGURATION (a) :

- STRUT-SUPPORTED SHEET METAL SHELL
- RADIAL FLOW
- TRAILING-EDGE COOLANT DISCHARGE

CONFIGURATION (b) :

- SINGLE-PASS RADIAL FLOW

CONFIGURATION (c) :

- TWO-PASS RADIAL FLOW

CONFIGURATION (d) :

- THREE-PASS RADIAL FLOW

Figure 3. Candidate Rotor-Blade Cooling Configurations.

2.1.2.4 Disk Cooling, Impingement, and Radial Flow

Disk cooling included both impingement cooling at the rim and radial flow. For radial flow cooling, a seal was assumed to exist at 80 percent of the rim radius. The coolant flow rate was taken as equal to the pumping flow for this portion of the disk. This was based on the assumption that these conditions will tend to prevent hot-gas recirculation from the mainstream along the sides of the disk.

2.1.2.5 Shroud Cooling

The blade shroud is exposed to an environment similar to that of the film-cooled outer vane band. Procedures were written to provide geometric approximations of an axial-flow scheme for cooling this component. Wall temperature was controlled as a function of the oxidation limit of the material.

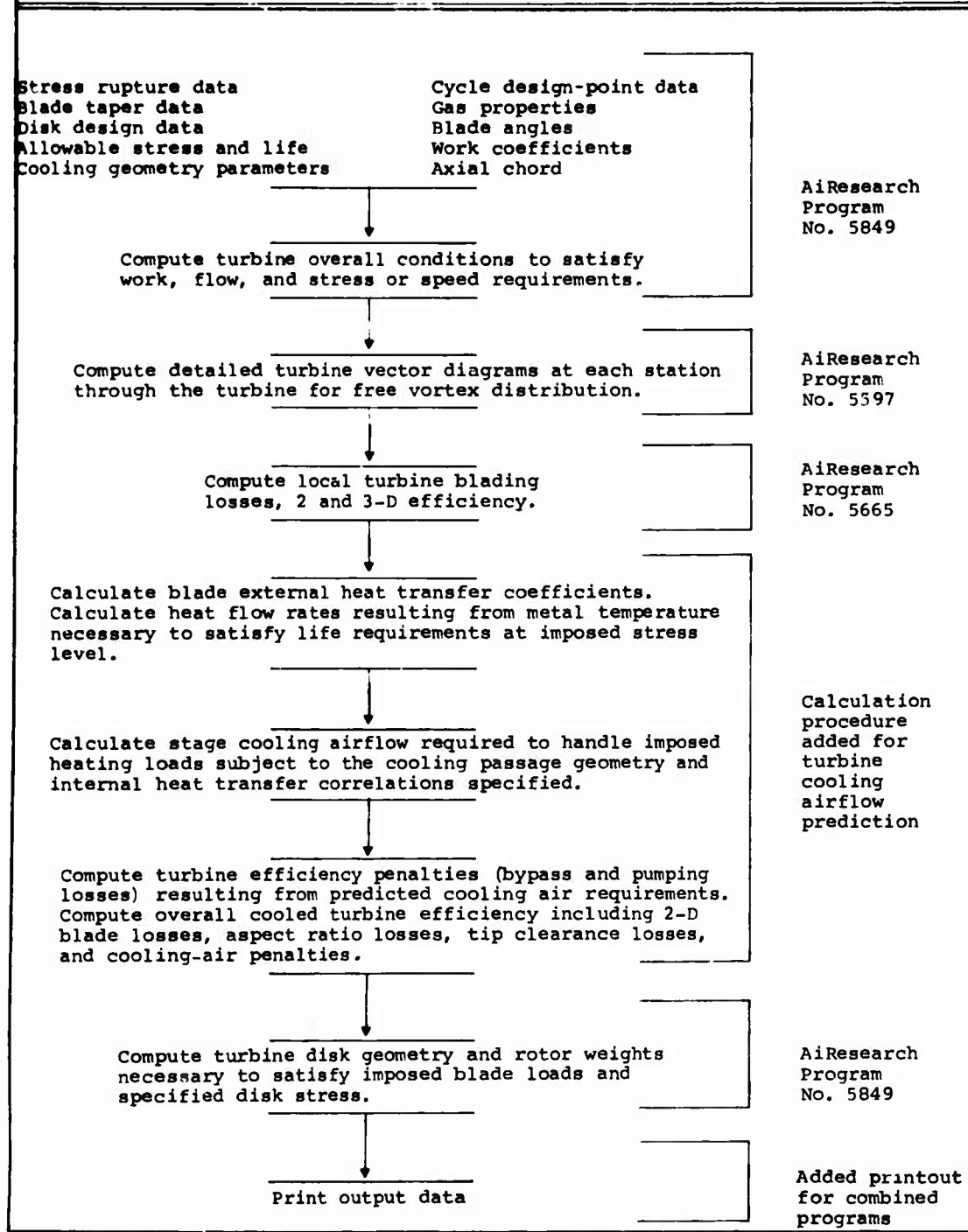
2.1.3 Analysis Technique and Optimization Procedure

The analysis method utilized for the optimization study was developed by combining existing programs with new subroutines that were written to account for the effect of the turbine stage cooling considerations. Table III, the computer program flow diagram, shows (a) the existing programs that were used to determine the basic turbine design parameters necessary to define the performance of an uncooled turbine, and (b) the new subroutines that were added to determine the effect of the turbine stage cooling considerations. Discussions of the new subroutines are presented in subsequent paragraphs.

Allowable metal temperatures in the rotor were computed as a function of radius from the local centrifugal stress level and life requirement by the use of the Larson-Miller curve input to the program. The imposed heating rate was then calculated with the use of the values of external film coefficient, adiabatic wall temperature, and surface area previously determined. The heating load was then used in the internal heat-transfer analysis to determine the cooling air-flow required to maintain, at steady state, the required wall temperatures.

Performance penalties resulting from the calculated cooling-flow requirements of stator and rotor were computed to accomplish this. A certain fraction, X , of the stator cooling-flow requirement was considered to be available to do work in the rotor, and hence, behaved as though there were no cooling-flow penalty for this portion of the stage cooling requirement. The fraction X , called the directed fraction of stator-cooling air, was defined as

TABLE III. COMPUTER PROGRAM FLOW DIAGRAM FOR
COOLFD TURBINE DESIGN OPTIMIZATION



$$X = \frac{W_{ts} + W_{hs} + W_{ted}}{W_{stator}} \frac{T_{c,in}}{T'_1} \quad (6)$$

where W_{ts} = stator tip shroud cooling flow
 W_{hs} = stator hub shroud cooling flow
 W_{ted} = stator trailing-edge discharge cooling flow (if applicable)
 W_{stator} = total stator-cooling requirement
 $T_{c,in}$ = coolant inlet temperature
 T'_1 = turbine inlet temperature

It was assumed that the remaining fraction ($1-X$) of the stator-cooling air and all of the rotor-cooling air were not available to do work in the rotor, and that pumping work must be done to enable the cooling air to flow through the rotor.

Applying these concepts to the power output of the cooled stage yielded the following expression:

$$\frac{HP_{cooled}}{HP_{uncooled}} = (1+X\bar{W}_s) - \frac{U_H^2}{gJ\Delta H_t} (1-X) \bar{W}_s + \bar{W}_r \quad (7)$$

where \bar{W}_s = stator-cooling flow fraction of turbine inlet flow
 \bar{W}_r = rotor-cooling flow fraction of turbine inlet flow
 ΔH_t = stage work per lb

It was apparent that this ratio may be greater or less than unity, depending on the relative amounts of stator- and rotor-cooling and on the turbine hub speed, U_H . For the purpose of analysis, this power ratio was assumed to be an efficiency ratio. Thus, the cooled turbine efficiency was calculated from

$$\eta_{cool} = \frac{HP_{cooled}}{HP_{uncooled}} \eta_{aero} \quad (8)$$

where η_{aero} = attainable turbine efficiency calculated previously

Note that η_{cool} is not a true efficiency in the thermodynamic sense, since the flow through the turbine is not constant during the expansion process. However, η_{cool} represents the work capacity of a cooled turbine relative to an uncooled turbine having the same inlet equivalent flow.

Calculating η_{cool} and $W/W_C = \bar{W}_s + \bar{W}_r$ is sufficient to determine the engine performance parameters of SFC and sp hp from the cycle study described previously.

As a final step in the calculation, the program computed a turbine disk design subject to the input design parameters and determined the average tangential disk stress and overall rotor weight.

The optimization procedure employed consisted of using the analysis technique described previously to determine η_{cool} and W/W_C for a wide range of turbine designs satisfying the input requirements. The values of cooled turbine efficiency and stage cooling flow fraction uniquely determine values of engine SFC and sp hp according to the cycle analysis. The optimum turbine configuration was considered to be the design that achieves the best balance between minimum SFC and maximum sp hp.

The study was divided into three phases, as summarized in Table IV. The first phase considered the effect of two primary independent variables:

1. Turbine stage work coefficient at the hub,

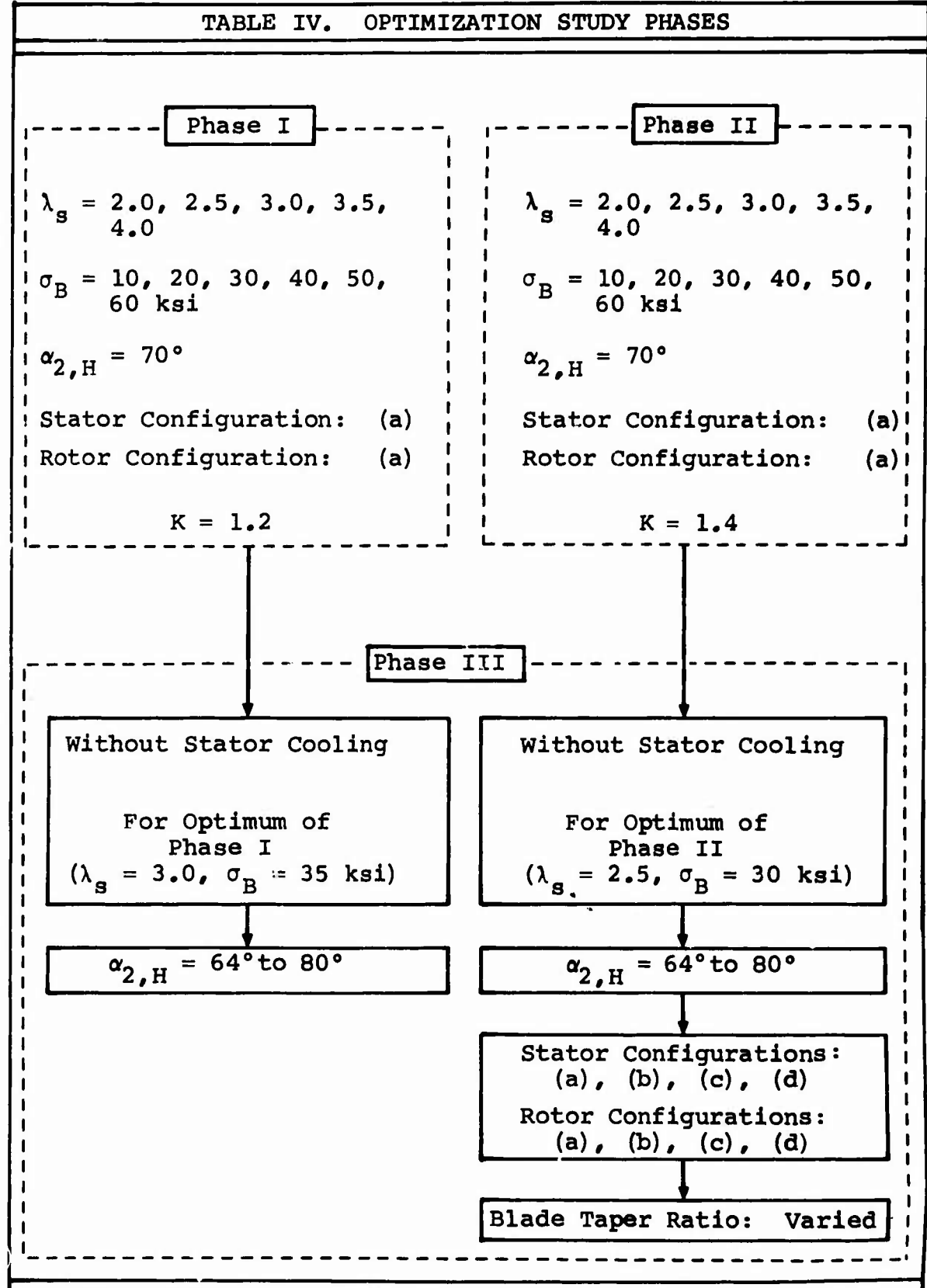
$$\lambda_s = \frac{V_u}{U_{2H}} - \frac{V_u}{U_{3H}} \quad (9)$$

2. Turbine blade root centrifugal stress based upon turbine exit annular area,

$$\sigma_B$$

In Phase II, the study of Phase I was repeated at a higher rotor hub reaction ratio K. Phase III considered the

TABLE IV. OPTIMIZATION STUDY PHASES



effects of additional variables while holding constant the optimum conditions derived from Phases I and II.

The first step in the optimization procedure was to select a design point with regard to turbine efficiency and compressor bleed flow. It was necessary that this design point lie in the range of the predicted efficiency level and cooling requirement so that the turbine work would match the compressor work. The design point selected was

$$\eta_{cool} = 0.84, \quad w/w_c = 0.10$$

The design-point input parameters that are common to all three phases are listed in Table V. Figure 4 shows the assumed combustor radial profile, and Figure 5 shows the blade cross-section area distribution, which was based upon previous turbine designs.

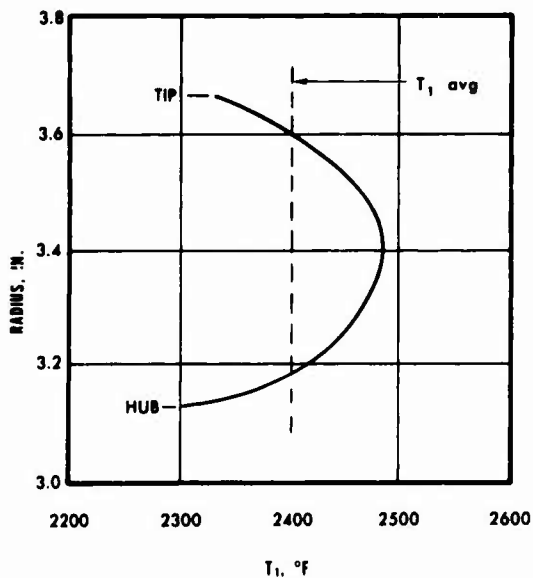


Figure 4. Assumed Combustor Radial Profile.

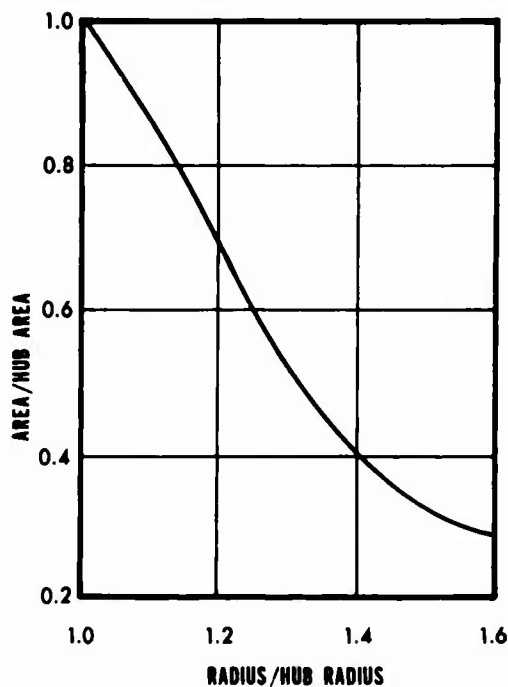


Figure 5. Blade Cross-Section Area Distribution.

TABLE V. DESIGN POINT INPUT PARAMETERS COMMON
TO ALL THREE STUDY PHASES

Parameter	Value
Inlet temperature - °F	2400
Specific work - Btu/lb	28.0
Adiabatic efficiency	0.88
Stage entropy split - $\Delta S_{\text{stator}} / \Delta S_{\text{stage}}$	1/3
Gas constant - Btu/lb-°R	53.399
Prandtl number	0.7
Pressure surface diffusion, stator	0.5
Pressure surface diffusion, rotor	0.5
Disk stress - psi	60,000
Material density, blade and disk - lb/cu ft	527.04
Wall temperature, stator - °F	2000*
Root conduction to disk - °F	-100
Coolant temperature rise (from source) - $\Delta T/T$	0.12
Disk taper angle - deg	15
Disk hole, radius - in.	0
Axial chord, stator vane tip - in.	1.0
Axial chord, rotor blade hub - in.	1.0
Trailing-edge thickness, stator - in.	0.04
Trailing-edge thickness, rotor - in.	0.04

*Except for Phase III (without stator cooling).

Values listed for blade axial chord and trailing-edge thickness resulted basically from fabrication and cooling considerations. As discussed later in the text, the blade and vane sheet metal thickness was selected to be 0.010 inch. To provide for sufficient area to discharge the coolant through the trailing edge, it was found that a passage width of approximately 0.020 inch would be required, including 20 percent blockage for internal structural members. Thus, the trailing-edge thickness becomes 0.040 inch ($0.010 + 0.010 + 0.020$ inch). Preliminary evaluations indicated that solidity requirements of the turbine design would require an axial chord of approximately 1.0 inch for the selected trailing-edge thickness if reasonable blockage values were maintained. This was verified by the optimization study.

2.1.4 Results of Optimization Study

The results of the optimization study are presented in the following subparagraphs. Twenty-five turbines were analyzed for the specified range of blade stress and hub work coefficients. The predicted values of η_{cool} and W/W_c are plotted on the SFC and sp hp graphs that were determined from the cycle analysis and are discussed and shown on the following pages.

2.1.4.1 Phase I

The first phase of the study as shown in Table IV was run at a reaction ratio, K , of 1.2 and considered hub work coefficient, λ_s , and blade root stress, σ_B , as primary independent variables.

The results of the Phase I study are presented in Figure 6, where λ_s and σ_B are plotted as parameters on the curves of SFC and sp hp versus W/W_c (determined from cycle analysis). Several important trends are apparent from these graphs:

1. The blade centrifugal stress level plays a dominant role in controlling rotor blade height, and, hence, turbine efficiency. This result is due to the strong effect of tip clearance-to-blade height ratio on rotor blade losses for turbines in this design equivalent flow range.
2. Both blade centrifugal stress level and stage work coefficient directly control turbine size (diameter). The curves indicated that turbine size was a significant factor in determining overall stage cooling requirements.

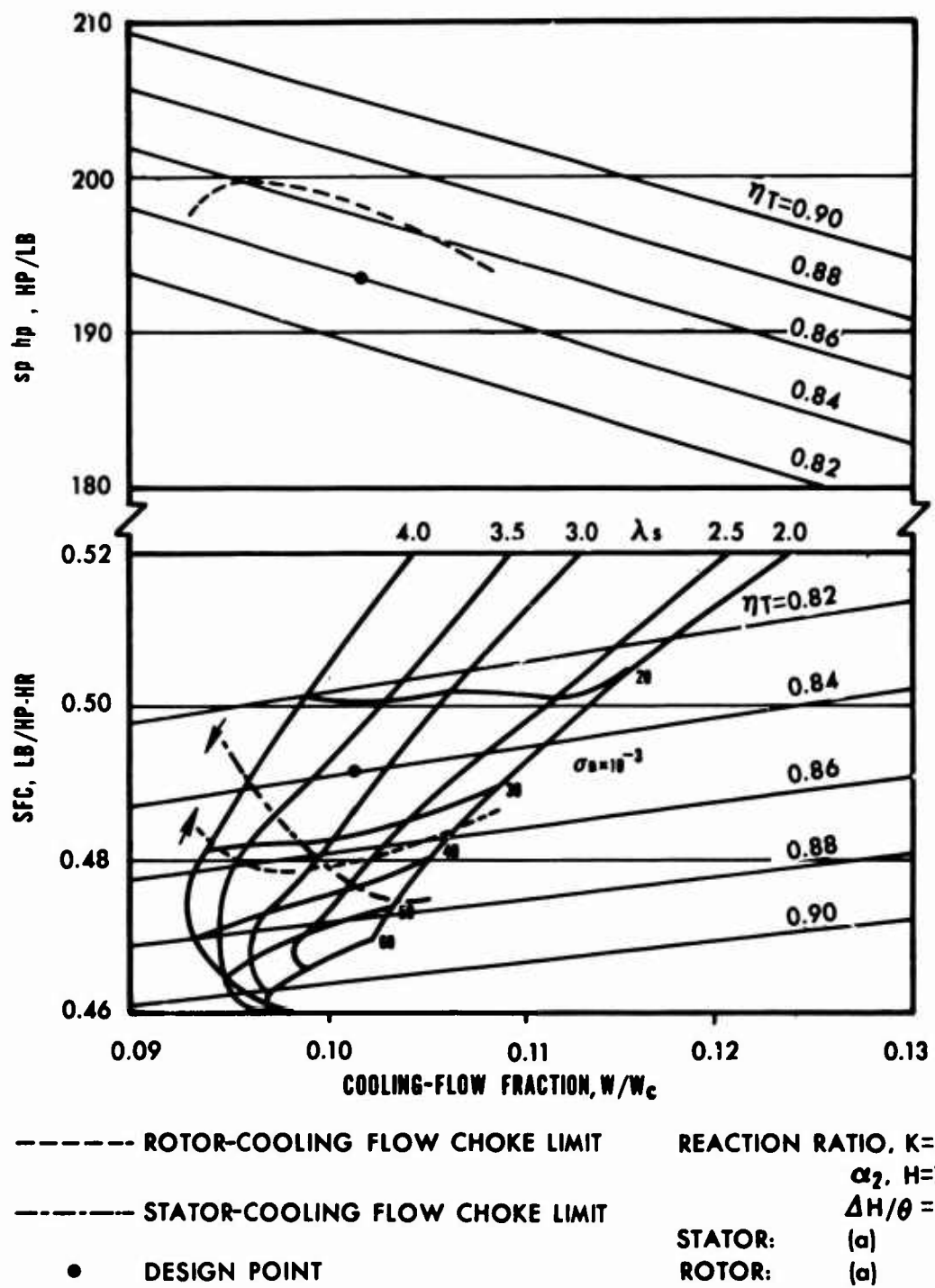


Figure 6. Phase I Results of Optimization Study.

3. As the blade stress level was increased for a given stage work coefficient, turbine efficiency increased and cooling flows decreased. However, a point was reached where the rotor-cooling requirement became dominant due to the low metal temperatures required. This point was dependent upon the stage work coefficient, but was generally in the range from 40,000 to 60,000 psi blade stress. Beyond this stress level, cooling flows increased, although turbine efficiency continued to improve. However, diminishing returns in SFC and sp hp were realized.

From these considerations alone, the desirability of operating the turbine at as high a stress level as feasible was apparent. This limiting stress level was determined by the flow capacity of the cooling flow passages in the rotor. Thus, as turbine size was reduced by increasing blade stress, rotor blade cooling requirements increased. A point was reached where the discharge area of the cooling passage choked. In this study, it was assumed that sufficient total pressure was available to choke the cooling-passage discharge area at the downstream static pressure level. This point represented a limit in blade stress that cannot be exceeded without major improvements in cooling-passage design and manufacturing capabilities.

The locus of the rotor-blade cooling-flow choke points is indicated in Figure 6. This figure indicates that an optimum value of blade stress and hub work coefficient exists both for SFC and sp hp. Peak sp hp required designs having slightly higher stage work coefficients and reduced stress levels in comparison to minimum SFC. However, the differences were not great, and design levels of σ_B and λ_s can be selected to provide the best compromise.

For this particular phase of the study, an optimum design condition appeared to be

$$\sigma_B = 35,000, \quad \lambda_s = 3.0$$

However, the turbine vector diagram for the 1.2 reaction ratio required a rotor inlet critical Mach number of 0.82 at the hub radius. At the same time, consideration of the rotor leading-edge cooling problem required a leading-edge diameter of 0.082 inch, which is considerably larger than desired if shock effects are to be minimized at this high inlet Mach number. This

leading-edge diameter, along with the blade pitch required for optimum passage solidity, resulted in large leading-edge blockage ratios.

2.1.4.2 Phase II

To reduce the complexities encountered in Phase I, the second phase of the study considered the effects of an increase in rotor hub reaction ratio to $K = 1.4$, with all other input quantities remaining fixed. The results of repeating the analysis for $K = 1.4$ are presented in Figure 7.

The general trends outlined in Phase I for $K = 1.2$ were preserved for this study. It is notable that the higher reaction blading had a somewhat increased cooling-flow requirement. However, turbine efficiency levels also increased, so that the net result, in terms of SFC and $sp\ hp$ at the optimum point, was a slight increase in SFC and a slight decrease in $sp\ hp$ for the higher reaction case.

The optimum design point for $K = 1.4$ was also determined by the flow capacity of the rotor cooling-flow passages. In this case, the design condition becomes

$$\sigma_B = 30,000, \quad \lambda_s = 2.5$$

It may be noted that no solution actually exists that satisfies both stator and rotor. However, since the choke flow characteristic for the stator is an insensitive function, it is felt that its significance is of second order. Therefore, emphasis is placed upon the rotor characteristic for determination of the optimum design point.

The turbine for this design condition had a rotor inlet critical Mach number of 0.70 at the hub. The leading-edge diameter required for cooling this case was 0.076 inch. The combination of this leading-edge diameter with an increased blade pitch at optimum passage solidity resulted in a lower leading-edge blockage ratio at a reduced inlet critical Mach number compared to the low reaction design.

2.1.4.3 Phase III

The following subparagraphs are concerned with examining the effects of changing some of the parameters held constant during the investigations previously described.

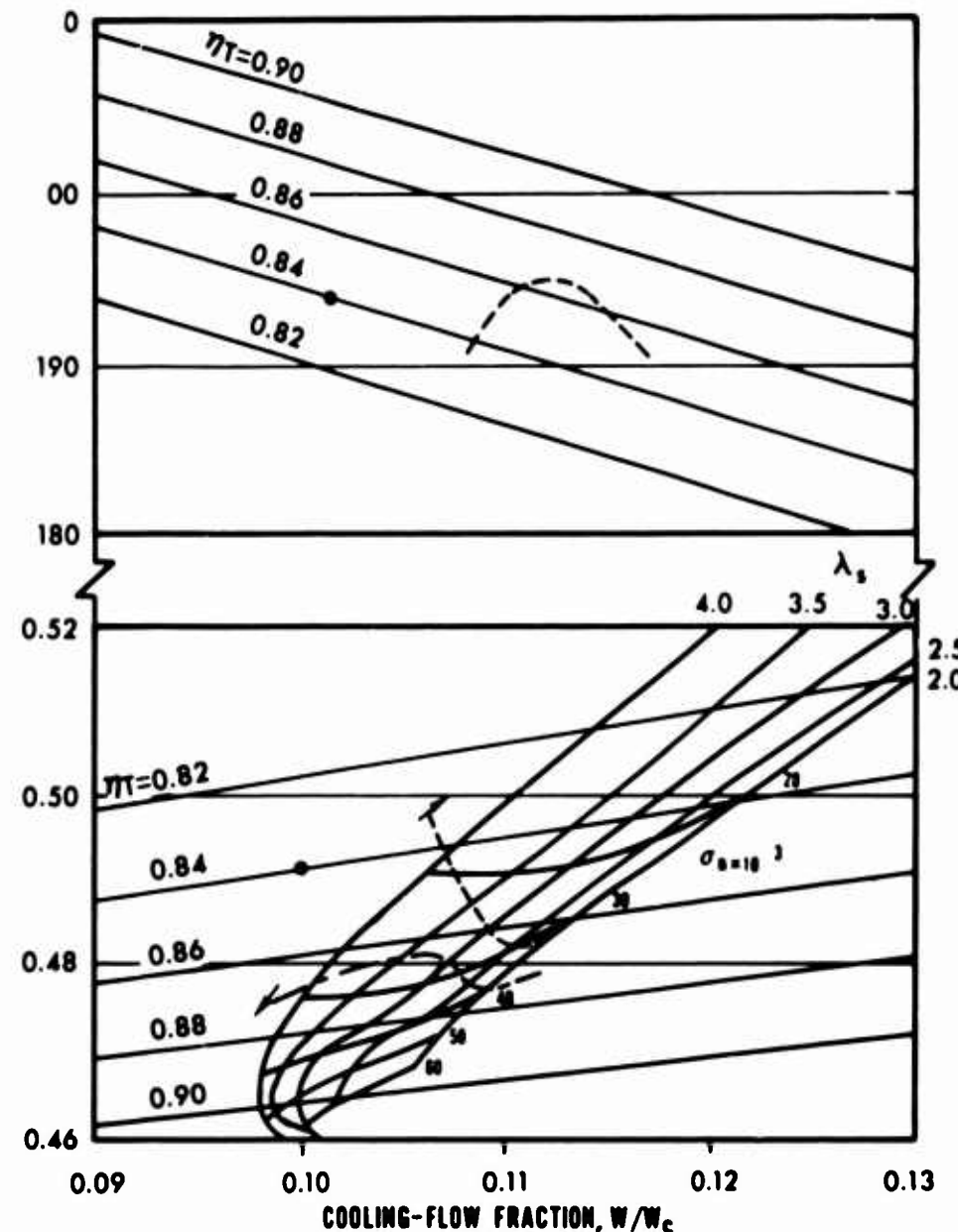


Figure 7. Phase II Results of Optimization Study.

No Stator Cooling

Consideration was first given to changes in the optimum design conditions that resulted from considering only penalties due to rotor cooling. In the program, this was achieved by raising the allowable stator metal temperature above the turbine inlet temperature. Physically, this required that a stator material be found that did not require cooling.

The complete analysis was repeated with the preceding assumptions for both $K = 1.2$ and $K = 1.4$. Since the stator no longer required cooling, the turbine design point shifted to a lower $\Delta H/\theta$, which was a reflection of the increased turbine through-flow and reduced turbine pressure ratio required to drive the compressor.

The general trends with respect to changes in λ_s and σ_B previously determined were preserved. It is important to note than an improvement in SFC of about 5 percent and an increase in sp hp of about 10 percent at the optimum design point resulted from the elimination of stator cooling-flow penalties. However, it was believed that the stator cooling-flow penalties employed in the earlier study were more realistic in terms of current materials technology. Therefore, optimization of the turbine design was confined to configurations having cooled stators and cooled rotors.

Effect of Stator Hub Exit-Flow Angle

The effects of changes in stator hub exit-flow angle, $\alpha_{2,H}$ on SFC and sp hp at the turbine design points corresponding to the following were considered (optimum values from Phases I and II) :

$$K = 1.2, \lambda_s = 3.0, \sigma_B = 35,000$$

$$K = 1.4, \lambda_s = 2.5, \sigma_B = 30,000$$

For these two design conditions based on $\alpha_{2,H} = 70^\circ$, $\alpha_{2,H}$ was varied from 60° to 80° , while all other variables remain fixed. Results of this analysis are shown in Figure 8. This figure shows that $\alpha_{2,H} = 70^\circ$ was optimum when considering both SFC and sp hp.

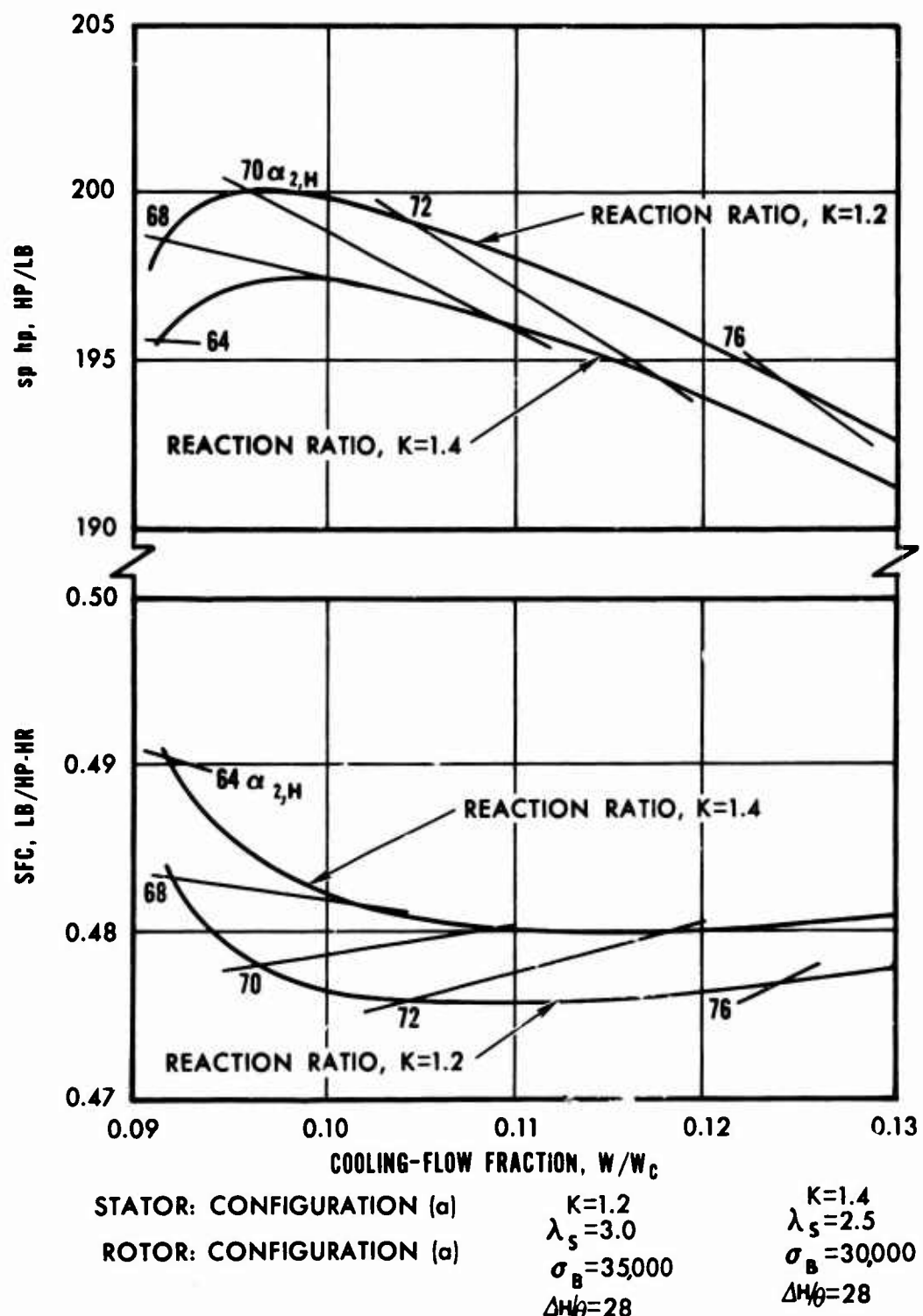


Figure 8. Phase III Results of Optimization Study.

Effect of Stator- and Rotor-Cooling Schemes (Ref. Figures 2 and 3)

Figure 9 shows the effects of stator- and rotor-cooling configurations (b), (c), and (d) on SFC and sp hp at the optimum design point for the originally selected cooling configuration, (a). From this investigation, it appeared that the original cooling configuration (a) provides the best results in terms of SFC and sp hp, although some of the other configurations required lower overall cooling flows.

The stator-cooling configuration (a) provided the highest performance because of the higher percentage of directed stator-cooling flow. This result stemmed from the trailing-edge cooling-air discharge arrangement in contrast to the single-, double-, and triple-pass radial-discharge stator-cooling configurations.

The selected rotor-cooling configuration (a) provided the best overall rotor-cooling performance mainly because the load-carrying member (strut) was somewhat insulated from the full effect of mainstream gas temperature by the conduction temperature drop through the sheet metal skin.

Varying Blade Taper

Figure 9 also indicates the effect of an increased blade cross-sectional area taper assumption on overall performance at the optimum design point for $K = 1.4$. The increased blade taper resulted in a 2-percent reduction in SFC, due to reduction in cooling requirement from 0.11 to 0.10, along with an efficiency increase of 1-1/2 points. However, it should be noted that the increased blade taper would be extremely difficult to achieve in practice, since it would result in severe compromises in aerodynamic and cooling-passage geometry. It is believed that the original blade taper curve (normal taper) represents a realistic approximation to the design of a cooled turbine blade.

2.1.5 Design Selection

Preliminary investigation of the two candidate designs ($K = 1.2$ and $K = 1.4$) indicated that the high-reaction design was the most favorable. The reasons for selection of the high-reaction design rather than the low-reaction design are listed below:

1. The high-reaction design had a lower inlet relative Mach number. This condition is desirable for cooled turbines requiring blunt leading edges.

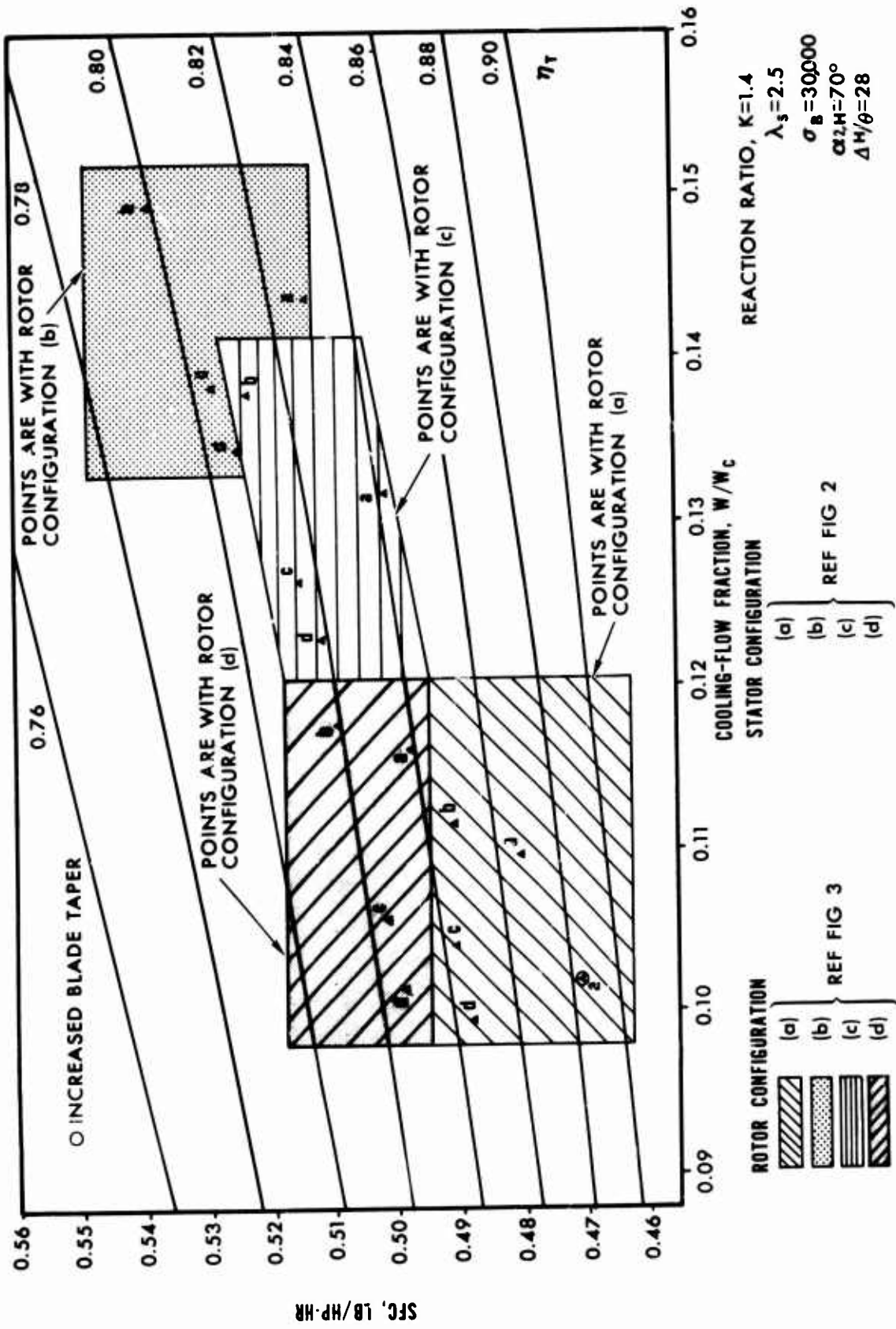


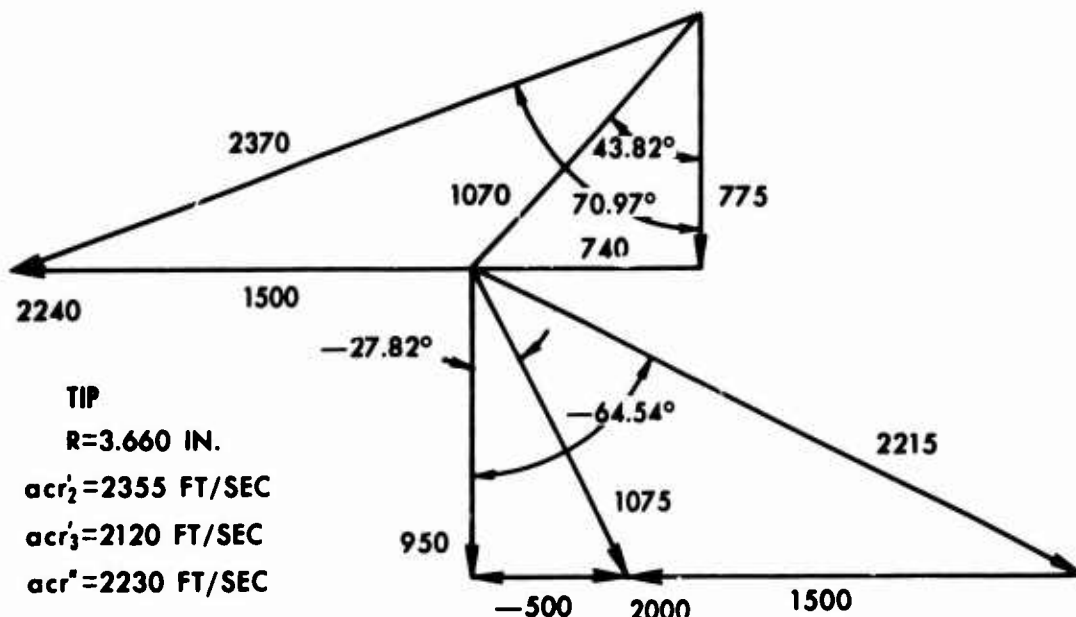
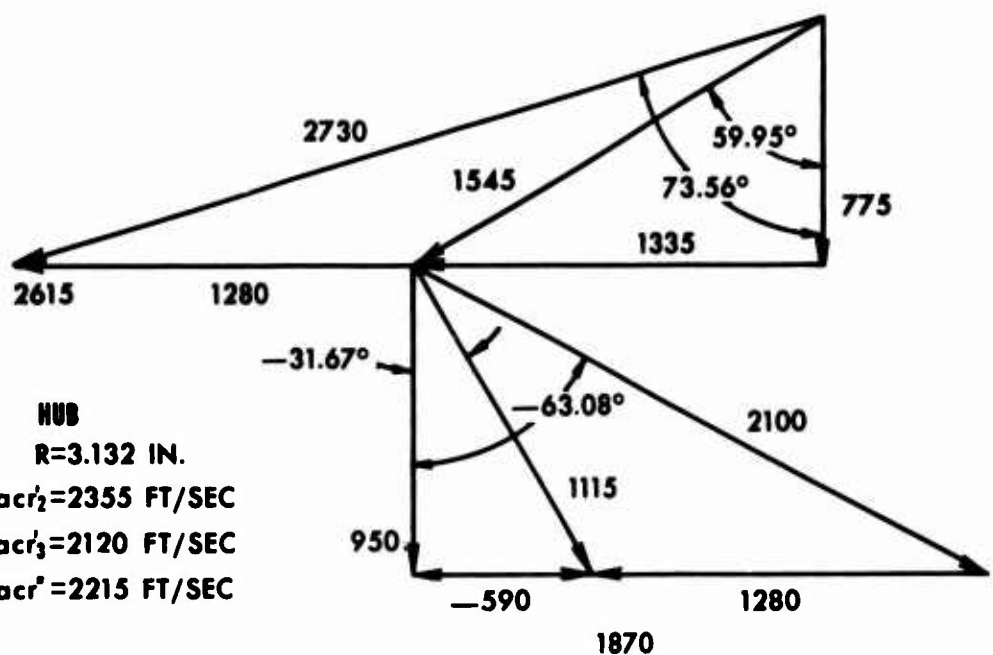
Figure 9. Effects of Stator- and Rotor-Cooling and Increased Blade Taper.

2. The high-reaction design required a smaller physical leading-edge diameter, by virtue of the reduced inlet velocity, to maintain an average leading-edge stagnation point heat-transfer coefficient of 1000 Btu/hr-sq ft-°F.
3. The high-reaction design had a lower optimum solidity requirement which, for the axial chord of 1 inch, results in a larger blade pitch.
4. Larger blade pitch requirements resulted in reduced leading- and trailing-edge blockage ratios. The increased blade pitch also provides greater flexibility in the blade attachment design.
5. Higher rotor hub reaction reduced the possibility of shock-induced boundary-layer separation in the leading-edge region, which may result in complete flow separation in the rotor. Higher reaction provides the favorable pressure gradient necessary to allow the boundary layer to remain attached to the blade surface within the guided channel.
6. Mach number and swirl angle in the downstream duct were lower for the high-reaction design. It should be noted, however, that this trend was caused primarily by the reduction in stage work coefficient, λ_s , from 3.0 to 2.5. For fixed values of λ_s , the Mach number and swirl angle in the downstream duct increase as the reaction increases.

2.2 AERODYNAMIC DESIGN

Although the stator design was not of direct value in generating blade attachment concepts and designs, certain details of the stator are presented for reference purposes. The aerodynamic design of the blade was completed in sufficient detail to provide realistic input for attachment studies.

For the reasons noted in Section 2.1.5, a detailed aerodynamic design is presented for the high-reaction-ratio ($K = 1.4$) turbine. Detailed turbine vector diagrams with the assumption of free vortex flow and simple radial equilibrium are given in Figure 10 for the rotor exit hub and tip radii. The meridional flow path is presented in Figure 11. Table VI lists the important aerodynamic parameters for the turbine as a function of radius.



NOTE: ALL VELOCITIES IN FT/SEC

Figure 10. Turbine Vector Diagrams.

The results of the optimization study indicated that a rotor hub axial chord of 1 inch is the smallest size allowable. Reduction of this dimension results in reduced cooling-flow capacity in the rotor for a fixed trailing-edge blockage ratio. Rotor trailing-edge thickness was set at 0.040 inch for a 1-inch rotor hub chord. The effect of the resulting trailing-edge blockage ratio on turbine efficiency is given in the following section. The stator tip axial chord was also set at 1 inch, with 0.040-inch trailing-edge thickness.

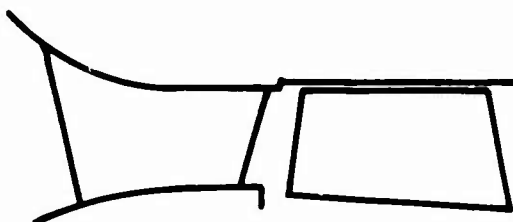


Figure 11. Turbine Meridional Flow Path.

2.2.1 Stage Efficiency Analysis

An analysis of the stage aerodynamic efficiency was carried out by use of analysis techniques developed at AiResearch that were based on the work of Stewart, Whitney, and Wong¹ and Stewart, Glassman, and Vanco.²

Results of the aerodynamic efficiency analysis are presented in Figures 12, 13, and 14. Figure 12 gives the local total momentum thickness parameters per unit surface length at the blade trailing edge versus section radius for both the stator and the rotor. Also plotted is the local stage efficiency for both zero and design values of stator and rotor trailing-edge thickness. The effect of trailing-edge thickness was to reduce the local efficiency about 1.5 points at the hub and 1.0 point at the tip. The efficiency values do not include the effects of tip clearance.

TABLE VI. VECTOR DIAGRAM CONDITIONS

Parameters	Hub	Mean	Tip
Section radius - in.	3.1316	3.3958	3.6600
Stator inlet flow angle - deg	0.0	0.0	0.0
Stator inlet - Mach no.	0.162	0.162	0.162
Stator exit flow angle - deg	73.56	72.25	70.97
Stator exit - Mach no.	1.158	1.076	1.006
Stator reaction (V_3/V_1)	7.148	6.641	6.209
Rotor inlet flow angle - deg	59.95	52.96	43.82
Rotor inlet - relative Mach no.	0.697	0.577	0.480
Rotor exit flow angle - deg	-63.00	-63.75	-64.54
Rotor exit - relative Mach no.	0.947	0.969	0.993
Rotor reaction (W_3/W_2)	1.359	1.679	2.069
Rotor hub Mach no.	0.544	0.590	0.636
Stator inlet total pressure - psia	139.6	139.6	139.6
Stator inlet static pressure - psia	137.5	137.5	137.5
Stator exit total pressure - psia	133.3	133.3	133.3
Stator exit static pressure - psia	57.94	65.57	72.18
Rotor inlet rel. total pressure - psia	77.12	79.71	82.59
Rotor exit rel. total pressure - psia	70.28	72.64	75.26
Rotor exit static pressure - psia	40.99	41.24	41.44
Stator inlet total temperature - °R	2860.0	2860.0	2860.0
Stator inlet static temperature - °R	2848.0	2848.0	2848.0
Stator exit static temperature - °R	2313.2	2387.2	2445.9
Rotor inlet rel. total temp. - °R	2527.6	2546.6	2567.1
Rotor exit abs. total temp. - °R	2321.0	2321.0	2321.0
Rotor exit static temperature - °R	2023.7	2009.8	1995.1

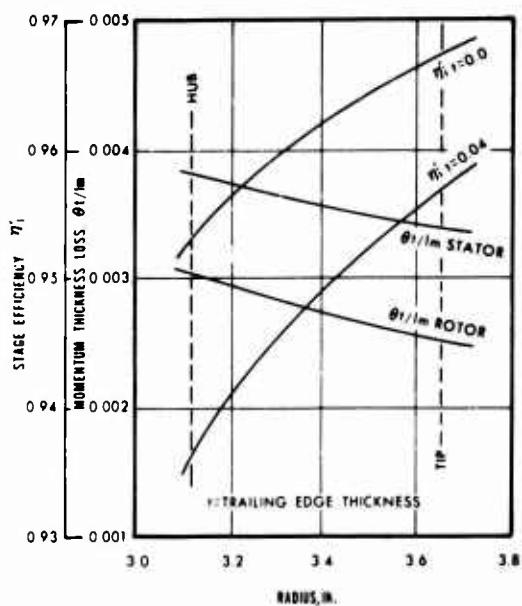


Figure 12. Local Loss Characteristics.

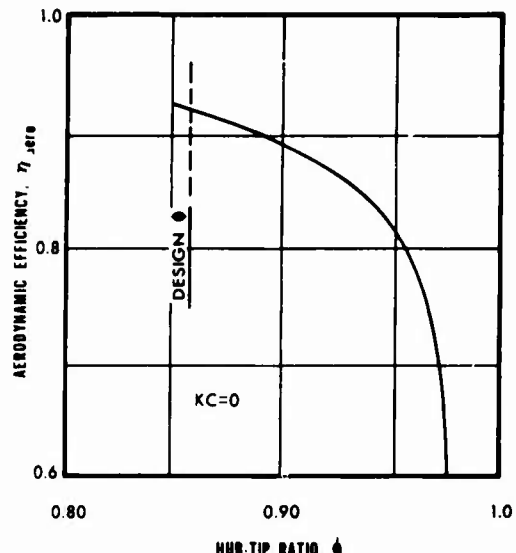


Figure 13. Stage Efficiency Versus Hub-Tip Ratio.

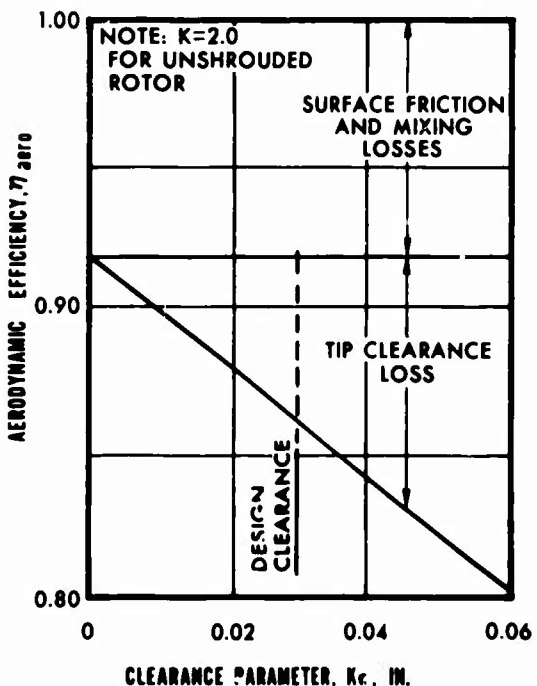


Figure 14. Overall Stage Efficiency.

Figure 13 presents aerodynamic stage efficiency at zero clearance versus stage hub-tip ratio. This curve indicates the relative magnitude of the aspect ratio correction due to end-wall boundary-layer losses.

Figure 14 gives the overall aerodynamic stage efficiency as a function of the tip clearance parameter K_c . It is notable that, at the design radial clearance of 0.015 inch, the loss in efficiency due to clearance is almost equal to the total of surface friction and mixing losses for the entire stage. The slope of the efficiency

curve indicates that stage efficiency is extremely sensitive to changes in tip clearance; therefore, close control of clearance is mandatory for good efficiency.

Since the turbine stage required cooling, the predicted aerodynamic efficiency was modified to include the effects of cooling. The methods by which this correction was made are described in Section 2.1.3.

For the final turbine design, the optimization analysis predicted the following percentage of cooling-flow distributions for the stage:

$$\text{Stator cooling, } (w/w_c)_S = 7.54 \text{ percent}$$

$$\text{Rotor cooling, } (w/w_c)_R = 3.44 \text{ percent}$$

$$\text{Total stage cooling, } w_t/w = 10.98 \text{ percent}$$

$$\text{Directed fraction of stator cooling, } X = 44.60 \text{ percent}$$

With use of the design values of hub speed, stage work, and cooling-flow fractions, the turbine power ratio became

$$\frac{HP_{cooled}}{HP_{uncooled}} = 1.019 \quad (10)$$

The fact that this ratio was greater than unity indicated that the increase in turbine work produced by the directed fraction of stator-cooling air was greater than the deficit in work due to the combined effects of undirected stator-cooling air and pumping work done on the rotor-cooling air. The effective stage efficiency with cooling became

$$\eta'_{aero} = 0.858 \text{ at } Kc = 0.03$$

$$\eta'_{cool} = 0.874 \text{ at } Kc = 0.03$$

It should be noted that the efficiency levels may be somewhat optimistic, since the following factors were not included in the analysis:

1. Stator and rotor shock losses
2. Secondary flow losses

3. Nonadiabatic flow effects such as the reduction in rotor total temperature due to stator cooling.

2.2.2 Detailed Blading Design and Analysis

The blade and vane design procedure began with the design of two-dimensional cylindrical sections satisfying the vector diagram. The sections were designed at equal radial increments from hub to tip to facilitate stacking and fairing of the profiles.

The procedure used to design the cylindrical sections followed the steps described below to generate a profile satisfying a given vector triangle.

1. A relative critical Mach number and flow angle in the plane of the trailing edge were calculated from the specified vector triangle downstream of the blade for the required blade spacing and trailing-edge thickness. The calculation assumed one-dimensional flow and satisfied continuity and momentum equations for either subsonic or supersonic flow in the plane of the trailing edge.
2. The blade suction surface was generated by an involute curve that turned from the inlet flow angle specified by the upstream vector triangle to the calculated blade angle. The blade-section stagger angle was a function of the inlet-to-exit curvature ratio of the involute curve, which was an input number. The solidity of the passage was determined from Zweifel's³ criterion on the basis of an input aerodynamic loading coefficient.
3. The profile pressure surface was specified as input data.
4. The passage velocity distribution was calculated by estimating blade-to-blade velocity gradients and adjusting suction surface velocities until continuity was satisfied. The resulting velocity distribution generated a circulation that was in close agreement with the required value imposed by the vector diagram.

5. A two-dimensional boundary-layer analysis based on the methods described by Whitney, Stewart, and Miser⁴ was calculated by use of the velocity distribution, along with the generated blade profile.

The procedure that was used for this activity had several drawbacks. The program did not determine the leading-edge contour; therefore, the velocity distribution on this portion of the blade could not be calculated. The effects of three-dimensional flow within the blade row were accounted for in an approximate manner in that the specific mass flow was assumed to vary linearly with axial chord from the inlet to the exit of the blade row to satisfy the vector diagram at a given section radius. In addition, the procedure did not account for the effect of blade wakes downstream of the throat.

Figures 15 and 16 describe the results of the two-dimensional cylindrical blade section design and analysis. Each figure presents a drawing of hub and tip blade profiles in their correct orientation, along with the calculated velocity distribution. A brief discussion of the design philosophy of each blade row follows.

2.2.2.1 Stator

The stator was designed with 25 vanes and a trailing-edge thickness of 0.040 inch to accommodate the internal cooling configuration. The resulting blockage ratio of the hub profile was 0.16, which is extremely large when compared with uncooled designs. The losses incurred from such high blockage ratios are difficult to determine with certainty due to interactions of the wake and mainstream flow.

The calculated vane channel velocity distributions are given in Figure 15. As a result of the high reaction, little suction or pressure surface diffusion is apparent.

The leading-edge radius of 0.100 inch was selected to minimize stagnation-point heat-transfer coefficients and to allow sufficient room for good internal cooling.

The complete vane profile was defined by stacking the designed cylindrical sections on a radial line passing through the center of the throat of each section. Vane pressure surfaces were adjusted to ensure a smooth fairing from hub to tip.

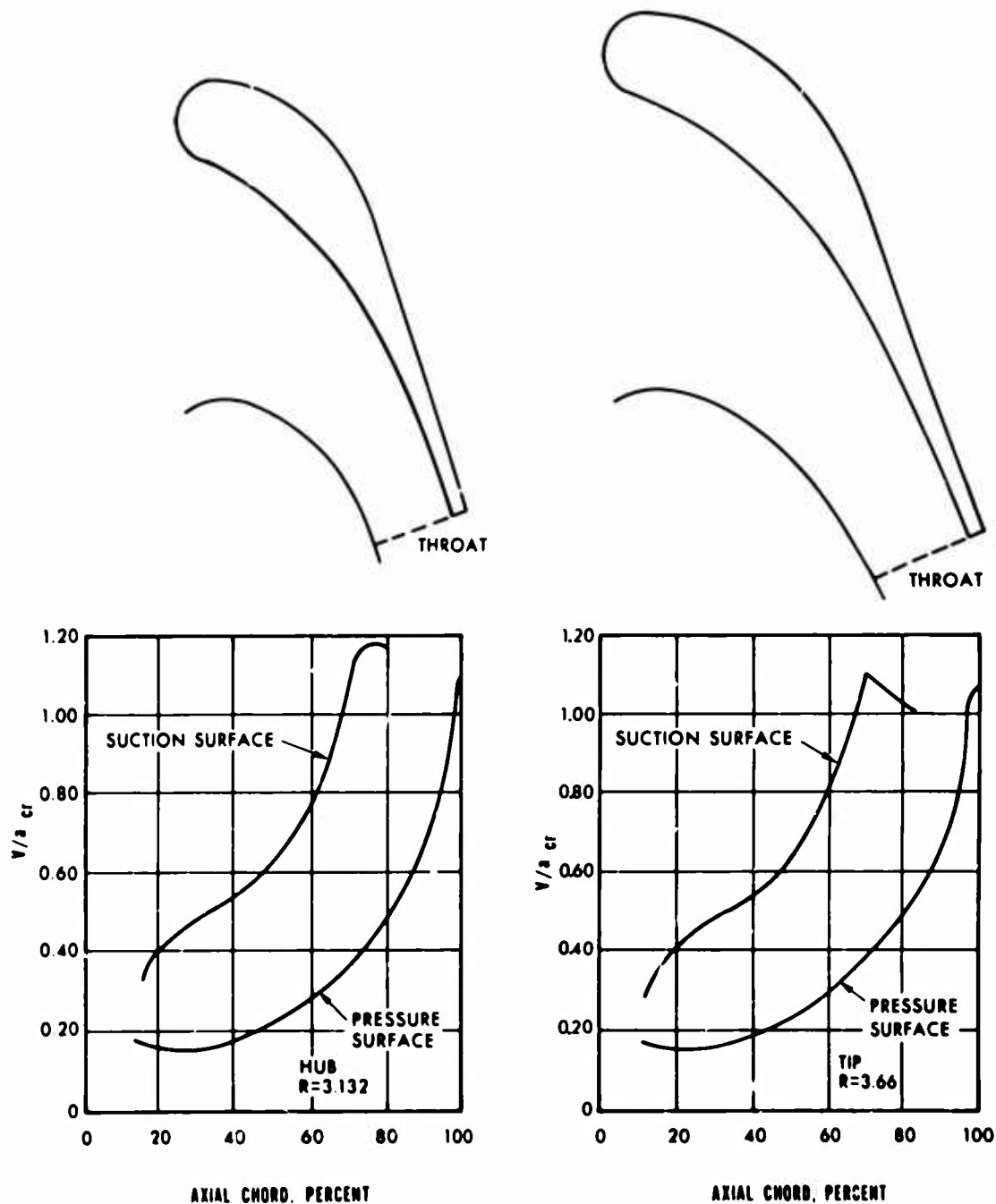


Figure 15. Vane Channel Velocity Distribution.

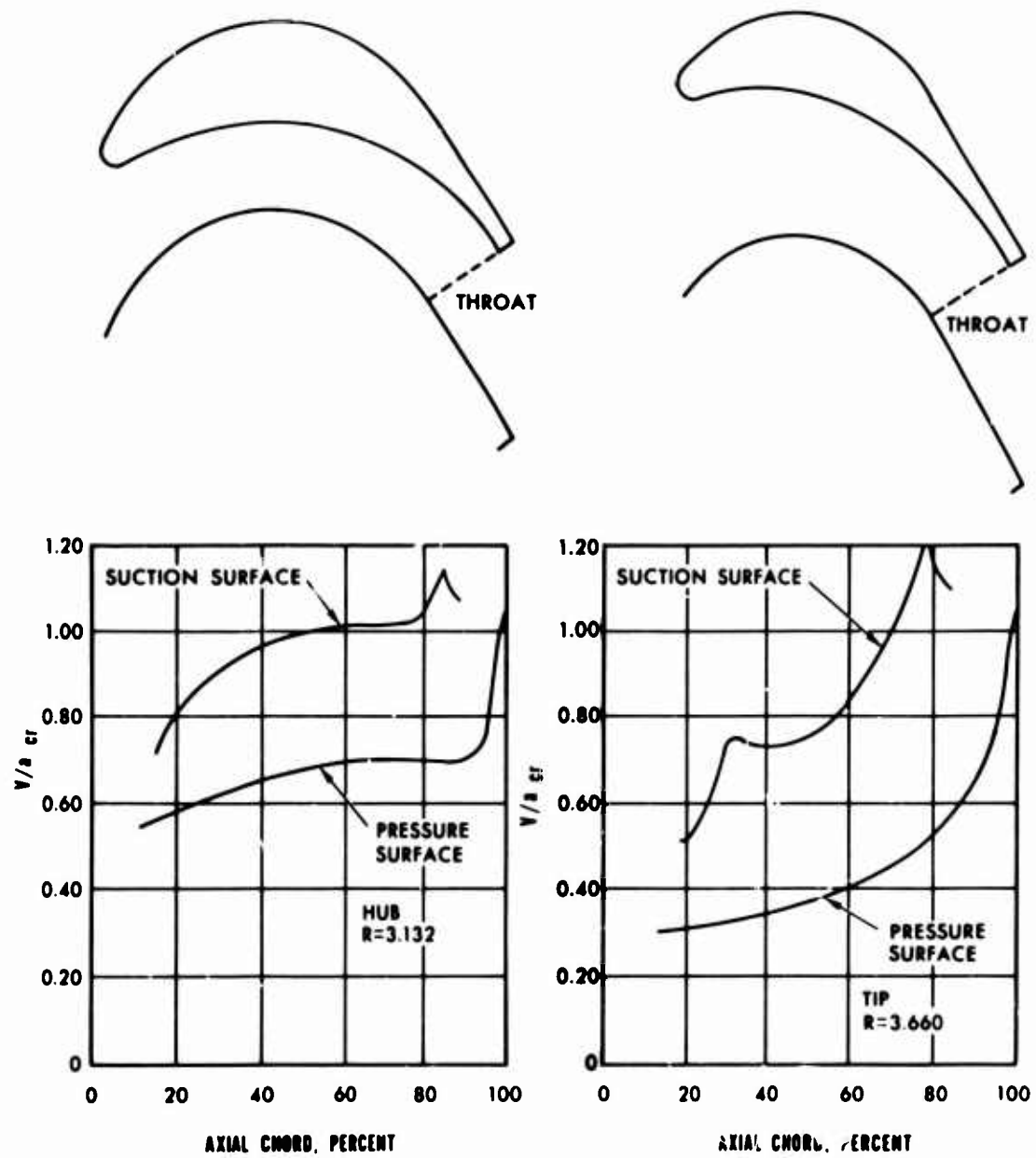


Figure 16. Blade Channel Velocity Distribution.

2.2.2.2 Rotor

The rotor was designed to have 44 blades and a trailing-edge thickness of 0.040 inch to accommodate the necessary internal cooling passages. The resulting blockage ratio at the hub section was also 0.16. The calculated blade channel velocity distributions are presented in Figure 16. The hub section provides a good approximation to the ideal rectangular blade loading, having minimal suction-surface diffusion and a pressure surface diffusion of 0.24. The tip section has a slightly increased suction surface diffusion and a pressure surface diffusion of 0.35. Allowable diffusion values of 0.55 or less were recommended. The surface diffusion is then defined as

$$\text{Suction surface diffusion, } D_s = 1 - \frac{V_{\text{exit}}}{V_{\text{max}}} \quad (11)$$

$$\text{Pressure surface diffusion, } D_p = 1 - \frac{V_{\text{min}}}{V_{\text{inlet}}} \quad (12)$$

To minimize bending stresses in the rotor, the cylindrical sections were stacked about a radial line passing through the center of gravity of each section. The blade stacking is complicated by the presence of the cooling passage--that is, the design of the cooling passage is dependent on the blade stacking, since this geometry controls the stresses within the blade. However, the blade stacking without inclusion of cooling passages was considered sufficiently accurate for use in stress calculations required to define the blade attachment concepts.

1. MECHANICAL DESIGN AND ANALYSIS

With the turbine annulus and blade shape defined by the aero-thermodynamic design activity, the details of determining feasible blade/disk attachment concepts were considered.

While the optimization study indicated that a strut-supported sheet metal blade--Configuration (a) of Figure 1--resulted in the best RBC and sp/tip combination, it should be immediately clarified that the blade/disk attachment concepts evaluated, selected, and tested in this program were not restricted to the use of such a blade design. Of the four blade configurations that were considered in the optimization study, three could be configured by cast/coring techniques. Though certain variations in blade weight and, consequently, rotor size may exist, the geometry of all four blade configurations is approximately common with respect to the blade pedestal and cooling-air inlet passages. Therefore, a blade/disk attachment method determined to be suitable for any one configuration would be sufficient for any of the four.

However, since the optimization study did suggest use of the strut-supported sheet metal blade, and since this design is unconventional for rotating blades, a preliminary evaluation of the joining problems associated with the shell/strut joint was conducted. This evaluation was conducted in parallel with the preliminary tests for blade/disk attachments and generally differed only by material combinations. One exception was that an evaluation of cast bonding was conducted for the shell/strut application only.

3.1 MECHANICAL-DESIGN OBJECTIVES

Objectives of the mechanical-design activity were:

1. To further evaluate, modify if necessary, and finalize the rotor blade cooling geometry
2. To determine the complete turbine-rotor assembly metal-temperature profile
3. To determine the turbine rotor blade load and stress-rupture life
4. To select several feasible blade/disk attachment concepts for preliminary test evaluation
5. To establish the final turbine rotor designs for the three most promising blade/disk attachment concepts

In addition, a parallel activity (described in Section 4. FABRICATION TECHNOLOGY DEVELOPMENT) was undertaken to support and supplement the mechanical design and analysis. The goals of the parallel activity were:

1. To select several suitable material types for fabrication of the disk, cast/cored blade or strut, and sheet metal blade shell
2. To evaluate and determine by fabrication and joint-property preliminary-type testing the most advantageous material types and blade/disk attachment concepts (also to evaluate shell/strut attachment concepts)
3. To obtain potential joint-strength data that would aid in the design of the final test specimens and in the final turbine rotor designs

While compromising of several factors was involved in establishing the mechanical design, emphasis was placed upon evolving a design such that the rotor could be produced in production quantities at a reasonable cost.

Prior to initiating the mechanical design activity, an extensive literature survey was conducted and a survey of Government agencies was made to review existing blade attachment methods and joining processes that might be applicable to the subject design. Recent activities involving turbine blade attachments were found to be confined mostly to space applications and were not compatible with the subject-design requirements. However, considerable material describing various joining processes was found, some of which appeared to be feasible for use in blade attachment design concepts. A listing of pertinent material deduced during the literature survey is presented in the appendix.

3.2 FINAL DESIGN OF BLADE

For the design conditions under consideration, the optimization study of the aerothermodynamic design activity suggested that the optimum values of SFC and sp hp would be realized by utilization of vane cooling scheme Configuration (a), (Figure 2), and blade cooling scheme Configuration (a), (Figure 3). Details of the vane design will not be included in this report, since they have no direct bearing on the blade/disk attachment study.

As shown in Figure 3, the blade cooling scheme of Configuration (a) is a strut-supported sheet metal shell with radial flow in the leading-edge and centerbody regions, chordwise

flow in the tip region, and trailing-edge discharge. Coolant flows radially outward through passages formed by the strut and sheet metal, turns and flows chordwise in the tip region, flows radially inward in the trailing-edge region, and discharges uniformly through the trailing edge into the main gas stream.

Layout studies of various blade attachment concepts, combined with the radial-flow blade, indicated a serious problem in the definition of a coolant supply plenum in the pedestal region of the design. The prime reason for considering radial flow in the strut, as opposed to chordwise flow, is to eliminate parasitic loads inherent in the chordwise-flow configuration resulting from the non-load-carrying members, and hence, to reduce the blade root loading. To realize full load-carrying ability from the radial-flow "lands," these members must extend into the pedestal region and as a result would complicate the plenum configuration and root region of the sheet metal shell. In view of these complications as they relate to fabrication, it was decided to utilize a chordwise-flow blade configuration and accept the non-load-carrying penalty.

3.2.1 Final Cooling Configuration

The chordwise-flow concept is shown in Figure 17. Coolant flows from the central cavity of the strut through three slots in the nose and impinges against the inside surface of the leading edge. It then turns and flows chordwise along both the suction and the pressure sides in passages formed by the strut and sheet metal, and discharges uniformly through the trailing edge into the main gas stream.

The blade strut is an investment casting incorporating chordwise grooves on both suction and pressure sides for controlling coolant flow and incorporates coring to configure the internal air supply plenum. Impingement slots may be cored or may be machined by the electrical-discharge machining process. The strut is designed to eliminate a separate blade cap by extending the tip land to join the sheet metal, in both the leading-edge and the trailing-edge regions.

The outer sheet metal shell may be brazed, or with sufficient process development may be diffusion-bonded to the strut. Based upon fabrication experience, 0.010-inch-thick sheet metal was selected for the shell as offering the best compromise of the following design considerations:

1. Fabricability
2. Foreign-object damage

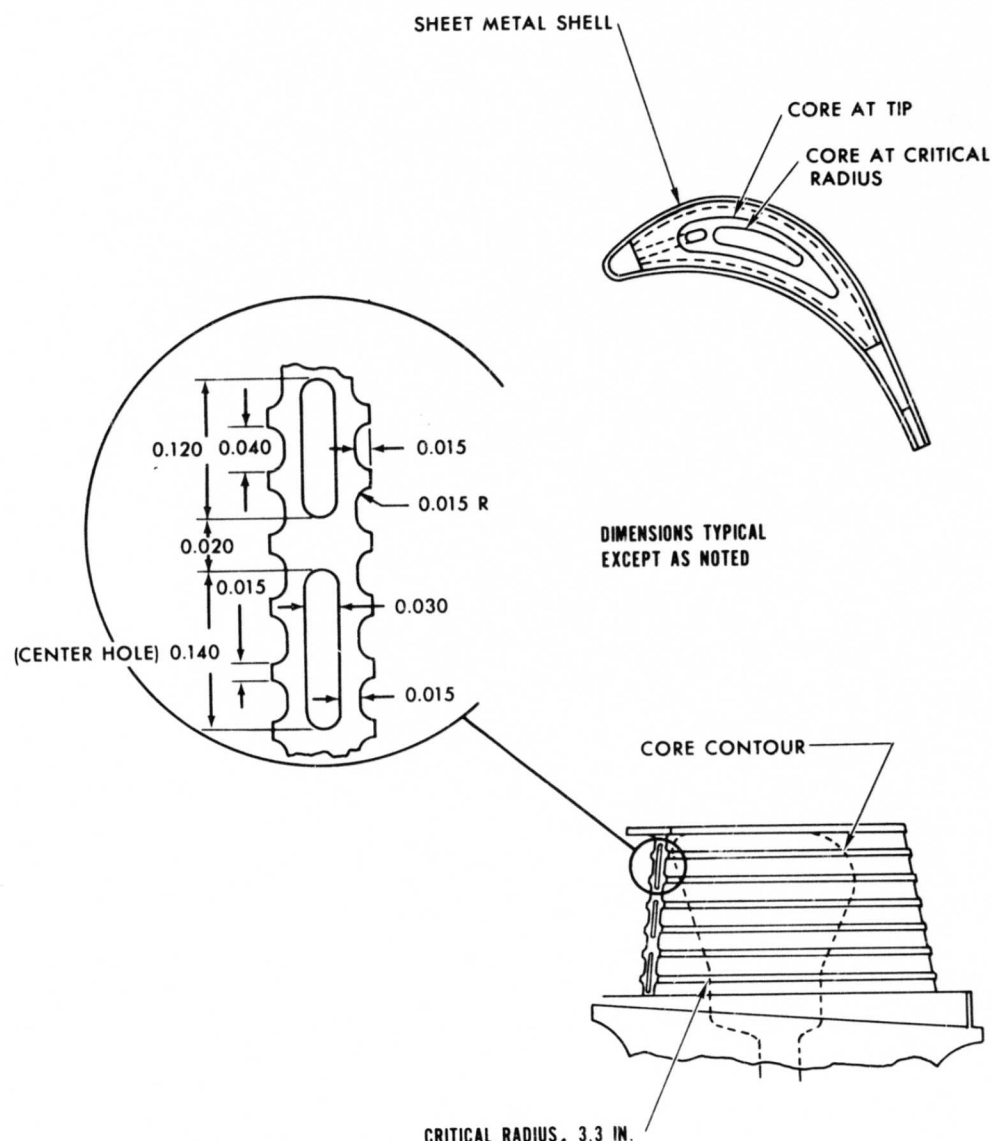


Figure 17. Chordwise-Flow Blade Configuration.

3. Considerations of erosion from brazing
4. Damage in handling
5. Minimum trailing-edge thickness

The shell is supported in shear by the strut "lands" throughout the mid-chord region. The leading-edge and trailing-edge regions of the shell are supported in shear at the root land only, with a portion of the load being transmitted back to the center section of the strut. The trailing edge contains a "wiggle strip," which serves to (a) control the coolant discharge flow area and (b) join the trailing edges structurally. The "wiggle strip," attached by brazing, is configured from 0.004-inch sheet metal and provides flow passages having the approximate shape of an equilateral triangle. The resulting trailing-edge thickness is 0.040 inch.

The chordwise-flow design, compared to the radial-flow design, has several advantages that are believed to more than compensate for the parasitic load caused by the chordwise land geometry:

1. The coolant supply route is much less complicated, and a large supply plenum in the blade attachment region is not required.
2. The sheet metal shell load may be distributed over a larger area, and no sheet metal blade cap is required.
3. The sheet metal temperature in the leading-edge region can be lowered to values similar to centerbody region values, since impingement cooling has high cooling capacity (however, for the same centerbody metal temperature, the coolant flow rate must increase slightly).
4. Blade coolant flow-distribution problems are expected to be less severe both from a physical significance viewpoint and from a computational viewpoint.

3.2.2 Blade Heat-Transfer Analysis

An analysis of the strut and sheet metal shell was performed to determine metal temperatures during steady-state operating conditions. Transient heat-transfer analysis was not considered, since it is believed that steady-state conditions sufficiently define the cooling-flow requirements for realistic blade attachment design. This reasoning also applies to

heat-transfer analysis of the disk and attachment, discussed elsewhere in this section.

Blade metal temperatures based upon the aerodynamic optimization study coolant flow rates were computed for several chordwise locations at about one-third blade height. This location (at $R = 3.3$ inches) was determined to be the critical radius for the radial-flow strut-supported sheet metal blade concept. No adjustment was made in the critical radius to account for differences in critical radius between the radial-flow and chordwise-flow designs, since the net effect is considered small. The total coolant flow rate determined by the optimization study is 10.96 percent of the compressor discharge flow, of which 2.2 percent is utilized to cool the blades. The blade metal temperatures of the chordwise-flow scheme corresponding to these flow rates are shown in Figure 18.

The sheet metal temperature in the leading-edge region and just aft of the strut is relatively high. These temperatures could be decreased by modifying the coolant flow path and/or increasing the flow rate slightly. However, it was believed that these values provided a sufficient definition of the blade to result in realistic blade attachment designs, and no modifications to the cooling geometry were made. The gas temperature profile and estimated strut temperature variation with radius are shown in Figure 19.

3.2.3 Blade Stress Analysis

With the aid of the blade strut metal temperature distributions presented in Figure 19, the stress-rupture life in the blade was determined and the required strut cross-sectional area distribution was calculated and optimized to obtain maximum life consistent with the various boundary conditions and within the general capabilities of investment casting techniques. The cored center of the blade strut was tapered to reduce the loading at the critical location ($r = 3.30$ inches) and at the same time to provide the maximum possible load-supporting cross section at this location. In addition, the cored chordwise cooling-flow slots were designed to minimize the centrifugal loading for a given cooling-airflow area.

The stress analysis of the blade was performed with use of the following major considerations:

1. Only centrifugal stresses were calculated (gas bending stresses for this blade will be negligible).

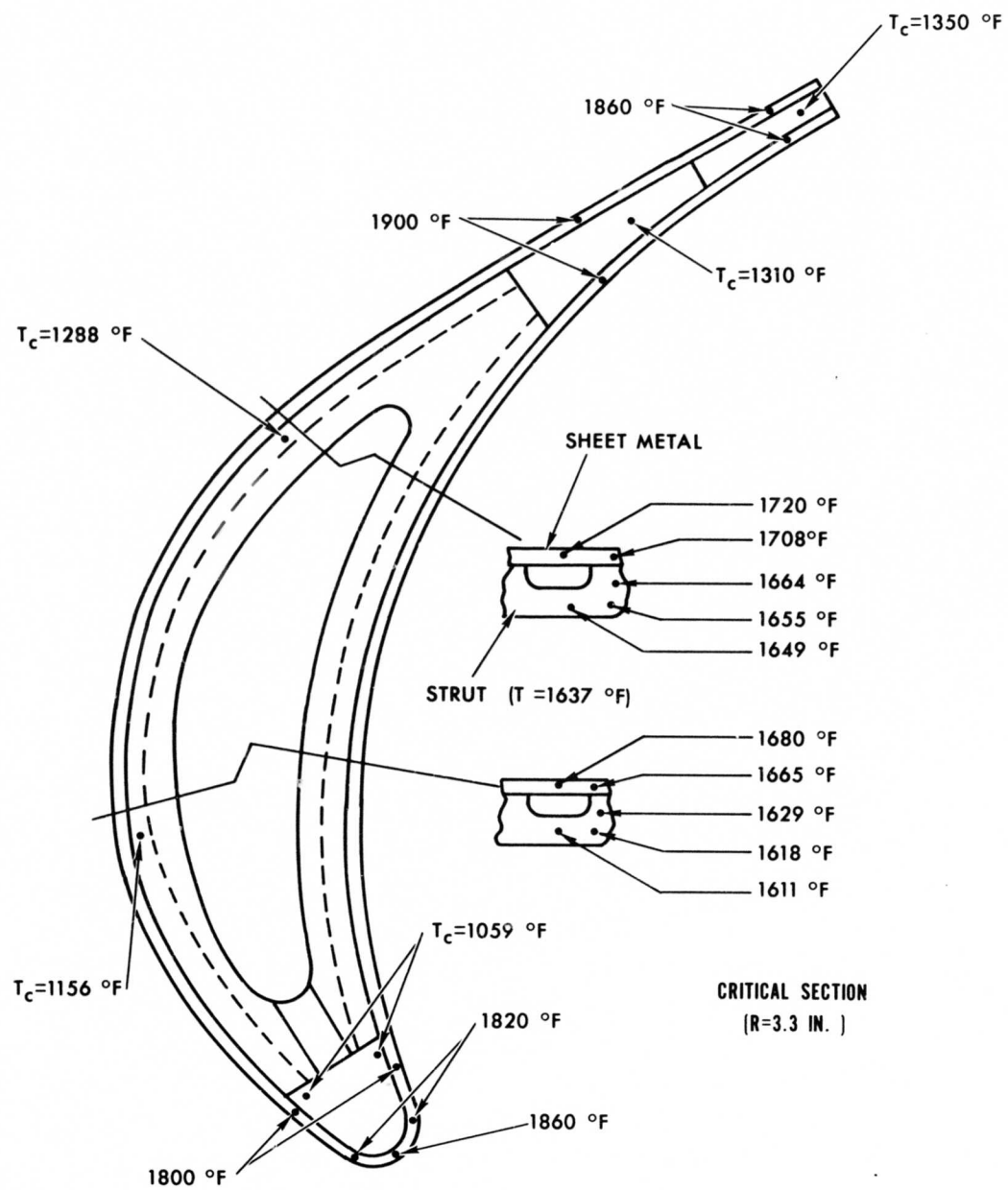


Figure 18. Blade Metal Temperatures for Chordwise Flow Configuration.

2. The centroids of the blade cross sections were assumed to lie in a radial line, thus minimizing centrifugal bending stresses in the blade.
3. The cast strut material was assumed to carry all of the load, and the shell loading was assumed to be uniformly distributed through each braze joint into the strut.
4. The cast strut material used was MAR-M 246, with a density of 0.305 lb per cubic inch.
5. The shell material used was assumed to have a nominal thickness of 0.010 inch and a density of 0.305 lb per cubic inch.
6. The mass of the braze material was neglected.

The resulting centrifugal stress distribution in the blade at design speed (46,900 rpm) is shown on Figure 20.

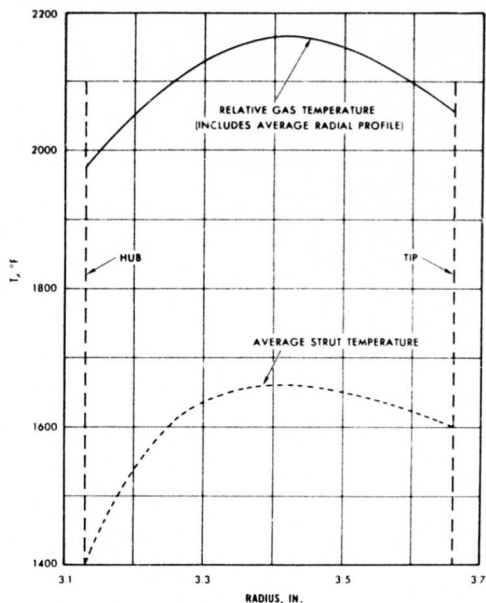


Figure 19. Gas Profile and Estimated Average Strut Temperature.

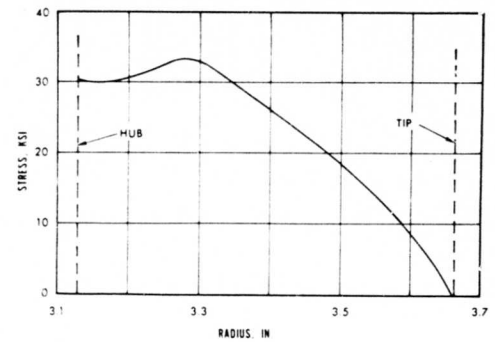


Figure 20. Centrifugal Stress Distribution of Blade.

There is insufficient MAR-M 246 rupture-strength data available to establish design minimum strength levels with any degree of confidence. However, a nominal rupture strength curve is shown on Figure 21 based on a limited amount of testing. Nominal IN-100 data corrected for density is also shown for comparison. The resulting nominal stress-rupture life for MAR-M 246 is shown on Figure 22. The minimum life of about 1800 hours occurs at a radius of approximately 3.3 inches. This exceeds the design objective of 1000 hours.

It is recognized that in any final detailed design analysis, the following additional work would be necessary to optimize the design:

1. Transient and steady-state thermal stresses in the blade at several radial stations would be calculated to determine the low-cycle fatigue life, critical location, and interaction with stress-rupture failure modes.

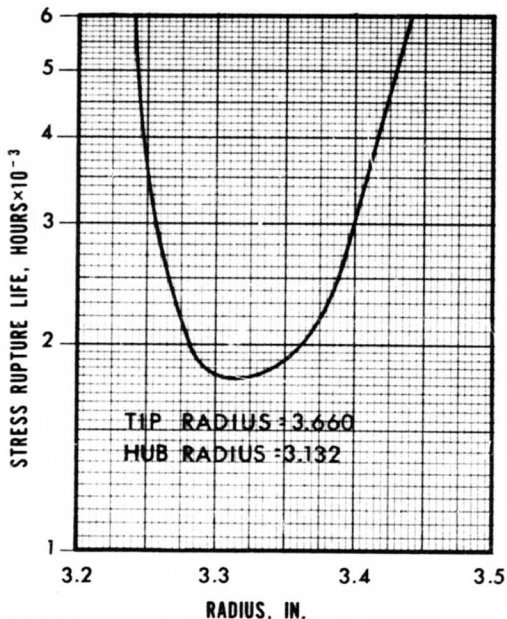
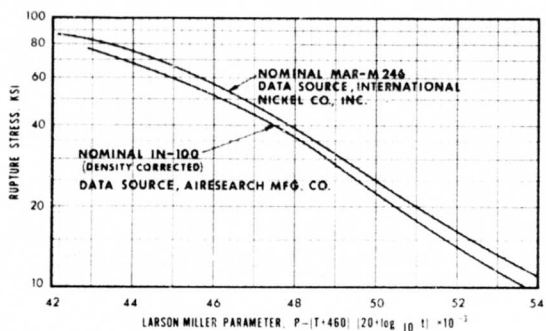


Figure 21. Comparison of MAR-M 246 and IN-100 Rupture Strength.

Figure 22. MAR-M 246 Stress-Rupture Life.

2. The blade cross sections would be stacked on a radial line to minimize centrifugal bending stress in the blade.

3.3 BLADE/DISK ATTACHMENT CONCEPTS

Knowing the blade loads and design details of the blade and blade coolant inlet flow passages provided the necessary information for design of blade attachment concepts. A number of different methods were considered in an effort to find the most feasible approach. The following basic criteria were established for the methods under consideration:

1. The joining method must attach 44 blade struts of cast nickel-base alloy such as MAR-M 246 to a disk forged of high-strength nickel-base alloy, similar to Waspaloy.
2. The joint between the blade and the disk should be capable of nondestructive testing or inspection techniques that would evaluate the soundness and reliability of the joint for its intended service.
3. The joining technique should be economically feasible for normal production quantities.
4. Strength properties of the joint should be sufficient to permit a practical design from the standpoints of weight, polar moment of inertia, and axial length.
5. Geometry of the attachment must provide for transport of coolant to the blade without excessive leakage.

The following paragraphs are devoted to a discussion of methods considered and give the design details of the selected attachment concepts. The ideas considered can be grouped into several broad classifications such as:

1. Mechanical concepts, which include axial fir trees, circumferential dovetails, and pin joints.
2. Diffusion bonding.
3. Brazing, primarily vacuum furnace brazing with nickel-base braze alloys.

4. Welding, which includes electron beam, inertia, explosive, and laser beam.

3.3.1 Mechanical Concepts

Several mechanical attachment concepts were studied, including axial fir trees, circumferential dovetails, and pin joints. Of all concepts evaluated, the conventional axial fir-tree design promised the most reliable lightweight approach for the subject turbine design.

Pin-joint designs have been used for some compressor blade attachments and offer certain advantages, such as frictional damping of flexural blade vibrations. Because of the small hub diameter of the subject turbine design and the limited space available, it is necessary to put the pin in quadruple shear. In the design considered, the estimated average shear stress is approximately 70,000 psi; thus, a very high strength pin material, such as AF2-1DA, is required. Bending stresses in the pin were not estimated, but would be a major factor in any detailed analysis. Since the pin-joint design resulted in one of the heavier of the concepts studied, it was abandoned.

A circumferential dovetail design in which a split disk was utilized was also considered. In this type of design, very large bending stresses develop in the disk due to the blade loading, and large axial through-bolts are necessary to hold the disk halves together. It is inherently a heavy design and was dropped from further consideration.

Since no other mechanical attachment concepts appeared to be particularly encouraging, the major effort was expended on the axial fir tree. A preliminary design was made and analyzed, although no attempt was made to optimize the configuration, as would be required in a final detailed design analysis. The design selected was a two-lobe configuration. Figure 23 shows the basic design configuration.

Table VII shows a summary of the stresses calculated for the preliminary design, and Figure 23 gives the respective locations of these stresses. No allowance was made for the fact that a cooling-air passage equivalent to a 3/32-inch-diameter hole (0.0069 square inch) is required to feed each blade. This consideration would amount to a small increase to the blade tensile stress in the inner tang and outer tang.

The critical stresses--those most likely to cause failure--are the combined fillet stresses and the maximum combined fillet stresses. The combined fillet stress is the effective Heywood stress combining the tensile and bending stresses in the fillet region. The maximum combined stress includes the effect

TABLE VII. FIR-TREE STRESS SUMMARY

Type of Stress	Blade Stresses, KSI			
	Outer Tang		Inner Tang	
	Nominal	Peak	Nominal	Peak
Tension	23.6	36.7	26.4	40.0
Bending	30.0	34.9	32.7	39.2
Comb. fillet	53.6	71.6	59.2	75.9
Max. comb. fillet	91.1	117.8	98.3	122.1
Shear	20.2	23.5	22.0	24.1
Bearing	41.4	48.1	47.0	51.5

Type of Stress	Disk Stresses, KSI			
	Outer Tang		Inner Tang	
	Nominal	Peak	Nominal	Peak
Tension	49.3	71.7	59.3	66.2
Bending	38.7	45.0	39.6	43.4
Comb. fillet	87.6	116.1	98.5	109.2
Max. comb. fillet	162.9	207.1	202.0	220.0
Shear	16.7	19.4	19.8	21.7
Bearing	41.4	48.1	47.0	51.5

NOTE: Refer to Figure 23 for location of stresses.

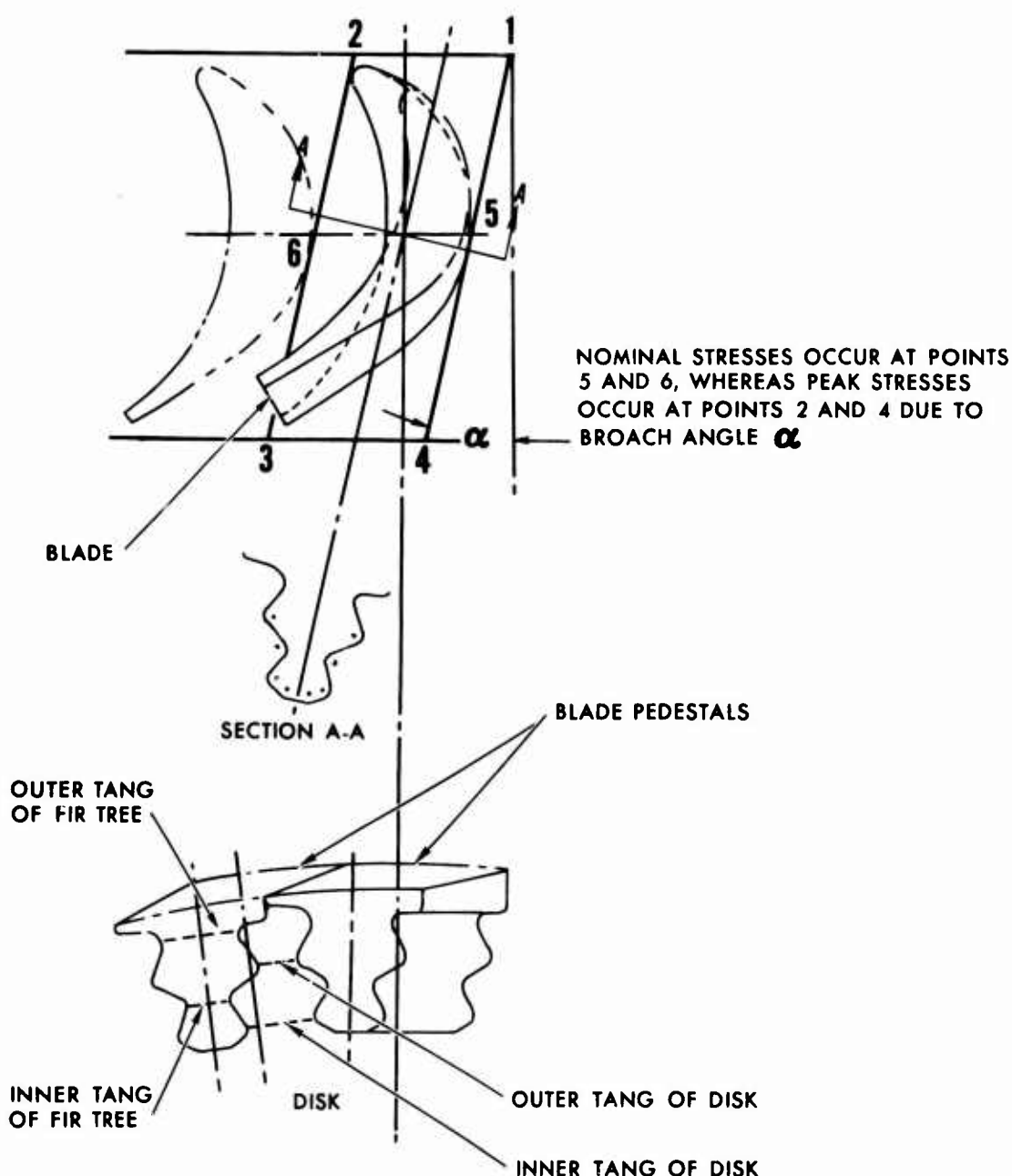


Figure 23. Stress Locations of Fir-Tree Disk Attachment Design.

of both tensile and bending stress concentration factors. The combined fillet stress is compared with the allowable rupture strength of the material, and the maximum combined fillet stress is compared with the low-cycle fatigue strength of the material.

Although no heat-transfer calculations of disk steady-state temperatures were made for this design, a reasonable estimate based on experience with similar designs would indicate a metal temperature of 1300° to 1350°F at the disk rim. Typical gradients in the radial direction are 500° to 700°F per inch, and the temperature drop from blade to disk is usually about 50°F at a given radius. These assumptions and the use of MAR-M 246 castings for the blades and Astroloy forgings for the disk permitted calculation of the safety margins shown in Table VIII.

Allowable stresses (creep-rupture and low-cycle fatigue) for the MAR-M 246 were assumed to be the same as for IN-100, since there is insufficient data available to establish realistic minimums. In the absence of available data for Astroloy, it was assumed that the low-cycle fatigue strength is comparable to that for Waspaloy.

It is apparent from Table VIII that negative margins of safety exist in the disk, the worst being due to the combined fillet stress at the outer tang. This is primarily due to the large tensile stress there. There is very little that can be done to improve this situation, since the axial length of the fir tree is the full chord length of the blade. Larger axial dimensions would only necessitate a larger disk to carry the load. In view of the prohibitive stress factors, the mechanical attachment evaluation was discontinued. Further investigation was confined to brazing, welding, and diffusion-bonding techniques.

3.3.2 Diffusion Bonding

As found in the literature survey, recent research efforts have been conducted to develop methods of solid-state diffusion bonding. These methods all depend on the effects of pressure, temperature, and time at the joint interface. The success of the diffusion-bonded joint concept depends strongly on the ability to maintain intimate contact between very smooth surfaces during the bonding operation. Methods have been pursued in an effort to eliminate the need for precisely mated surfaces and to relax the requirements of surface finish.

TABLE VIII. SUMMARY OF SAFETY MARGINS

Location	Stress Type	Estimated Temperature (°F)	Allowable* Stress (KSI)	Peak Stress M.S.**
Blade outer (MAR-M 246)	Comb. fillet	1300	79.0	71.6 +0.10
	Max. comb. fillet	1300	140.0	117.8 +0.19
Blade inner (MAR-M 246)	Comb. fillet	1200	93.0	75.9 +0.22
	Max. comb. fillet	1200	140.0	122.1 +0.14
Disk outer (Astroloy)	Comb. fillet	1200	100.0	116.1 -0.14
	Max. comb. fillet	1200	205.0	207.1 -0.01
Disk inner (Astroloy)	Comb. fillet	1100	116.0	109.2 +0.06
	Max. comb. fillet	1100	205.0	220.0 -0.07

*Based on 1000-hr stress-rupture strength or 0.2 percent offset yield strength for combination fillet stress and 1000-cycle strength for maximum combination fillet stress.

**M.S. = $\frac{\text{allowable stress}}{\text{peak stress}} - 1$

The gas pressure bonding process, which has been developed extensively at Battelle Memorial Institute, provides an isostatic load application and for certain joint geometry, allows the relaxation of surface mating conditions. This is accomplished wherein at least one of the joint elements has compliance under application of the bonding parameters and thus conforms to the mating surface.

The use of interface diffusion aids with certain material combinations shows promise of obtaining higher joint strengths for a given surface condition, or alternatively permits a less precise surface finish for realization of a given joint strength.

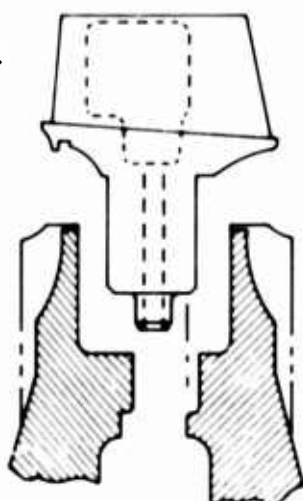
In view of these recent advances in technology, the diffusion bonding technique was selected as a candidate joining method. Prior to the preliminary test evaluations of Section 4.2, analyses were performed to determine the temperature distribution and stress levels of a diffusion-bonded rotor design, as reported in Section 3.4.

Figure 24 shows the most attractive concept of those studied for diffusion bonding. Although other lighter weight concepts were considered, this design was chosen because of the ideal geometry that it provides for fixturing and for applying the bonding load. Concepts utilizing diffusion bonding, wherein the load is applied in a direction other than axial, are inherently deficient in bond area and, in the case of a radially applied load, are probably incapable of supporting the required bonding load through the blade and/or pedestal. The chosen concept may be subjected to loads that produce small deformation, if required for bonding strength, without affecting the integrity of the rotor design.

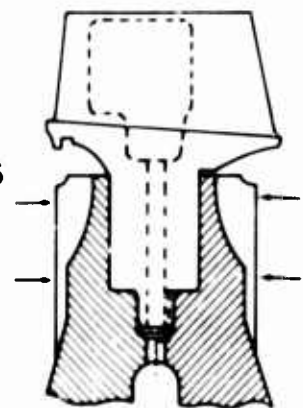
To reduce stress concentration in the rim region, holes and slots are provided as for the other attachment designs. The blade pedestal extensions are spaced 0.003 to 0.005 inch apart during bonding. The disk halves are considered to be slotted and have holes drilled prior to bonding for ease of machining and to provide compliance between disk and blade elements. If bonding load is applied mechanically, it is believed that all blade pedestal extensions must be ground with a common set-up in order to provide for uniform loading of elements during bonding. If gas pressure bonding were utilized, the compliance offered by the slots and holes could allow small variations in the blade pedestal extension dimensions without affecting the bonding characteristics appreciably from blade to blade.

SEQUENCE OF WHEEL ASSEMBLY VIEWS

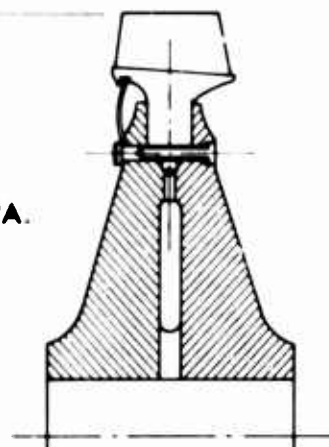
COMPONENTS PRIOR TO DIFFUSION BONDING



DISC JOINT SURFACES FINISH MACHINED AND COMPONENTS DIFFUSION BONDED



7.32 DIA.



WHEEL ASSEMBLY

HOLES MACHINED, DISC FINISH MACHINED AND SEGMENTED AIR SEAL INSTALLED

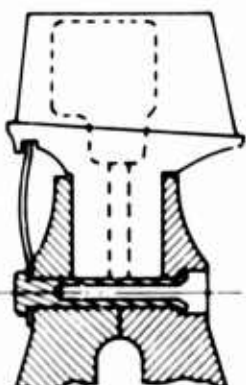


Figure 24. Diffusion-Bonded Design.

Advantages and disadvantages of this design are:

1. Advantages

- (a) Because of the parallel-sided bond surface design, fixturing and surface preparation are simple and easy to control.
- (b) Analysis of the joint is simple, since it is in pure shear.
- (c) Cooling-air access is simple, since each blade can be cored completely prior to joining.

2. Disadvantages

- (a) Inspection is difficult, since X-ray, ultrasonic, and other nondestructive techniques cannot adequately define areas of incomplete bonding. Whirlpit testing can be used to discover gross defects in the bond, but will not reveal the small stress concentrations that affect low-cycle fatigue behavior and stress-rupture life.
- (b) The disk must be slotted and drilled at the inner boundary of the joint to prevent low-cycle fatigue failures in disk rims.
- (c) The design is relatively heavy.
- (d) To ensure uniform bonding, blade elements may have to be ground in matched sets.

The design of a turbine rotor that incorporates the diffusion bonding attachment concept is described in Section 3.4.

3.3.3 Brazing

Brazing of nickel-base alloys for high-temperature operation has long been used for static structures such as gas turbine stators, bearing support frames, and other parts. However, its use for highly stressed rotor parts has been virtually nil due to the low rupture-strength and fatigue-strength properties in most joint designs. Over the past few years, however, reliable joints have been made with vacuum brazing techniques with the use of new brazing alloys and close control of the process variables.

Preliminary calculations based upon joint properties reported in the literature and approximate attachment geometry suggested that a satisfactory attachment could be designed with the use of a brazed joint. Thus, brazing was selected as one of the candidate joining techniques. Prior to the preliminary test evaluations of Section 4.2, analyses were performed to determine the temperature distribution and stress levels of a brazed rotor design, as reported in Section 3.4.

The brazed-joint design selected is shown on Figure 25. This design was chosen since it best provides the large joint area required, and additionally provides a natural radius between each blade to mitigate the stress concentration effect at the rim of the disk. The design concept utilizes a split disk, which is joined by electron-beam welding. The depth of this weld is minimized by machining a 0.300-inch-deep groove in the periphery of the disk prior to welding. The bottom of this groove then becomes the maximum diameter of the welded surface. After final machining of the disk, this groove divides the surfaces to be brazed into four separate and essentially equal areas. This has the desirable effect of providing smaller areas over which the alloy must flow, and as such, should reduce the possibility of incomplete bonds due to incomplete wetting of the surfaces. Additionally, this groove simplifies the coolant entry path to the blade. Coring in the blade pedestal may be designed to provide a passage having considerable overlap over the disk groove, and therefore, would require less precise positioning, so that a certain amount of core shift could be tolerated. Coolant enters the groove through holes drilled in each disk attachment projection.

The blade pedestals have thin webs cast at each end, which prevent bypass flow of the working fluid through the cavities between blades. A small gap (0.003 to 0.005 inch) is allowed to exist between each pedestal to prevent undesirable loading from thermal-growth effects. The design shown on Figure 25 would allow excessive leakage at both root and tip of the disk attachment projections. These regions were left undefined because of the uncertainty of fillet effects from excess braze alloy. Sealing of these regions could be resolved by further development.

Advantages and disadvantages of this concept are:

1. Advantages

- (a) The joining process is inherently simple.

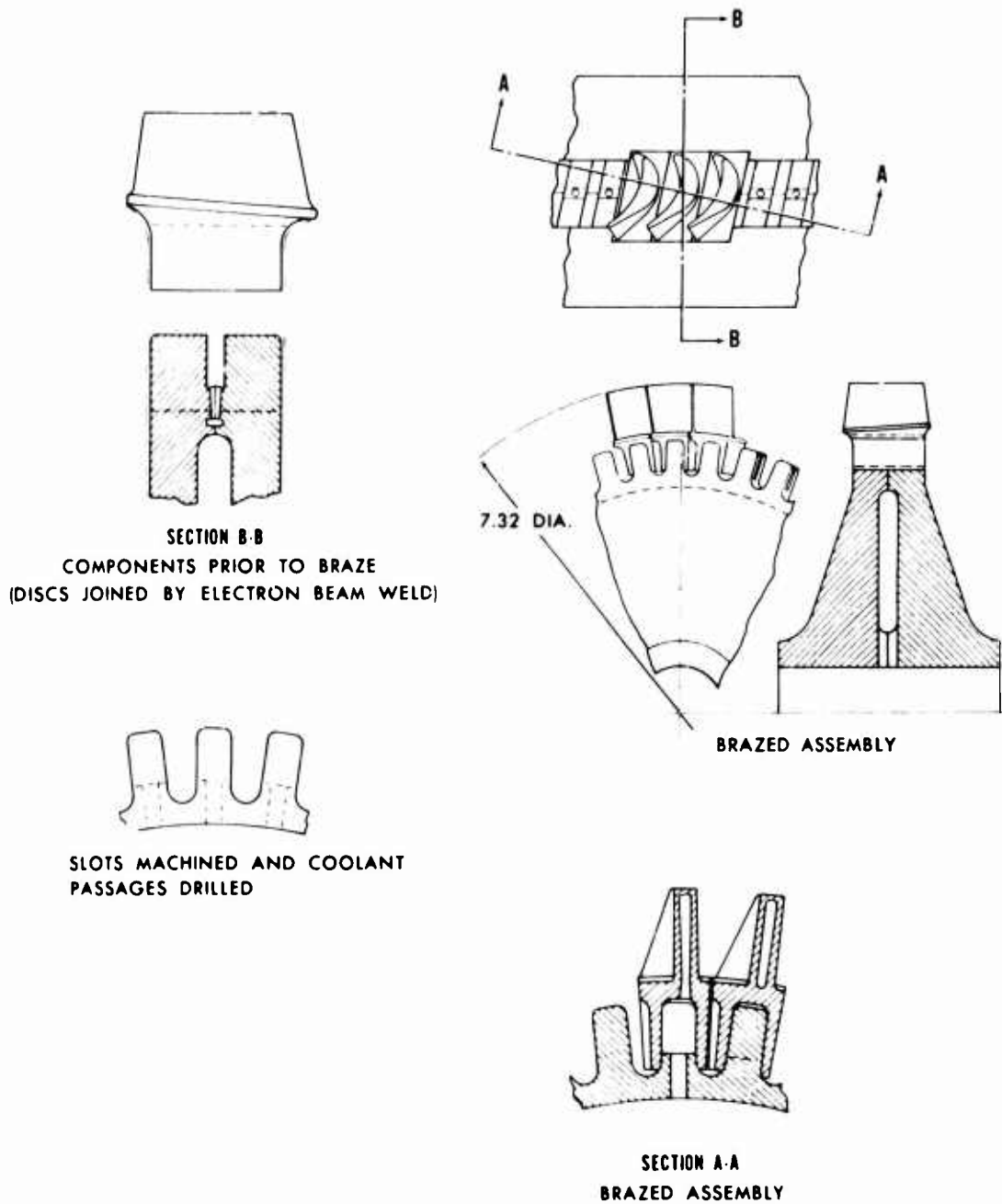


Figure 25. Brazed-Joint Design.

- (b) The brazed joint is in pure shear, which eliminates the "peeling" effect that is inherent with many brazed designs.
- (c) Machining of the attachment on both blade and disk is simplified because of the parallel joining surfaces, and close dimensional control of the braze gap should be feasible at minimum cost.

2. Disadvantages

- (a) The discovery of small voids and areas that would result in stress concentrations in the joint is not feasible by nondestructive inspection methods such as X-ray and fluorescent-penetrant.
- (b) A relatively heavy disk is required.

The design of a turbine rotor that incorporates the brazed attachment concept is described in Section 3.4.

3.3.4 Electron-Beam Weld

An examination was conducted to evaluate welding processes for use as a joining method in the blade/disk attachment. Of the welding processes evaluated, (electron beam, inertia, explosive, and laser beam), the electron-beam-welding process was considered to be the most effective and was the process selected for use in this program. Reasons for this selection were:

1. More experience has been obtained on the joining of nickel-base alloys with use of electron-beam welding than for other applicable welding processes.
2. Less heat input is generated to the welded assembly by electron-beam welding than by other applicable welding processes. This provides an important advantage in minimal distortion, and minimized weld joint cracking should also be obtained.
3. The minimized weld zone produced by the electron-beam-welding process facilitates joint inspection by radiographic techniques.
4. Fixturing requirements for the pre-weld assembly are relatively simple in comparison to those required for other applicable welding processes.

5. A considerable amount of experience has been accumulated in recent years with the electron-beam welding of components having geometry similar to that of the turbine rotor designed for this program.

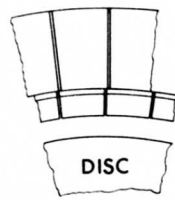
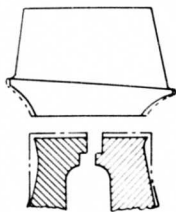
Prior to the preliminary test evaluations of Section 4.2, analyses were performed to determine the temperature distribution and stress levels of an electron-beam-welded rotor design, as reported in Section 3.4. The electron-beam-welding concept selected is illustrated in Figure 26. The disk halves are first joined by a girth weld. Then with the disk and blade pedestals in the premachined condition, the blades are fixtured around the periphery of the disk and spaced 0.003 to 0.005 inch apart. A single pass full-penetration (0.79-inch), circumferential weld is then made. The disk faces are then finish-machined (0.050-inch cleanup at weld), and holes are drilled in line with the slots between blades and centered on the weld. These holes thus remove weld flash at the space between blades and reduce the stress concentration in the same fashion as on integrally cast wheels. Bypass of the main gas flow through the holes is prevented by sealing each hole with a rivet. The 0.003 to 0.005-inch slots remaining in the disk rim allow only negligible bypass leakage and are considered to be sufficient to prevent bending or compressive stresses from developing as a result of mechanical interference induced by thermal transients.

This concept facilitates inspection of the weld by providing a section through the weld zone on both sides and on each end of each blade attachment. Flaws in the weld and/or heat-affected zone are easily detected by fluorescent-penetrant inspections.

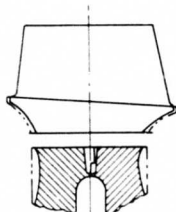
Use of the split-disk design provides a simple flow path for the blade cooling air from the shaft. For the blade cooling scheme utilized in this assembly, the relatively large cored cavity in the blade permits insertion of electrical-discharge-machining tooling through the tip of the blade so that a passage may be machined to connect the cored blade cavity and the disk cavity and thus complete the cooling-flow circuit.

SEQUENCE OF WHEEL
ASSEMBLY VIEWS

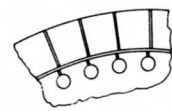
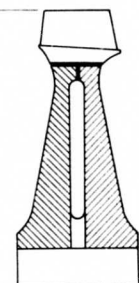
COMPONENTS PRIOR
TO WELD



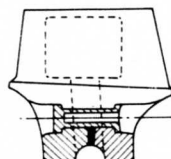
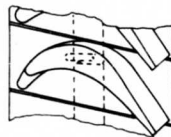
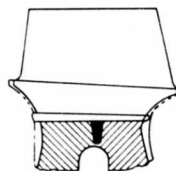
DISCS JOINED BY
GIRTH WELD AND
FINISH MACHINED
PRIOR TO BLADE
ATTACHMENT



7.32 DIA.



BLADES JOINED
TO DISC BY
CIRCUMFERENTIAL
WELD



RIM HOLES MACHINED,
RIVETS INSTALLED, AND
COOLING-AIR PASSAGES
ELECTRICAL-DISCHARGE
MACHINED
DISC FINISH MACHINED

Figure 26. Electron-Beam-Welded Design.

Advantages and disadvantages of this concept are:

1. Advantages

- (a) Fit of blades and disks prior to welding is easy to obtain.
- (b) Analysis of the joint is simple, since the weld is in pure tension.
- (c) Inspection of the joint by X-ray with a single film exposure, plus a fluorescent-penetrant inspection of all four sides of each blade attachment, ensures quality control.
- (d) Weld joint strength is potentially equal to that of the weakest member being joined.
- (e) Past experience with use of similar design configurations for the blade pedestals was successful.

2. Disadvantages

Access of cooling air is difficult to obtain, since the weld must be opened by inserting an Elox tool through each blade core.

The design of a turbine rotor that incorporates the electron beam welding attachment concept is described in the following section.

3.4 TURBINE ROTOR DESIGN

Three rotor designs were selected for evaluation with diffusion-bonding, brazing, and electron-beam-welding attachment methods to a split disk. The split-disk approach offers an ideal method of supplying cooling air to the blades. For each design, the attachment cross sections were designed to minimize the radial load on the disks while maintaining the design stress level in the joint.

3.4.1 Rotor Temperature Distribution

Rotor temperature distributions were computed for the three selected rotor designs. The analytical model for each design was an equivalent disk with accurate geometric approximations for the attachment area, blade strut area, and blade pedestal. At the time of this analysis, the disk contour and thickness were not yet defined. For this reason, a common typical disk design was used for each of the three design configurations analyzed. The isotherms were not corrected to the final disk shapes, since the effect on the attachment temperature is considered to be insignificant.

Neglecting the disks, the three design configurations differ primarily in the blade/disk attachment region. Therefore, the analytical models also differed primarily in the blade attachment region to obtain a valid approximation for the particular geometry under consideration. The analysis for each design configuration was two-dimensional (axial and radial); thus, the small circumferential temperature variations in the attachment region were not considered. This axisymmetric geometric assumption is not considered an analysis deficiency, since all geometric characteristics and blade coolant channels are accurately approximated with the equivalent axisymmetric disk analytical model.

Rotor isotherms for diffusion-bonded, brazed, and electron-beam-welded design configurations are shown in Figures 27, 28, and 29, respectively. General observations for all three isotherm patterns are similar. At small radii, rotor temperatures are only slightly above cooling-air inlet temperature, which was assumed to be 800°F. As radius increases, both rotor temperature level and temperature gradient increase, as can be expected. The strut isotherms agree with the strut temperatures presented in Section 2.

The coolant flow rates shown correspond to the disk pumping and blade coolant flow rates defined in the trade-off study. All three analyses included a heat balance on each of these cooling flows. Disk film coefficients were computed from conventional rotating disk heat-transfer correlations.

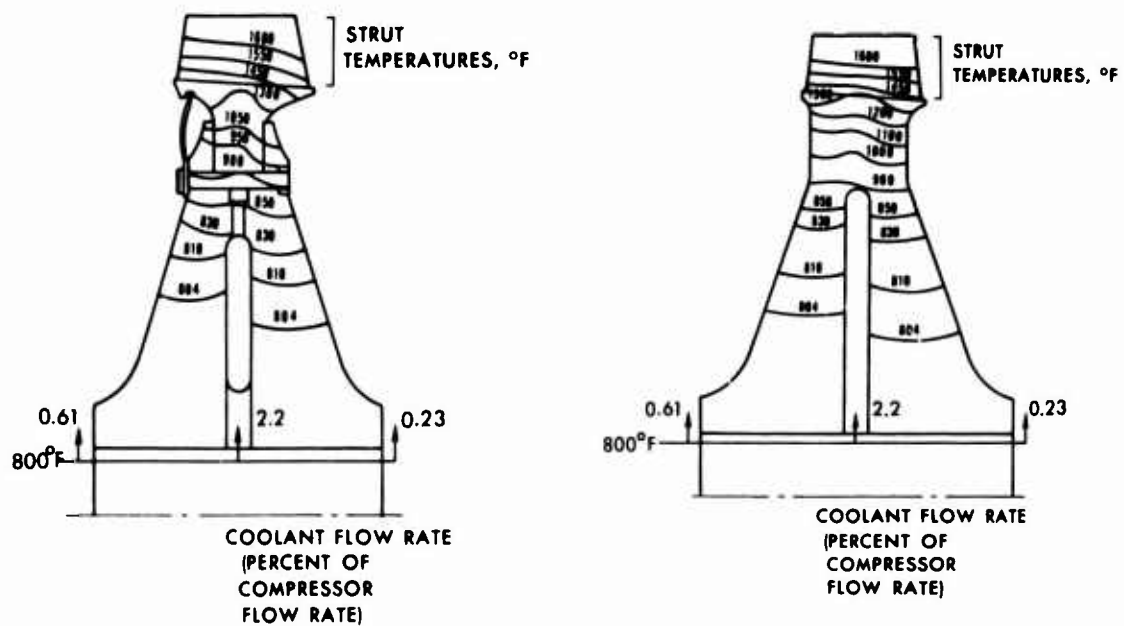


Figure 27. Rotor Isotherms, Diffusion-Bonded Design.

Figure 28. Rotor Isotherms, Braze Design.

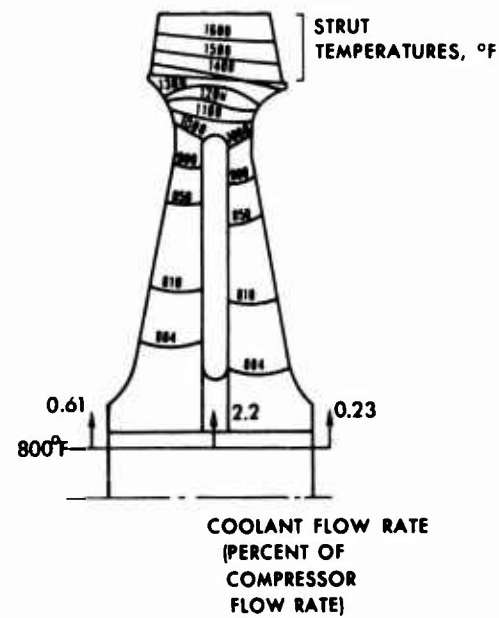


Figure 29. Rotor Isotherms, Electron-Beam-Welded Design.

3.4.2 Stress Analysis

The radial stresses in the attachment region were calculated as if the centroids of the sections lie on a radial line. Use of this approach minimized the centrifugal bending stresses. The nominal centrifugal stress distributions for each design are shown on Figures 30, 31, and 32, together with the disk stresses. The peak stresses in the electron-beam-welded design and diffusion-bonded design occur at the center of the rivet holes, whereas the radial stress in the brazed-joint design peaks at the root of the joint. The radial rim stress at the disk boundary is seen to be 60,000 psi for both the brazed-joint design and the diffusion-bonded design. The radial rim stress for the electron-beam-welded design is only 38,000 psi.

In each design configuration, the governing factor is the design stress level in the joint. These were chosen to be:

Diffusion bond	35,000 psi (shear)	MAR-M 246 to INCO 718
Braze	17,500 psi (shear)	MAR-M 246 to Waspaloy
Electron-beam weld	58,000 psi (tension)	MAR-M 246 to Waspaloy

The choice of these stress levels was based primarily on the results obtained from preliminary test evaluations modified by an estimate of changes expected in the final test results. The values used for design reflect not only the mean strength levels determined, but also the spread or variance observed.

At this time, a rotating disk design computer program, based on the work of Monson,⁸ was used to determine the thickness of the split-disk designs. This program uses a plane stress analysis to determine the optimum disk thickness distribution that satisfies the desired equivalent stress distribution (based on the maximum strain energy of distortion theory) for the radial temperature gradient and radial rim loading imposed. A bore diameter of 1.0 inch was arbitrarily selected for the study.

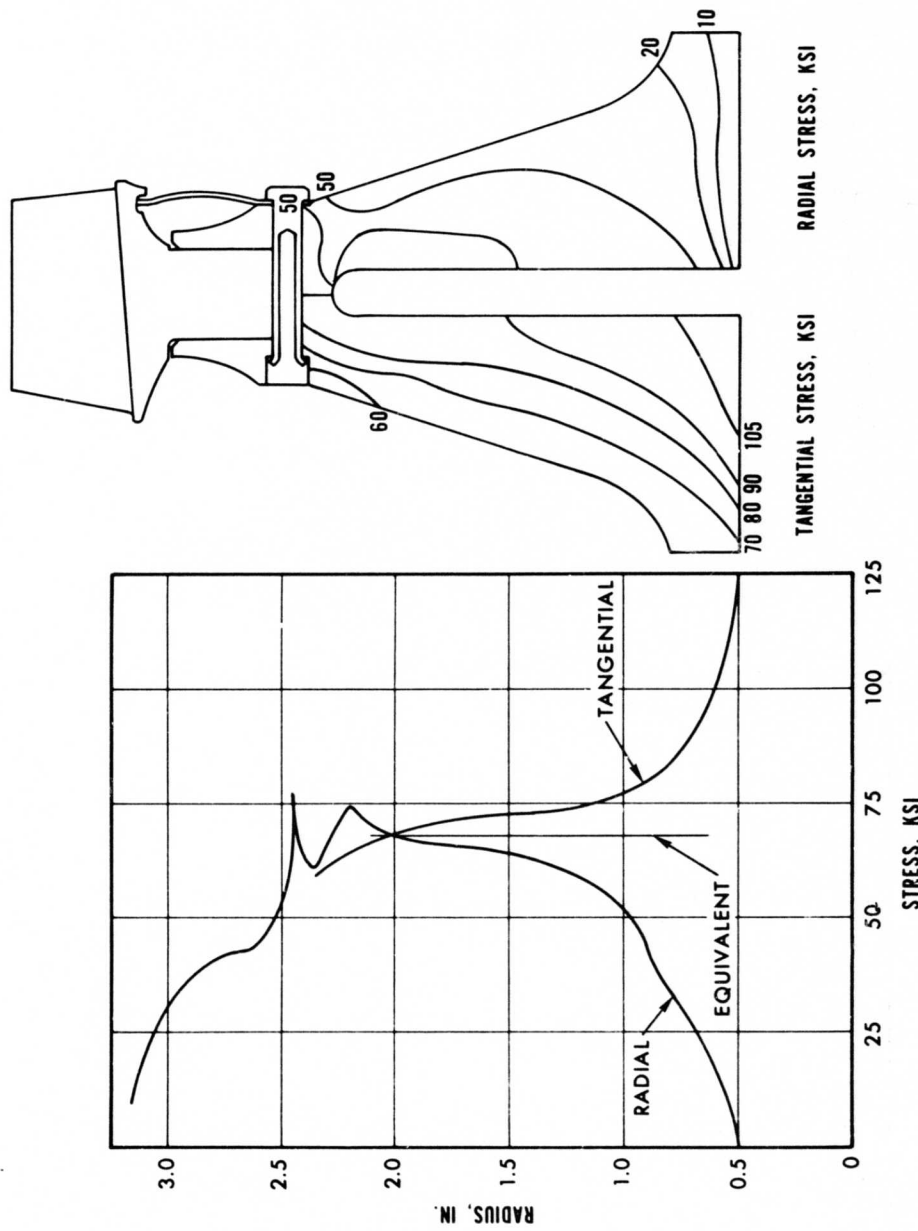


Figure 30. Nominal Centrifugal Stress Distribution for Diffusion-Bonded Design.

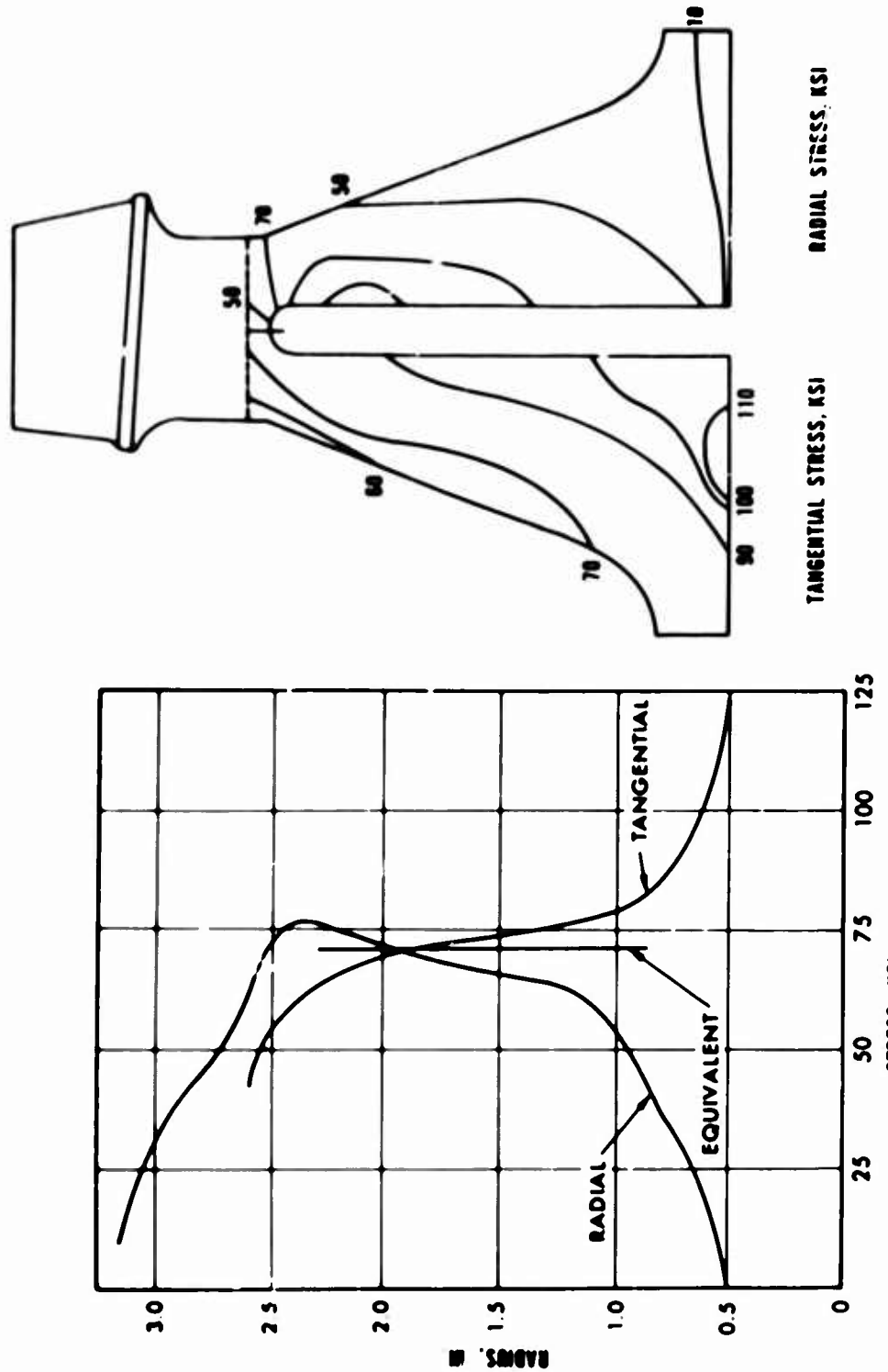


Figure 31. Nominal Centrifugal Stress Distribution for Brazed-Joint Design.

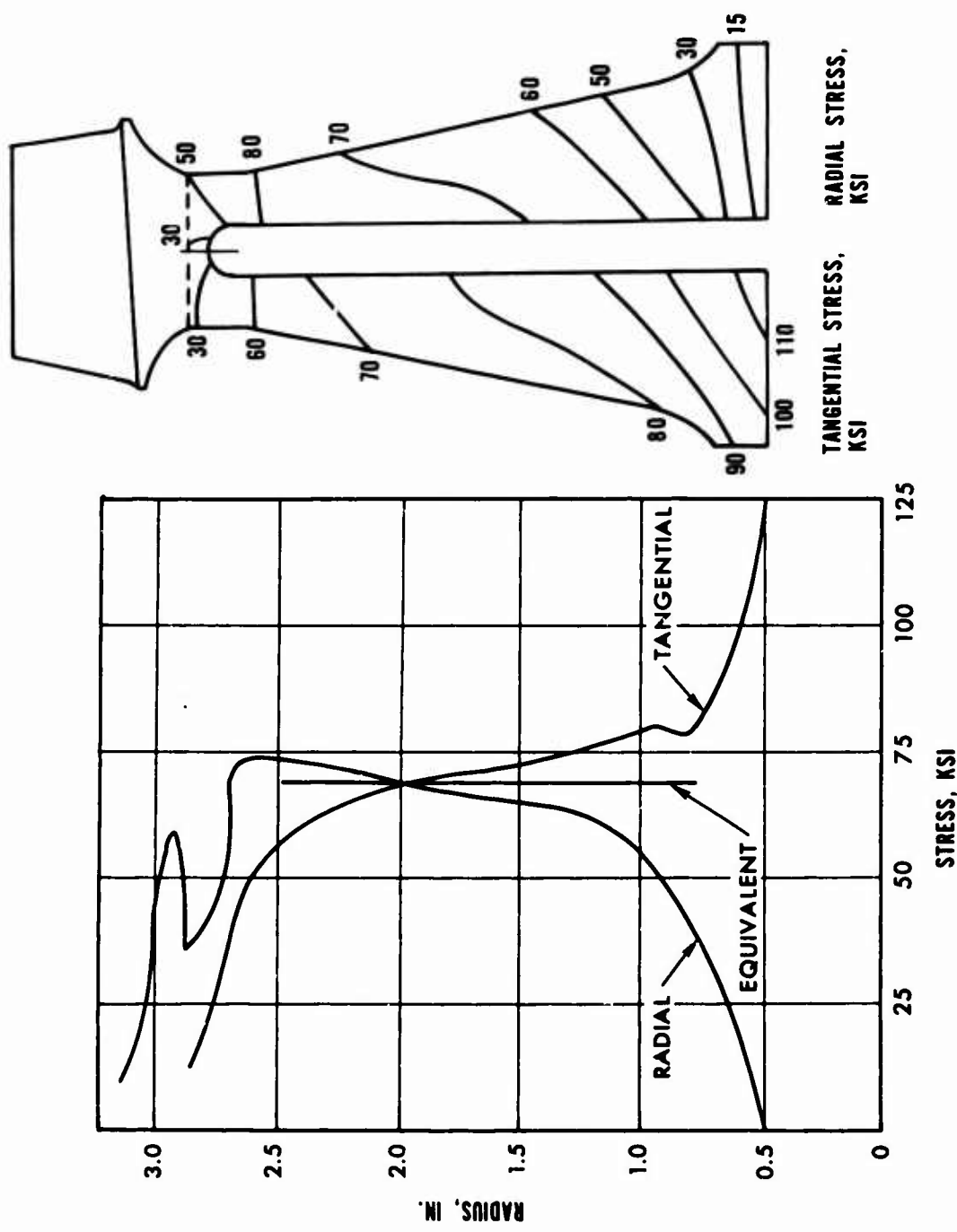


Figure 32. Nominal Centrifugal Stress Distribution for Electron-Beam-Welded Design.

The allowable stresses at design speed (46,900 rpm) used for the analysis were based on the following criteria:

1. Except at the bore, all equivalent stresses based on the maximum energy of distortion theory of failure were not to exceed the lowest value determined from
 - (a) 77 percent of the minimum* 0.2-percent offset yield strength.
 - (b) 100 percent of the minimum stress-rupture strength of the material at twice the required overhaul life (2×1000 , or 2000 hours).
2. At the bore, the tangential stress could not exceed 125 percent of the minimum 0.2-percent offset yield strength.
3. The average tangential stress in the disk could not exceed a value calculated to provide a minimum disk burst speed of 125 percent. This is obtained from the following relationship:

$$\frac{N_B}{N_D} = \sqrt{\frac{F_{tu}}{\sigma_t}} \quad (\text{burst factor}) \quad (13)$$

where N_B = burst speed

N_D = design speed

F_{tu} = average ultimate tensile strength of disk material

σ_t = average tangential stress at design speed

4. The burst factor is determined from burst tests of similar disk designs of the same material.

*All minimum-strength values are taken as three standard deviations below nominal.

From the radial loading and radial temperature gradients used, it became apparent that the average tangential stress in the disk (burst-speed criteria) governs the design rather than the equivalent stress in the disk.

Each of the three disk designs was analyzed by a finite-element computer program to determine the three-dimensional stress and deflection of each element. The radial and tangential stress distributions from this analysis are also shown in Figures 30, 31, and 32. The weights, polar moments of inertia, and bore widths for the three designs are compared in Table IX.

It can be seen from the data presented in Table IX that the electron-beam-welded design is by far the lightest and has the lowest polar moment of inertia. The diffusion-bonded design appears superior to the brazed-joint design in this regard. However, the brazed-joint design stress levels selected may be subject to change in some cases as a result of the final test data.

TABLE IX. WEIGHTS, POLAR MOMENTS OF INERTIA, AND BORE WIDTHS FOR THE THREE ROTOR DESIGNS

Design	Airfoils (44)	Attachment (44)	Disk	Total
Electron Beam				
Weight, lb	0.67	1.63	5.02	7.32
I_p , lb-in-sec ²	0.0202	0.038	0.0448	0.1030
Axial width, in.			1.60	
Diffusion Bond				
Weight, lb	0.67	3.17	5.73	9.57
I_p , lb-in-sec ²	0.0202	0.062	0.0358	0.1190
Axial width, in.			2.20	
Braze Joint				
Weight, lb	0.67	3.28	6.93	10.88
I_p , lb-in-sec ²	0.0202	0.0705	0.0507	0.1414
Axial width, in.			2.60	

4. FABRICATION TECHNOLOGY DEVELOPMENT

This section describes a fabrication technology development effort that was conducted in parallel with the mechanical design and analyses described in Section 3. The objectives of this parallel activity were:

1. To select several suitable material types that could be utilized for fabrication of a disk, cast/cored blade or strut, and sheet metal blade shell.
2. To conduct preliminary testing in order to determine the most advantageous material types and blade/disk joining methods and to evaluate shell/strut joining methods.
3. To obtain potential joint-strength data that would aid in the design and fabrication of the final test specimens and in the design of the turbine rotors.

As stated in the introductory remarks of Section 3, even though this program was directed toward development of blade/disk attachment methods, some consideration was given to shell/strut joining, since the aerodynamic optimization study suggested the use of a strut-supported sheet metal blade. Therefore, preliminary testing was conducted to evaluate both the blade/disk and shell/strut attachments.

It should be noted that in the text of this section, all references to the strut or strut/disk attachment are directly applicable to a cast/cored blade or blade/disk attachment. A cast/cored counterpart of the subject sheet metal blade may result in (a) a slight increase in total blade weight, and (b) for the same coolant flow rate, a slight increase in metal temperature compared to that of the subject sheet-metal-blade supporting strut. For the same attachment configuration, these minor differences compound to reduce stress-rupture life in the attachment by (a) increasing the attachment metal temperature and (b) increasing the stress in the attachment to carry the additional blade load. For the same stress-rupture life, the rotor assembly would increase in size. However, the technology gained from the material selection evaluations and preliminary attachment test data for the sheet-metal-blade supporting strut is directly applicable to the fabrication and disk attachment of a cast/cored blade.

4.1 SELECTION OF MATERIALS

An investigation was conducted to select suitable materials for fabrication of the disk, strut, and sheet metal blade. The primary consideration for the disk material was adequate tensile strength up to 1200°F. Strut materials were required to have good stress-rupture properties along with tensile properties, and the sheet metal blade material was required to have hot-corrosion resistance, to be coatable, and to have reasonably good tensile and creep properties. In addition, materials for each of the three components were required to be compatible with selected joining processes.

A number of materials were considered for each component, with the final decision being made on the basis of design requirements and fabrication parameters. The chemical compositions for the selected materials are given in Table X.

4.1.1 Disk Materials

Three materials were considered for the disk application: Inconel 718, Waspaloy, and AF2-1DA. All three are wrought nickel-base alloys that maintain good tensile properties up to at least 1200°F. The relative tensile strengths as a function of temperature for these alloys are shown in Figures 33 and 34. Both Inconel 718 and Waspaloy are commercially available alloys. The alloy AF2-1DA, however, is a more recently developed alloy, on which fabrication and property data is more limited. This alloy was selected for further evaluation, since it offers an apparent property advantage over the other two alloys.

4.1.2 Strut Materials

The material given primary consideration for the strut application was the alloy MAR-M 246. This is a cast nickel-base alloy having stress-rupture properties superior to other commercially available alloys, as indicated in Figure 35.

4.1.3 Sheet Metal Blade Materials

Three materials were considered for the blade application: René 41, AF2-1DA, and AiResist 213. The first two of these alloys are high-strength wrought nickel-base alloys. AiResist 213 is a wrought cobalt-base alloy, which has superior hot-corrosion resistance, although its mechanical properties are inferior to those of René 41 and AF2-1DA. Mechanical properties for these alloys are indicated in Figures 33, 34, and 35.

TABLE X. NOMINAL CHEMICAL COMPOSITIONS
FOR CANDIDATE ALLOYS

Element	Inconel 718	Waspaloy	AF2-1DA	René 41	MAR-M 246	AiResist 213
Ni	Bal	Bal	Bal	Bal	Bal	0.5 max
Co	-	13.5	10.0	11.0	10.0	Bal
C	0.04	0.8	0.35	0.09	0.15	0.17
Mn	0.20	-	-	-	-	0.10 max
Si	0.30	-	-	-	-	0.20 max
Cr	18.6	19.5	12.0	19.0	9.0	18.0-20.0
Mo	3.1	4.3	3.0	10.0	2.5	-
W	-	-	6.0	-	10.0	4.7
Cb	5.0	-	-	-	-	-
Fe	18.5	-	1.00 max	-	-	0.5 max
Ti	0.9	3.0	3.0	3.1	1.5	-
Al	0.4	1.3	4.60	1.5	5.5	3.5
B	-	0.006	0.015	0.005	0.015	-
Zr	-	0.06	0.10	-	0.05	0.15
Ta	-	-	1.50	-	1.5	6.5
Y	-	-	-	-	-	0.07
Cu	-	-	-	-	-	0.30 max
S	-	-	-	-	-	0.015 max
P	-	-	-	-	-	0.015 max

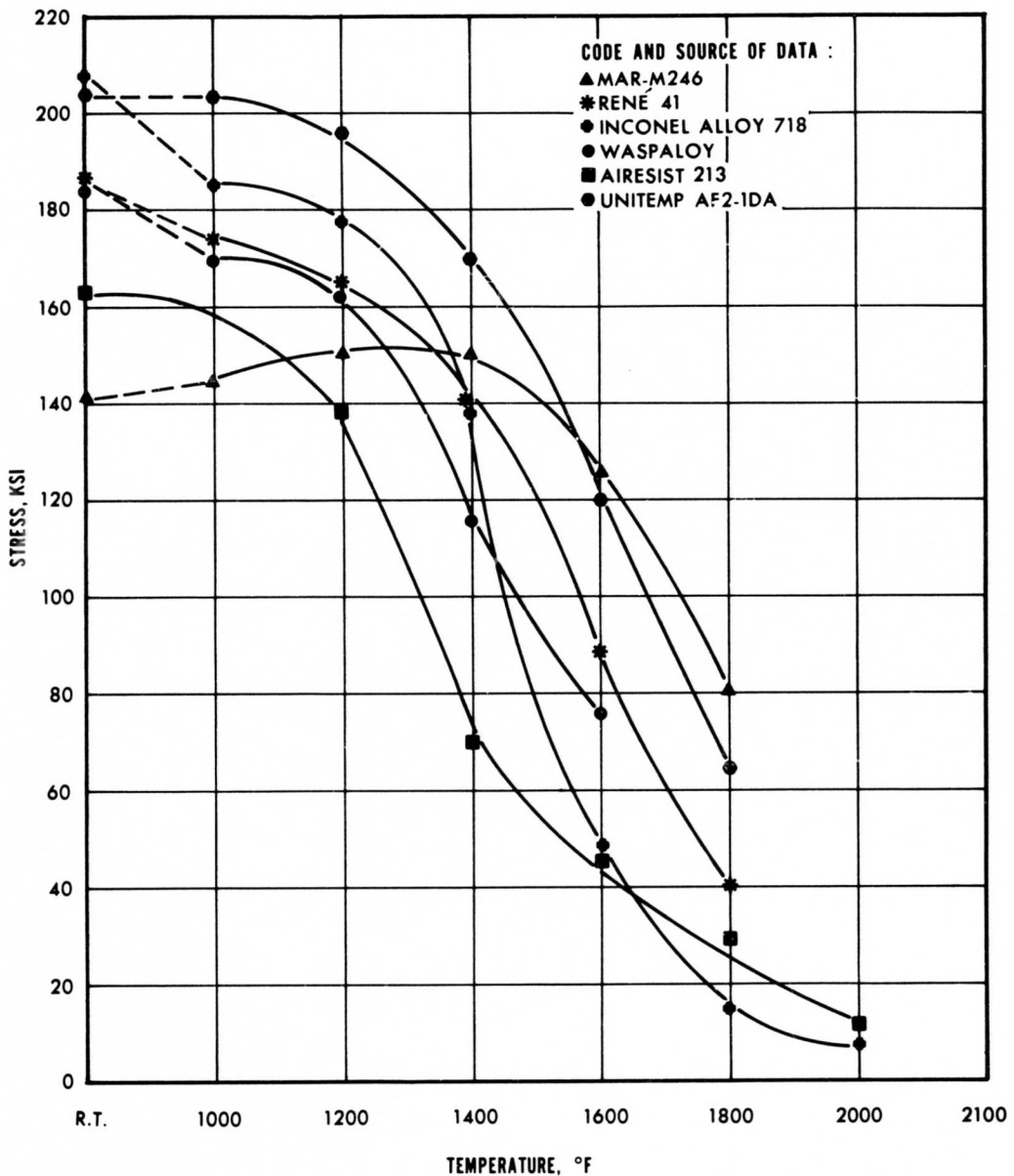


Figure 33. Ultimate Tensile Strengths for Candidate Materials.

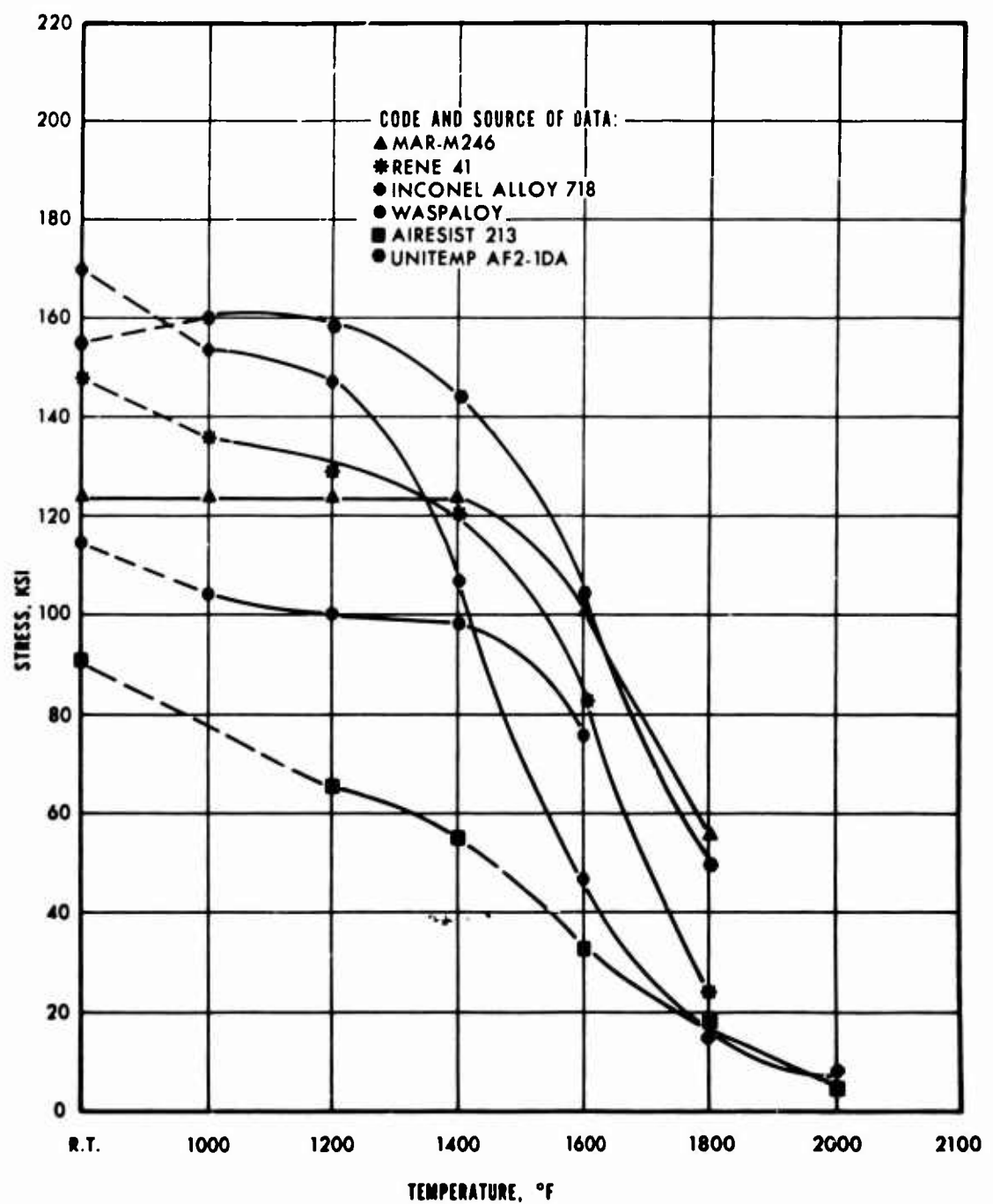


Figure 34. Yield Strengths (0.2% Offset) for Candidate Materials.

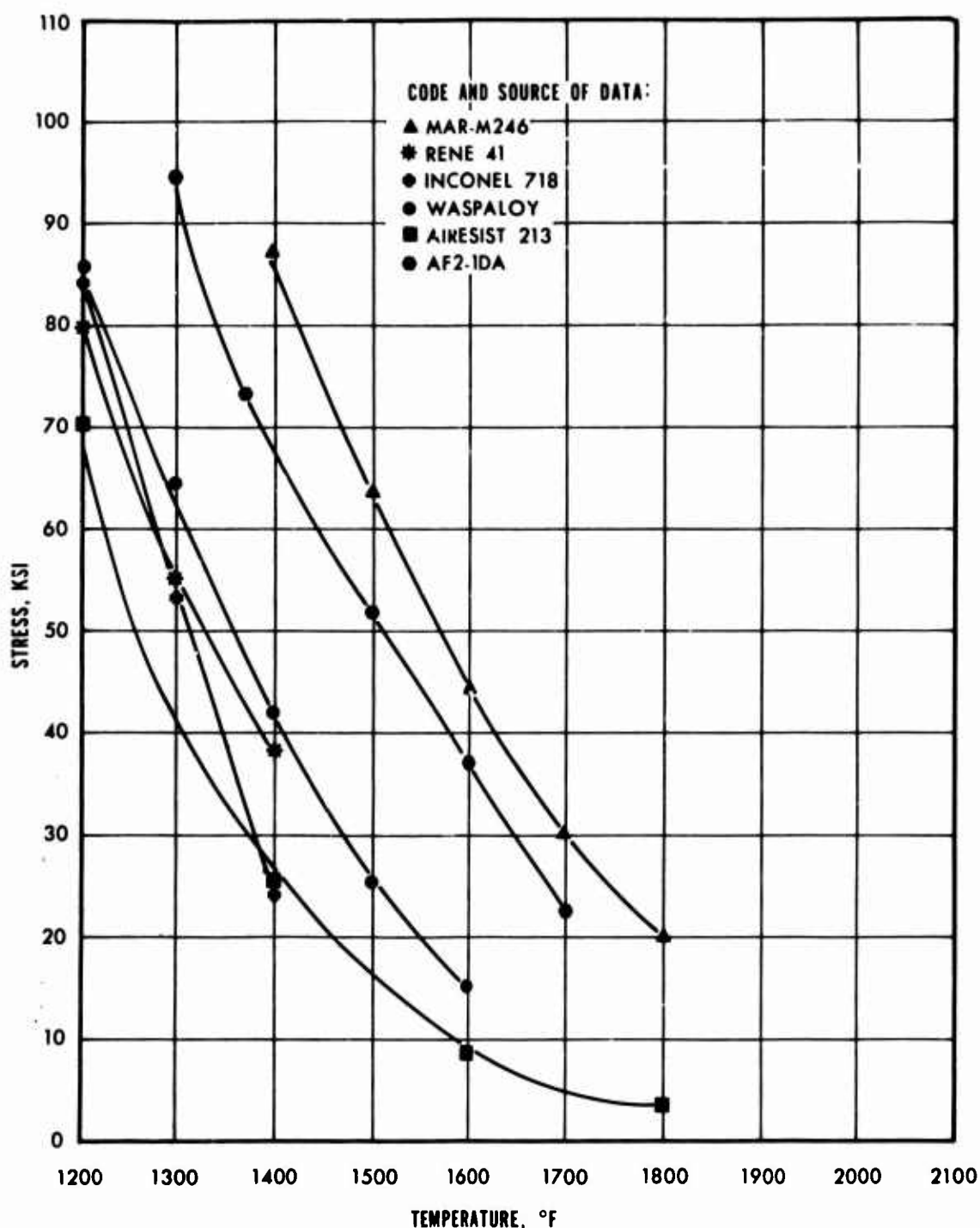


Figure 35. 1000-Hr Stress-Rupture Strengths for Candidate Materials.

4.2 PRELIMINARY TEST EVALUATIONS

For each selected strut/disk joining technique (diffusion bonding, brazing, and electron-beam welding), a series of preliminary fabrication and joint property tests was performed. In addition, an evaluation of cast bonding for the shell/strut application was conducted. Subsequent subparagraphs detail the results of these preliminary tests.

4.2.1 Diffusion Bonding

Diffusion bonding was considered for both the strut/disk and shell/strut joints. This joining technique offers some potential advantages over other methods, but is somewhat limited as to configurations which can be readily bonded. A design for the strut/disk joint was considered which would allow unidirectional loading to form the bond. The shell/strut joint, however, would likely require isostatic pressure to collapse the sheet metal shell against the strut and maintain sufficient pressure to form the bond. In either case, preliminary information was required on bond strengths which could be expected from the alloys of interest.

4.2.1.1 Experimental Procedure

In order to develop data for the preliminary screening of materials and bonding parameters, an overlap specimen and a pressing die in which to form it were designed as shown in Figure 36. The specimens were prepared from 0.050-inch-thick sheet materials and were polished to approximately a No. 3 rms finish on the surfaces to be bonded. The die was made of graphite and was heated by induction in the vacuum hot press furnace shown in Figure 37. Temperature was measured by a thermocouple placed in the die wall. A vacuum of less than 1 micron was maintained during the heating and pressing operation. The bonding procedure consisted of placing the assembled die (Figure 36) in the pressing furnace, evacuating the chamber to less than 1 micron, heating to the required temperature, and applying the load for the desired time. Bonded specimens were shear-tested by use of the test apparatus shown in Figure 38.

Three bonding parameters with bonding temperature maintained at 1800°F were evaluated: interface material, bonding pressure, and bonding time. Previously reported data had shown that bond strength could be improved by the use of a dissimilar interface material to serve as a "diffusion activator." Specimens were prepared with no interface material, with a 0.0005-inch nickel plate, and with a 0.001-inch-thick foil of a nickel plus 3-percent beryllium alloy. Bonding pressures were varied between 11,500 psi and 40,000 psi,

and bonding times were varied between 15 and 45 minutes. Two shear stresses were reported for each specimen. The "apparent shear stress" is that stress calculated on the basis of the total specimen overlap area. However, as a result of imperfect matching of surfaces, this total area was not completely bonded, in most cases. The "estimated actual shear stress" is therefore reported and is based on the estimated area of actual bond as determined by examination of the sheared surfaces. Material combinations evaluated initially are given in Table XI.

4.2.1.2 Test Results and Conclusions

Results of shear testing of the overlap specimens are given in Table XII. Material combinations of primary interest for the strut/disk joint included Waspaloy, Inconel 718, and AF2-1DA as disk materials joined to MAR-M 246 as a strut material. A summary of results of these combinations is given in Table XIII.

Difficulty in obtaining AF2-1DA in the required geometries precluded further material-combination evaluations utilizing this material type. Bonding data indicated the joint strengths of the Inconel 718/MAR-M 246 combination to be better than those between Waspaloy and MAR-M 246. The use of a thin nickel strike (0.0005-inch-thick) as an interface material gave consistently good strengths and a high percentage of bonded area, which indicates a tolerance for surface irregularities. This is an important consideration in the bonding of more complex geometries.

For these reasons, the final selection for diffusion-bonding evaluation was Inconel 718 joined to MAR-M 246 with a 0.0005-inch-thick nickel interface material. With use of these materials, the process was scaled up to specimens of a size similar to that required for the final test specimens. Figure 39 shows the larger specimen, and Figure 40 shows the die used to form it. These specimens were then further scaled up to the geometry shown in Figure 41, which exactly simulates the final specimen geometry. A typical bond produced in the final geometry is shown in Figure 42.

In order to develop full mechanical properties in the Inconel 718 disk material, the proper heat treatment was required. The fabrication procedure therefore consisted of bonding the specimens with the MAR-M 246 in the as-cast condition and the Inconel 718 in the solutioned condition. After bonding, the specimen was then given the proper heat treatment for the Inconel 718 material.

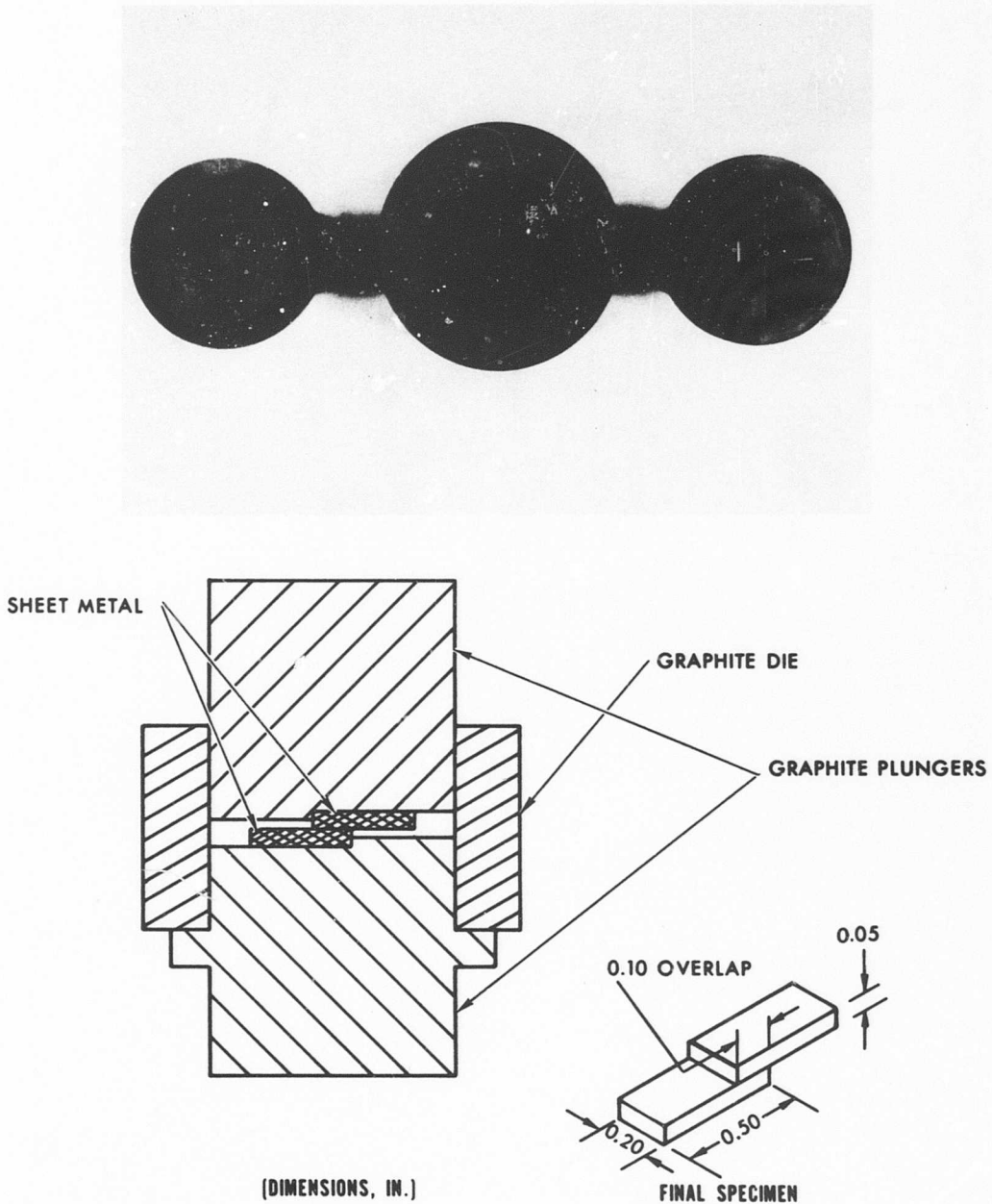


Figure 36. Pressing Die and Plunger Arrangement Used for Diffusion Bonding of Sheet Specimens.

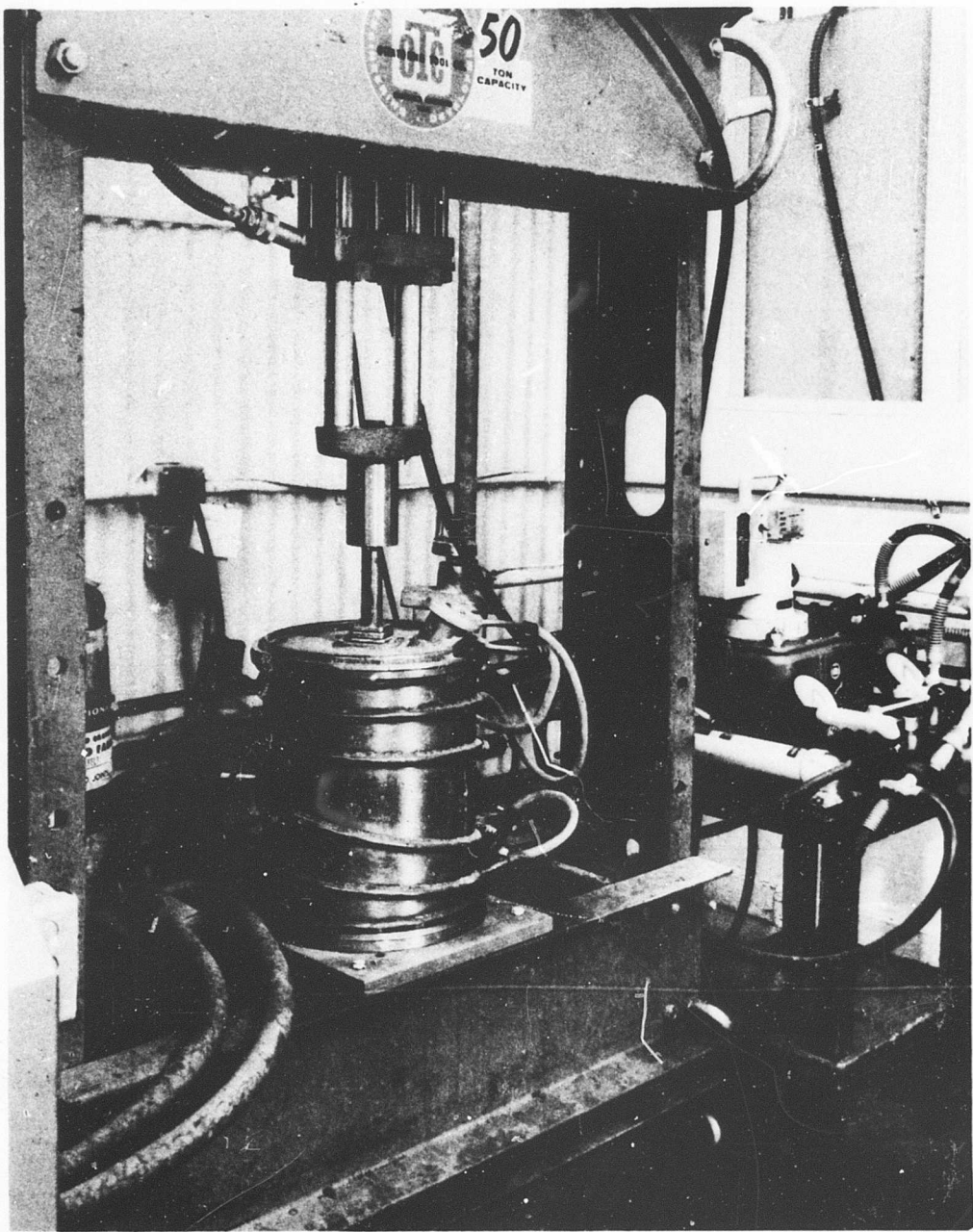


Figure 37. Vacuum Hot Press Furnace Used for Fabrication of Diffusion-Bonded Specimens.

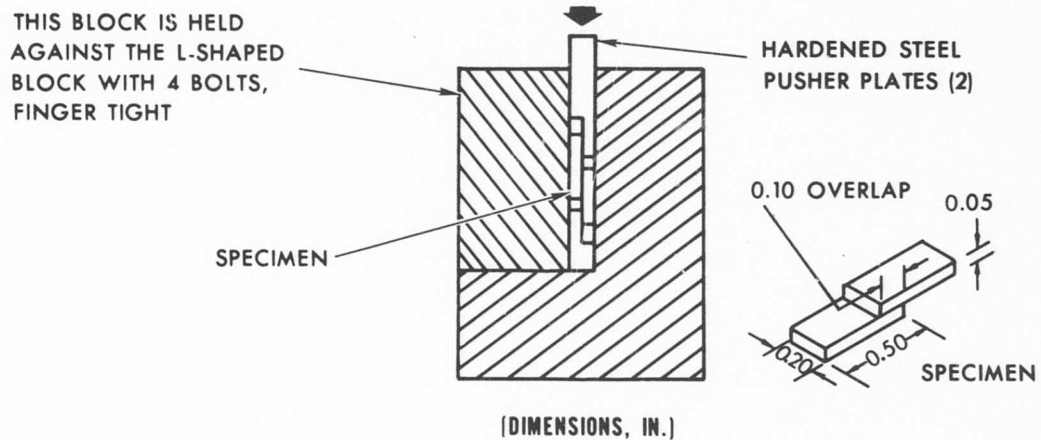
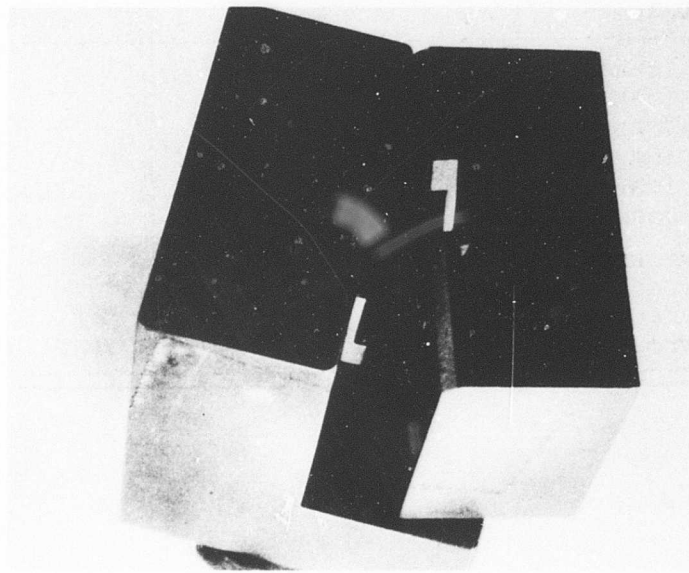


Figure 38. Test Fixture Used to Shear Test Diffusion-Bonded and Cast-Bonded Overlap Specimens.

TABLE XI. MATERIAL COMBINATIONS EVALUATED INITIALLY FOR DIFFUSION-BONDED JOINTS

Candidate Strut Material	Sheet Material (Strut/Shell Bond)	Disk Material (Strut/Disk Bond)
MAR-M 246 (cast)	AiResist 213	
MAR-M 246 (cast)	René 41	
MAR-M 246 (cast)	AF2-1DA	
MAR-M 246 (cast)		AF2-1DA
MAR-M 246 (cast)		Waspaloy
MAR-M 246 (cast)		Inconel 718
AF2-1DA (wrought)	AiResist 213	
AF2-1DA (wrought)	René 41	
AF2-1DA (wrought)	AF2-1DA	
AF2-1DA (wrought)		AF2-1DA

TABLE XII. LAP/SHEAR TESTS OF DIFFUSION-BONDED SPECIMENS

Specimen No.	Material Combination	Interface Material	Bonding Conditions Temp/Time/Pressure	Apparent Shear Stress (psi)	Estimated Actual Shear Stress (psi)
D-1	MAR-M 246/AiR 213	None	1800°F/15 min /11,600 psi	23,800	39,100
D-2				22,300	38,400
D-3				25,400	42,800
D-14	MAR-M 246/AiR 213	None	1800°F/15 min /29,500 psi	53,000	90,000
D-15				26,000	46,800
D-16				51,500	81,900
D-7	MAR-M 246/AiR 213	Ni	1800°F/15 min /11,600 psi	-	-
D-8				48,900	76,700
D-9				40,600	87,800
8-1A	MAR-M 246/AiR 213	Ni + 3% Be (0.001 in.)	1800°F/45 min /11,600 psi	23,300	54,200
8-2A				54,200	39,600
8-3A				19,500	41,000
8-1B	MAR-M 246/AiR 213	Ni + 3% Be (0.001 in.)	1800°F/15 min /29,500 psi	36,900	48,600
8-2B				47,200	50,100
8-3B				47,200	49,200
D-4-1	MAR-M 246/Rene' 41	None	1800°F/15 min /11,600 psi	31,100	68,500
D-4-2				30,600	54,600
D-4-3				16,700	43,500
D-4-10	MAR-M 246/Rene' 41	None	1800°F/15 min /29,500 psi	32,700	63,400
D-4-11				5700	11,100
D-4-12				10,000	16,500
D-4-7	MAR-M 246/Rene' 41	Ni	1800°F/15 min /11,600 psi	16,900	45,400
D-4-8				29,700	54,500
D-4-9				12,500	23,000
4-1	MAR-M 246/Rene' 41	Ni + 3% Be (0.001 in.)	1800°F/45 min /11,600 psi	17,800	22,300
4-2				30,600	31,300
4-3				21,700	24,000
13-1	AF2-1DA/AiR 213	None	1800°F/15 min /29,500 psi	34,200	42,700
13-2				21,300	28,400
13-3				36,700	43,200
14-1	AF2-1DA/AiR 213	None	1800°F/15 min /29,500 psi	46,800	52,100
14-2				53,700	57,200
14-3				62,800	64,100
15-1	AF2-1DA/AiR 213	Ni	1800°F/15 min /11,600 psi	33,100	27,100
15-2				32,100	36,900
15-3				19,200	27,400
16-1	AF2-1DA/AiR 213	Ni + 3% Be (0.001 in.)	1800°F/45 min /11,600 psi	23,500	26,200
16-2				20,200	31,000
16-3				37,100	39,000
9-1	AF2-1DA/Rene' 41	None	1800°F/15 min /11,600 psi	47,030	42,500
9-2				8400	62,600
9-3				37,800	51,500
10-1	AF2-1DA/Rene' 41	None	1800°F/15 min /29,500 psi	67,200	83,800
10-2				90,000	94,800
10-3				66,000	73,700
11-1	AF2-1DA/Rene' 41	Ni	1800°F/15 min /11,600 psi	34,600	40,800
11-2				47,700	53,900
11-3				18,100	27,700
12-1	AF2-1DA/Rene' 41	Ni + 3% Be (0.001 in.)	1800°F/45 min /11,600 psi	20,000	23,600
12-2				35,900	36,100
12-3				41,500	42,300

TABLE XII - Continued

Specimen No.	Material Combination	Interface Material	Bonding Conditions Temp/Time/Pressure	Apparent Shear Stress (psi)	Estimated Actual Shear Stress (psi)
17-1	AF2-1DA/AF2-1DA	None	1800°F/15 min /11,600 psi	36,800	38,900
17-2				25,100	28,900
17-3				30,100	33,500
18-1	AF2-1DA/AF2-1DA	None	1800°F/15 min /29,500 psi	62,600	64,500
18-2				65,000	66,400
18-3				72,200	72,800
19-1	AF2-1DA/AF2-1DA	Ni	1800°F/15 min /11,600 psi	25,400	30,200
19-2				27,200	30,200
19-3				25,600	30,100
20-1	AF2-1DA/AF2-1DA	Ni + 3% Be (0.001 in.)	1800°F/15 min /11,600 psi	42,000	44,400
20-2				31,100	34,600
20-3				46,400	47,700
21-1	AiR 213/Rene 41	Ni + 3% Be (0.001 in.)	1800°F/45 min /29,500 psi	58,300	61,400
21-2				58,000	61,100
21-3				53,000	57,200
1	MAR-M 246/AF2-1DA	None	1800°F/15 min /40,600 psi	67,200	67,200
2				74,500	74,500
3				63,200	63,200
10	MAR-M 246/AF2-1DA	None	1800°F/15 min /29,500 psi	41,600	55,500
11				51,000	59,400
12				36,000	59,400
19	MAR-M 246/AF2-1DA	Ni (0.0005-in.)	1800°F/15 min /29,500 psi	96,800	96,800
20				95,200	95,200
21				91,000	91,000
28	MAR-M 246/AF2-1DA	Ni + 3% Be (0.001-in.)	1800°F/45 min /29,500 psi	88,200	104,000
29				156,000	156,000
30				148,500	148,500
4	MAR-M 246/Waspaloy	None	1800°F/15 min /40,600 psi	74,200	82,500
5				68,200	80,000
6				75,700	84,000
13	MAR-M 246/Waspaloy	None	1800°F/15 min /29,500 psi	72,200	72,200
14				55,000	69,000
15				30,700	51,200
22	MAR-M 246/Waspaloy	Ni (0.0005 in.)	1800°F/15 min /29,500 psi	70,800	70,800
23				67,900	67,900
24				70,200	70,200
31	MAR-M 246/Waspaloy	Ni + 3% Be (0.001-in.)	1800°F/45 min /29,500 psi	74,000	74,000
32				81,000	81,000
33				68,000	68,000
7	MAR-M 246/ Inconel 718	None	1800°F/15 min /40,600 psi	95,600	106,200
8				59,500	91,500
9				95,800	100,500
16	MAR-M 246/ Inconel 718	None	1800°F/15 min /29,500 psi	67,300	75,000
17				103,200	103,200
18				99,000	99,000
25	MAR-M 246/ Inconel 718	Ni (0.0005-in.)	1800°F/15 min /29,500 psi	94,900	94,900
26				93,700	93,700
27				100,000	100,000
34	MAR-M 246/ Inconel 718	Ni + 3% Be (0.001-in.)	1800°F/45 min /29,500 psi	83,800	83,800
35				88,500	88,500
36				81,500	81,500

TABLE XIII. SUMMARY OF SHEAR-TILT RESULTS
ON DIFFUSION-BONDED SPECIMENS

Material Combination	Interface Material	Bonding Conditions Time/Temp/Pressure	Apparent Shear Stress (psi)	Estimated Actual Shear Stress (psi)
AF2-1DA/MAR-M 246	None	15 min/1800°F/40,600 psi	68,300	68,300
AF2-1DA/MAR-M 246	None	15 min/1800°F/29,500 psi	42,866	58,100
AF2-1DA/MAR-M 246	Ni	15 min/1800°F/29,500 psi	94,333	94,333
AF2-1DA/MAR-M 246	Ni + Be sheet	45 min/1800°F/29,500 psi	130,900	136,166
Waspaloy/MAR-M 246	None	15 min/1800°F/40,600 psi	72,700	82,166
Waspaloy/MAR-M 246	None	15 min/1800°C/29,500 psi	52,633	64,133
Waspaloy/MAR-M 246	Ni	15 min/1800°F/29,500 psi	69,633	69,633
Waspaloy/MAR-M 246	Ni + Be sheet	45 min/1800°F/29,500 psi	74,333	74,333
Inconel 718/ MAR-M 246	None	15 min/1800°F/40,600 psi	83,633	99,400
Inconel 718/ MAR-M 246	None	15 min/1800°F/29,500 psi	89,833	92,400
Inconel 718/ MAR-M 246	Ni	15 min/1800°F/29,500 psi	96,200	96,200
Inconel 718/ MAR-M 246	Ni + Be sheet	45 min/1800°F/29,500 psi	84,600	84,600

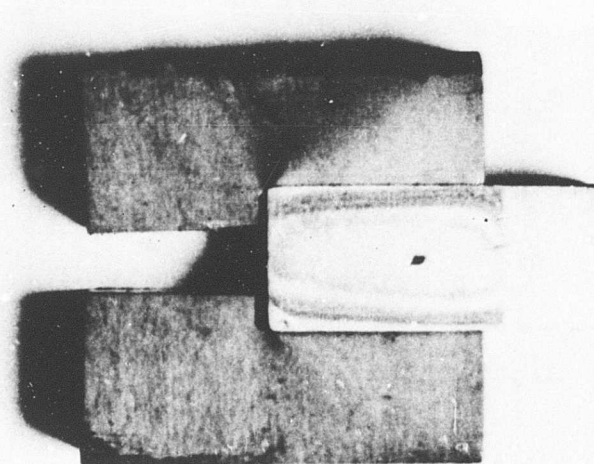


Figure 39. Diffusion-Bonding Specimen
(Final Test Size).

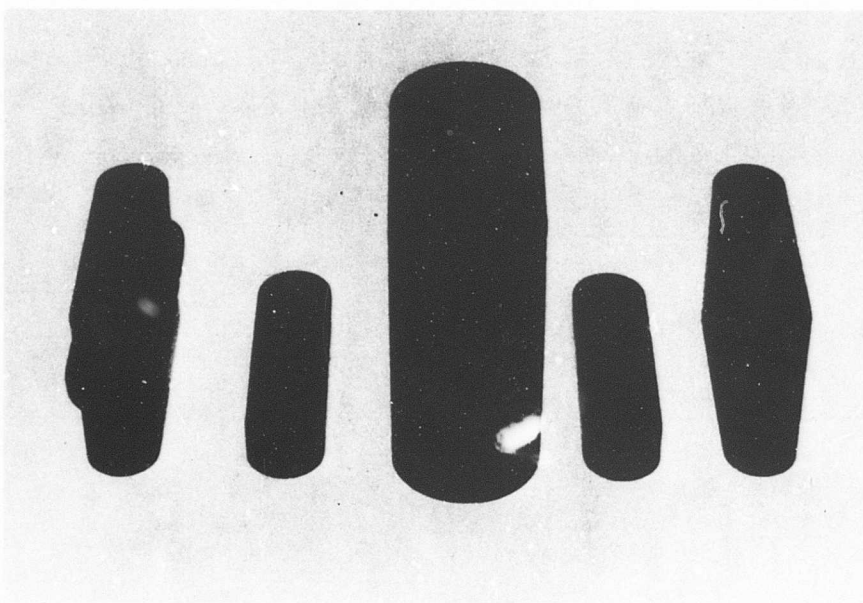


Figure 40. Die Used for Diffusion Bonding of Figure 39 Specimen.

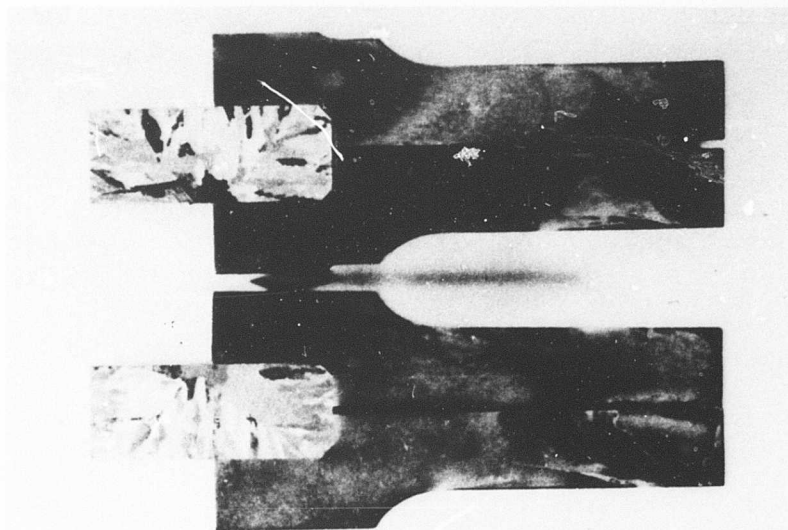


Figure 41. Diffusion-Bonded Specimens Simulating the Final Test Design.

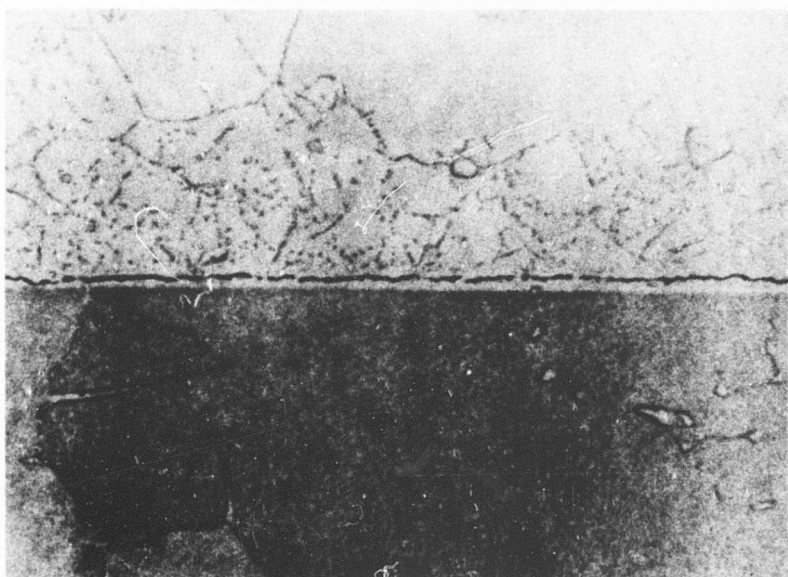


Figure 42. Typical Diffusion-Bonded Joint Produced With Parameters Selected for Final Test Specimens.

4.2.2 Brazing

Brazing was considered as a joining technique for both the strut/disk and the strut/shell joints. Primary consideration, however, was given to the strut/disk joint, since this region of the rotor can be designed such that temperatures and stresses are sufficiently low to permit reasonably high values for the stress-rupture life of the brazing alloy. Materials that were evaluated included AF2-1DA, Waspaloy, and Inconel 718 as disk materials, MAR-M 246 as strut material, and René 41 and AiResist 213 as shell materials.

4.2.2.1 Experimental Procedure

Three candidate brazing alloys were selected for evaluation: Nicrobraz 30, Nicrobraz 150, and Palniro 49TX. Compositions for each of these alloys are given in Table XIV. Selection of these alloys were based upon reported high-temperature stress-rupture properties.

Test specimens as shown in Figure 43 were prepared for preliminary testing. Specimens were machined from 0.050-inch thick sheet material, and the overlap surfaces were nickel-plated to a thickness of 0.0002 to 0.0005 inch. The specimens were positioned and tack-welded in the fixture shown in Figure 44. In each case, the braze gap clearance was controlled by shimming (to 0.002 inch) prior to tack welding. Both of the Nicrobraz alloys were placed in powder form in an amount to fill the gap adequately during the brazing operation. The Palniro 49TX alloy was preplaced in foil form (0.002-inch-thick) prior to tack welding.

Brazing was performed in a vacuum furnace at a vacuum of 0.5 micron and with a cycle of $2150^{\circ} \pm 10^{\circ}\text{F}$ for 20 minutes. Final machining of the specimens, as shown in Figure 45, removed the tack weld. All testing was by stress-rupture, since this is, in general, the limiting strength property of a brazed joint.

4.2.2.2 Test Results and Conclusions

Stress-rupture test results are listed in Table XV. Data for the strut/disk material combinations of Waspaloy to MAR-M 246 and Inconel 718 to MAR-M 246 indicated that the Nicrobraz 150 brazing alloy potentially offers the greatest stress-rupture strength. However, this alloy was eliminated from further consideration because of excessive erosion (base-metal attack) as indicated by Figure 46.

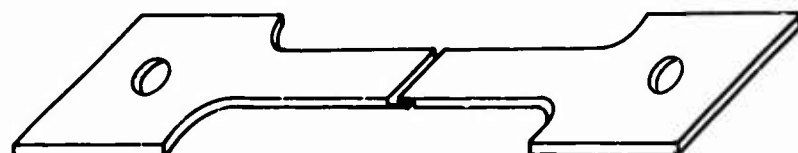
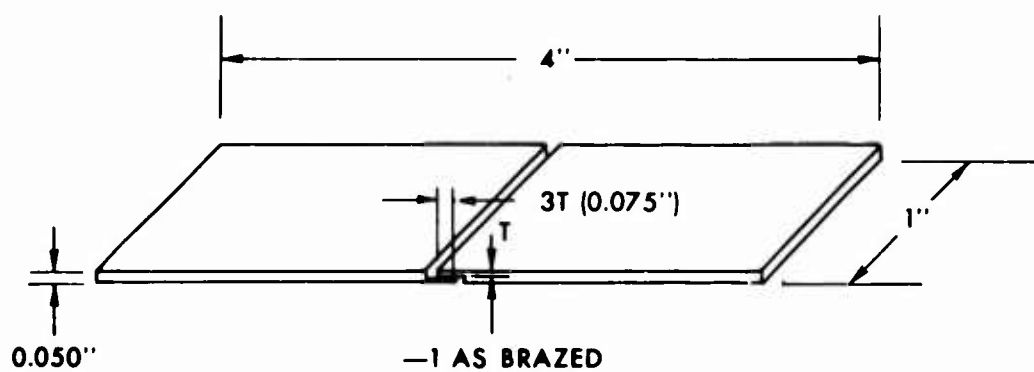
In most cases, the Nicrobraz 150 specimens failed through the bare metal at the brazing fillet area rather than through the brazing material. An example of such a failure is shown in Figure 46. Most of the specimens on which testing was terminated after approximately 100 hours failed at the fillet area upon removal from the testing fixtures. This indicated the extent of the embrittling effect of the braze. Examples of typical failed joints for specimens brazed with Nicrobraz 30 and Palniro 49TX are shown in Figures 47 and 48, respectively. In both of these cases, the small amount of erosion and the failure through the brazing material are evident.

The Palniro 49TX alloy behaved quite well during brazing and produced a sound joint. However, the stress-rupture strength of this alloy was somewhat less than for Nicrobraz 30 at the higher temperatures. As a result, Nicrobraz 30 alloy was selected for use in the final test specimens.

Figure 49 shows stress-rupture data for Nicrobraz 30 joints with the two material combinations of Waspaloy/MAR-M 246 and Inconel 718/ MAR-M 246. The combination of Waspaloy with MAR-M 246 gave the better stress-rupture properties. Specimens from which these data were obtained were given a post-braze heat treatment to correspond to the required treatment for either Inconel 718 or Waspaloy, as applicable. Examination of failed specimens indicated that the Inconel 718/MAR-M 246 specimens had a tendency to shear at the interface between the braze and the Inconel 718 rather than through the braze. For these reasons, the Waspaloy/MAR-M 246 combination was selected for further testing.

TABLE XIV. NOMINAL COMPOSITIONS OF THE BRAZING ALLOYS SELECTED FOR EVALUATION

Material	NOMINAL COMPOSITION							
	Cr	Si	C	Ni	B	Ta	Pd	Au
Nicrobraz 30	19.0	10.0	0.10	Bal	-	-	-	-
Nicrobraz 150	15.0	-	0.10	Bal	3.5	-	-	-
Palniro 49TX	9.0	-		29.0		1.0	27.5	33.5



—2 READY FOR TEST

BRAZE TEST SPECIMEN

Figure 43. Braze Test Specimen.

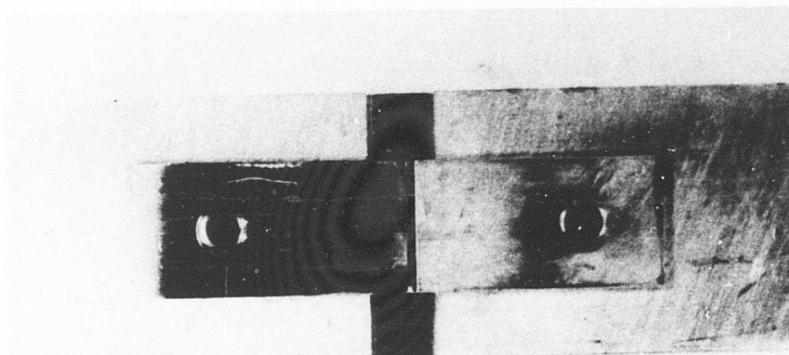


Figure 44. Fixture Used During Tack Welding of the Brazing Specimens.

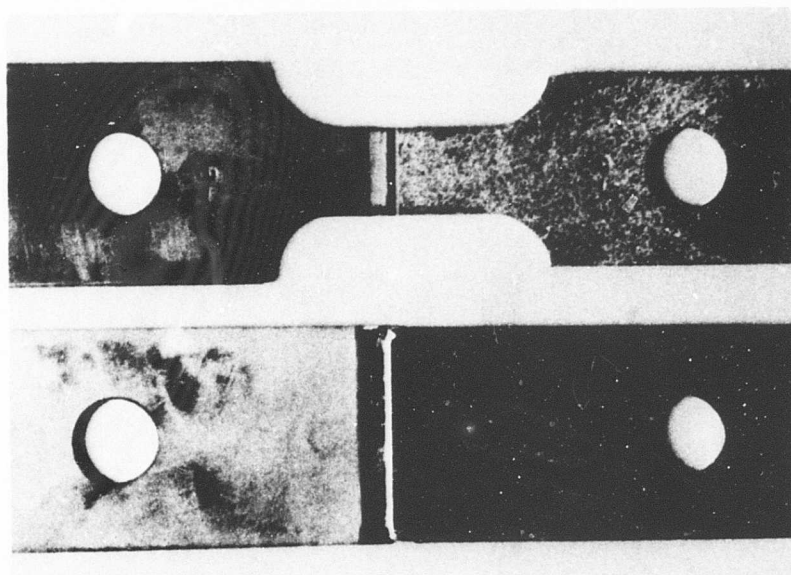


Figure 45. Brazing Specimens Before (Top) and After (Bottom) Final Machining.

TABLE XV. STRESS-RUPTURE DATA
 ON BRAZING SPECIMENS

Specimen No.	Material Combination	Braze Alloy	Temp (°F)	Stress (psi)	Time (Hours)	Fracture Location	Comments	Specimen Heat Treatment
1-0	AF2-1DA/ AF2-1DA	Nicrobraz 30	1200	10,000	100.0	No fracture	Test discontinued	None
1-1			1200	20,000	0.2	Through braze		
1-2			1200	15,000	1.2	Same as above		
1-3			1400	8000	1.6	Same as above		
1-4			1400	5000	40.7	Same as above		
1-5			1400	6500	13.1	Same as above		
2-0	MAR-M 246/ AIR 213	Nicrobraz 30	1200	30,000	-	Through MAR-M 246	Broke on loading	None
2-1			1200	15,000	-	Through braze	Broke on loading	
2-2			1200	7500	100.0	No fracture	Test discontinued	
2-3			1400	20,000	-	Through braze	Broke on loading	
2-4			1400	10,000	0.5	Through braze	Broke on loading	
2-5			1400	7500	-	Through braze		
3-0	AF2-1DA/ AiR 213	Nicrobraz 30	1200	10,000	14.0	Through AF2-1DA	Test discontinued	None
3-1			1200	8000	100.0	No fracture	Test discontinued	
3-2			1200	9000	100.0	No fracture		
3-3			1400	9000	0.7	Through braze		
3-4			1400	5000	4.6	Through braze		
3-5			1400	2500	100.0	No fracture	Test discontinued	
4-1	MAR-M 246/ INCO 718	Palniro 49TX	1200	11,000	19.0	Through braze		Inconel 718 age
4-2			1200	10,000	23.1	Through braze		
4-3			1200	9000	36.5	Through braze		
4-4			1400	9500	0.3	Through braze		
4-5			1400	8000	0.7	Through braze		
5-1	MAR-M 246/ INCO 718	Nicrobraz 30	1200	10,000	19.1	Through braze	Test discontinued	None
5-2			1200	9000	20.8	Through braze		
5-3			1200	6000	101.0	No fracture		
5-4			1400	10,000	2.3	Through braze		
5-5			1400	8000	3.9	Through braze		
6-1	MAR-M 246/ INCO 718	Nicrobraz 150	1200	8000	100.3	Braze fillet	Broke on removal	None
6-2			1200	10,000	114.0	Braze fillet	Broke on removal	
6-3			1200	20,000	122.1	Braze fillet	Test discontinued	Inconel 718 age
6-4			1400	9000	114.0	No fracture		
6-5			1400	12,000	13.3	Braze fillet		
7-1	AF2-1DA/ René 41	Palniro 49TX	1200	12,000	5.2	Through braze		None
7-2			1200	10,000	14.3	Through braze		
7-3			1200	8000	33.3	Through braze		
7-4			1400	10,000	-	Overtemp		
7-5			1400	9000	1.4	Through braze		
7-6			1400	6000	6.4	Through braze		
8-1	René 41/ AF2-1DA	Nicrobraz 30	1200	8000	100.0	No fracture	Test discontinued	None
8-2			1200	20,000	-	Through braze	Broke on loading	
8-3			1200	12,000	84.7	Through braze	Broke on loading	
8-4			1400	8000	-	Through braze	Broke on loading	
8-5			1400	15,000	-	Through braze	Broke in machining	
8-6				-	-	Through braze		
9-1	René 41/ MAR-M 246	Nicrobraz 30	1200	12,000	114.0	No fracture	Test discontinued	None
9-2			1200	15,000	109.0	No fracture	Test discontinued	
9-3			1200	10,000	7.4	Through braze		
9-4			1400	8000	30.6	Through braze		
9-5				-	-	Through braze		
9-6				-	-	Through braze		
10-1	René 41/ MAR-M 246	Nicrobraz 150	1200	13,000	108.8	Through braze		None
10-2			1200	16,000	42.0	Braze fillet		
10-3			1400	11,000	15.8	Through braze		
10-4			-	-	-	Through braze		
10-5			-	-	-	Through braze		
10-6			-	-	-	Through braze		
11-1	Waspaloy/ MAR-M 246	Nicrobraz 30	1200	15,000	111.0	No fracture	Test discontinued	Waspaloy age
11-2			1200	20,000	0.8	Braze fillet		
11-3			1200	17,500	0.2	Braze fillet		
11-4			1400	7000	92.4	Through braze		
11-5			1400	12,000	2.1	Through braze		

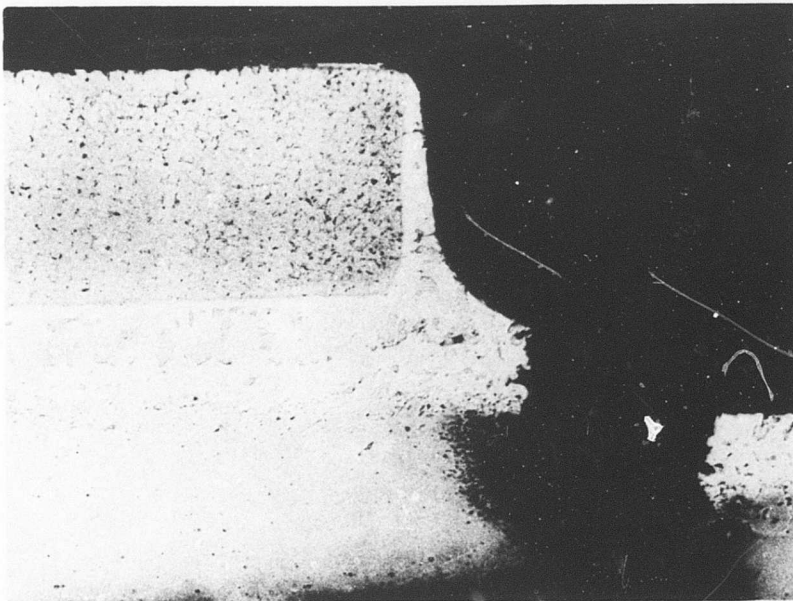


Figure 46. Typical Failed Joint Between Inconel 718 and MAR-M 246 with Nicrobraze 150 Brazing Alloy (x50).

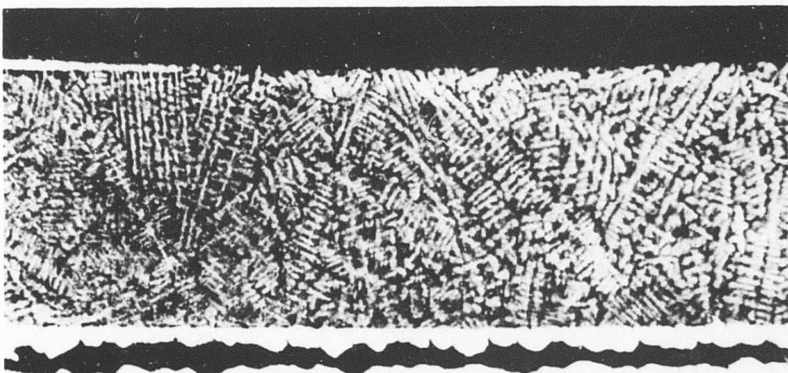


Figure 47. Typical Failed Joint Between Inconel 718 and MAR-M 246 With Nicrobraze 30 Brazing Alloy (x50).

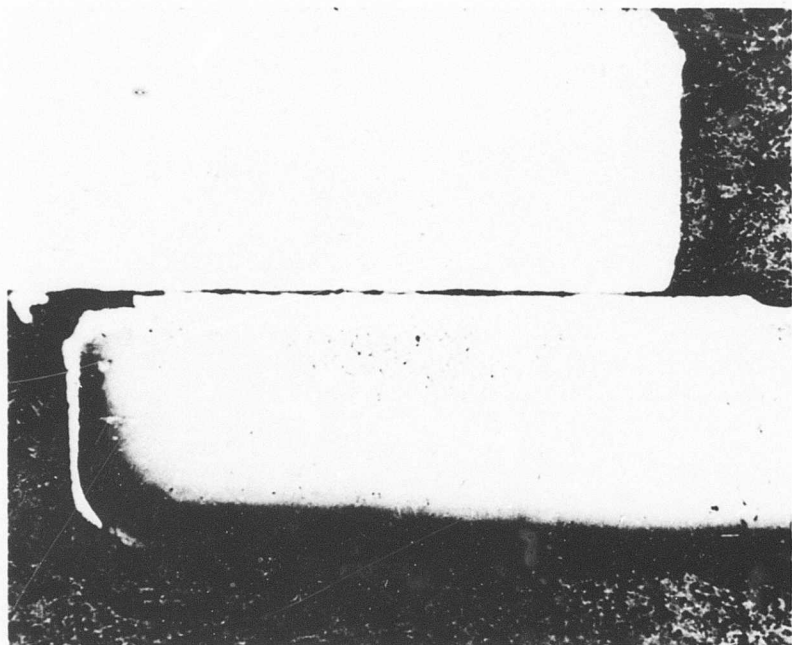


Figure 48. Typical Failed Joint Between Inconel 718 and MAR-M 246 With Palniro 49TX Braze Alloy (X50).

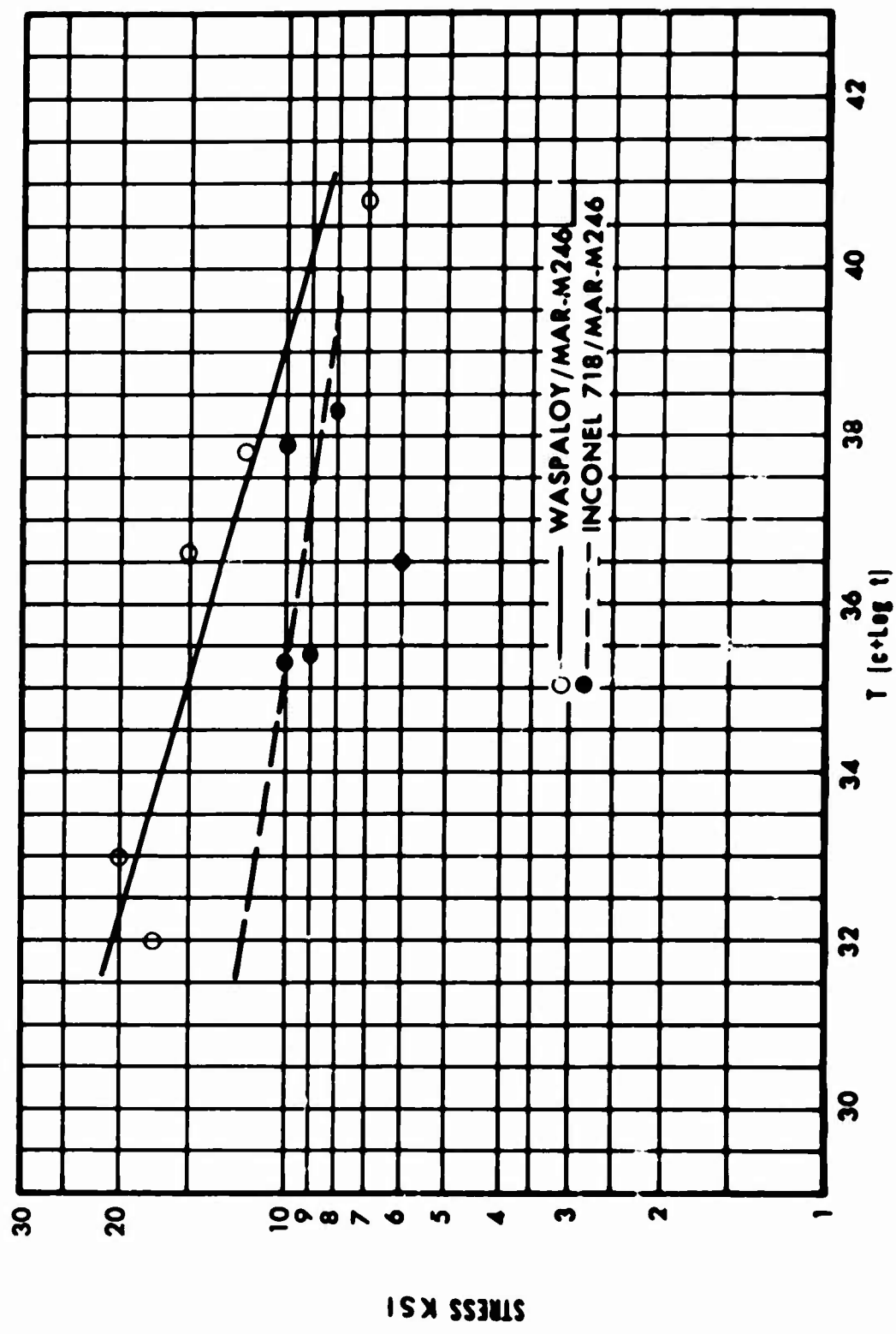


Figure 49. Stress-Rupture Data for
Nicrobraz 30 Brazed Joints.

4.2.3 Electron-Beam Welding

Electron-beam welding was considered for the strut/disk joint. Preliminary evaluations and testing were performed to establish materials and welding parameters required to optimize the weld joint. Materials given initial consideration included MAR-M 246 and AF2-1DA as strut materials and Waspaloy, Inconel 718, and AF2-1DA as disk materials.

4.2.3.1 Experimental Procedure

Preliminary weld evaluations were performed on the specimens shown in Figures 50 and 51. These specimens were prepared by butt welding two pieces of 0.050-inch-thick dissimilar sheet material together and subsequently machining to form a tensile specimen. The MAR-M 246 specimens were selected from cast-to-size flats and were welded in the as-cast condition and also in the 2000°F/2-hour heat-treated condition. For the remainder of the alloys, specimens were cut from sheet material and were welded in the solutioned condition. Post-weld heat treatments were given the specimens to simulate the required heat treatments for the age-hardenable materials.

Evaluation of the strip specimens was by metallographic examination and by tensile testing. Results indicate the material combinations that offered the greatest promise for further testing. These combinations were further evaluated by welding together blocks which simulated the thickness required for the final strut/disk weld joint. Welding parameters were varied and specimens examined to determine the parameters to be used for the final test specimens.

4.2.3.2 Test Results and Conclusions

Examination of the preliminary weld specimens (Figure 52) indicated a tendency toward weld cracking, which is confirmed in Figure 53, in combinations including the alloy AF2-1DA. Variations made in welding parameters in an attempt to eliminate this cracking were successful only in reducing the extent of cracking. Because of this problem, AF2-1DA was eliminated from further consideration. This left two possible material combinations: MAR-M 246/Waspaloy and MAR-M 246/Inconel 718.

Results of tensile tests are given in Table XVI. A summary of results is given in Table XVII and indicates that tensile failures occurred in the cast material (MAR-M 246) in all cases after the specimens were given a post-weld heat treatment to develop full properties in the heat-treatable material. Limiting properties, therefore, were those of the MAR-M 246 material.

The welding procedure was then scaled up to specimen sizes simulating the sizes required for the final test specimens. Welding was performed on blocks of the two material combinations MAR-M 246/Inconel 718 and MAR-M 246/Waspaloy. A total weld penetration distance of 0.790 inch was required. Two methods of achieving this penetration were investigated. The first consisted of welding from each side of the specimen with weld settings such that the two weld spikes would merge. Problems were encountered with use of this technique in that misalignment of weld spikes occurred, as shown in Figure 54. Also, in some cases, voids were formed in weld overlap areas, as shown in Figure 55. The weld spike appearing in the figures on one side of the joint was included prior to the joining weld to simulate the initial welding required to join the disk halves together. Because of the problems with the double-spike joint, a single-pass joint was developed as shown in Figure 56. Some cracking was encountered with this technique, as shown in Figure 57. By adjustment of welding parameters, this cracking was minimized and appeared to be less severe when joining Waspaloy to MAR-M 246 than when joining Inconel 718 to MAR-M 246. In addition, a preweld stabilization treatment of the MAR-M 246 consisting of 2000°F for 2 hours was found to reduce the cracking tendencies.

As a result of the development efforts outlined above, the material combination selected for final testing was MAR-M 246 to Waspaloy. The electron-beam-welding parameters selected for fabrication of the final test specimens are detailed in Section 5.2.3.

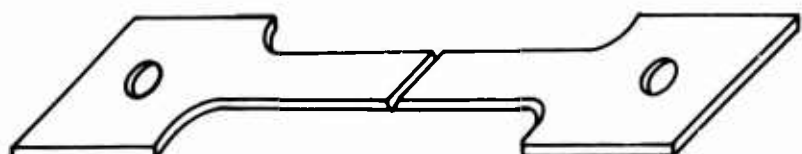
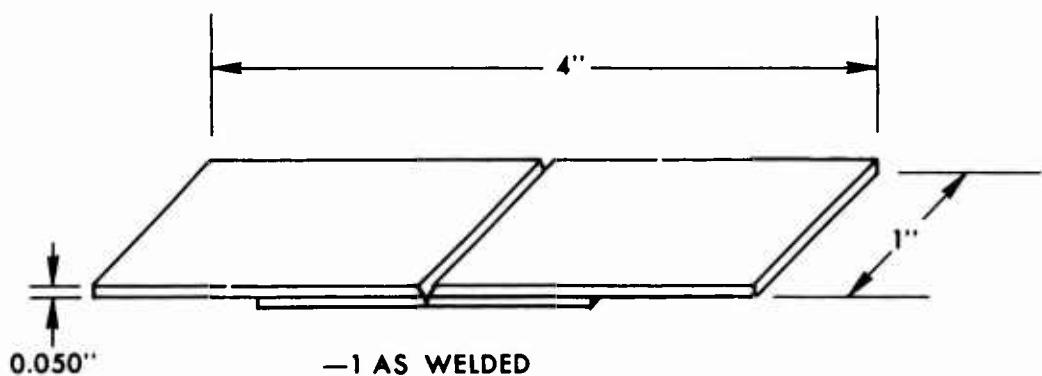


Figure 50. Electron-Beam-Welding Test Specimens.

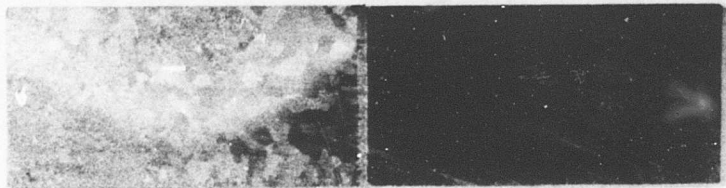


Figure 51. Electron-Beam-Welding Specimen
After Welding and After Final
Machining.

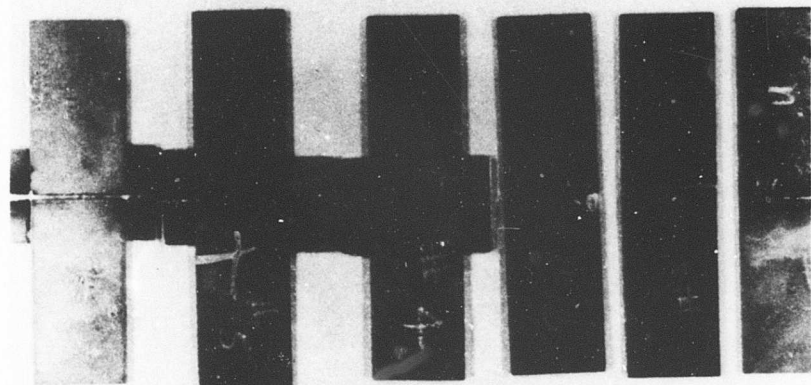


Figure 52. Preliminary Electron-Beam-
Welding Specimens (Half-
Size).

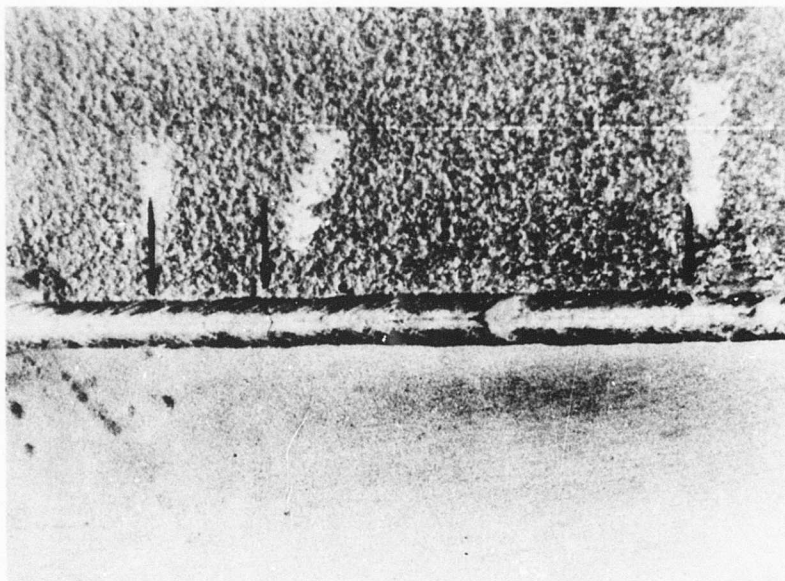


Figure 53. Typical Cracks in Electron-Beam
Welds Joining AF2-1DA to
MAR-M 246 (X10).

TABLE XVI. TENSILE TEST RESULTS OF
ELECTRON-BEAM-WELDED SPECIMENS

Specimen No.	Specimen Description	Heat-Treatment After Welding	Test Temp. (°F)	Yield (psi)	Ult (psi)	Elong (%)	Section Fractured
35	Inconel 718 MAR-M 246	H.T. 5071	Room	123,100	133,100	2.5 ^(a)	MAR-M 246
36	Inconel 718 Mar-M 246	H.T. 5071	Room	130,800	133,500	④	MAR-M 246
37	Inconel 718 MAR-M 246	H.T. 5071	Room	129,000	133,100	3.0	MAR-M 246
38	Inconel 718 MAR-M 246	H.T. 5071	Room	58,000	58,600	④	MAR-M 246
31	Inconel 718 Mar-M 246	H.T. 5071	1200	130,500	144,700	3.0	MAR-M 246
32	Inconel 718 MAR-M 246	H.T. 5071	1200	125,500	144,300	3.0	MAR-M 246
33	Inconel 718 MAR-M 246	H.T. 5071	1200	131,000	143,000	4.5	MAR-M 246
34	Inconel 718 MAR-M 246	H.T. 5071	1200	132,000	149,000	4.5	MAR-M 246
40	Waspaloy MAR-M 246	AMS5544	Room	128,000	129,500	0.5	MAR-M 246
41	Waspaloy MAR-M 246	AMS5544	Room	135,000	140,000	**	MAR-M 246
42	Waspaloy MAR-M 246	AMS5544	Room	161,000	162,000	1.0	MAR-M 246
39	Waspaloy MAR-M 246	AMS5544	Room	54,200	64,000	1.0	MAR-M 246
6	Waspaloy MAR-M 246	None	Room	64,000	120,100	41	Waspaloy
7	Waspaloy MAR-M 246	None	Room	68,400	123,400	37	Waspaloy
8	Waspaloy MAR-M 246	None	Room	66,500	125,000	43	Waspaloy
43	Waspaloy MAR-M 246	AMS5544	1200	125,000	169,000	3.5	MAR-M 246
44	Waspaloy MAR-M 246	AMS5544	1200	137,200	163,200	4.5	MAR-M 246
45	Waspaloy MAR-M 246	AMS5544	1200	126,000	156,200	2.0	MAR-M 246
46	Waspaloy MAR-M 246	AMS5544	1200	109,900	138,200	2.5	MAR-M 246
3	Waspaloy MAR-M 246	None	1200	58,400	104,100	31	Waspaloy
4	Waspaloy MAR-M 246	None	1200	58,000	101,500	36	Waspaloy
5	Waspaloy MAR-M 246	None	1200	57,400	100,000	34	Waspaloy
14	Waspaloy AF2-1DA	None	Room	70,400	123,400	43	Waspaloy
15	Waspaloy AF2-1DA	None	Room	68,400	119,600	42	Waspaloy

TABLE XVI - Continued

Specimen No.	Specimen Description	Heat-Treatment After Welding	Test Temp (°F)	Yield (psi)	Ult (psi)	Elong (%)	Section Fractured
16	Waspaloy/AF2-1DA	None	Room	66,500	109,500	12	Weld
11	Waspaloy/AF2-1DA	None	1200	62,500	101,800	30	Waspaloy
12	Waspaloy/AF2-1DA	None	1200	55,300	103,000	28	Waspaloy
13	Waspaloy/AF2-1DA	None	1200	58,400	102,000	36	Weld Waspaloy
21	AF2-1DA/MAR-M 246	None	Room	105,600	135,500	4	MAR-M 246
27	AF2-1DA/MAR-M 246	None	Room	105,000	138,200	4	MAR-M 246
29	AF2-1DA/MAR-M 246	None	Room	127,000	128,500	②	MAR-M 246
30	AF2-1DA/MAR-M 246	None	Room	②	136,400	55	MAR-M 246
25	AF2-1DA/MAR-M 246	None	1200	111,000	126,000	7	MAR-M 246
26	AF2-1DA/MAR-M 246	None	1200	114,000	137,000	3	Weld
28	AF2-1DA/MAR-M 246	None	1200	95,200	105,600	3	Weld
17	AF2-1DA/AF2-1DA	None	Room	96,000	168,000	18②	AF2-1DA
18	AF2-1DA/AF2-1DA	None	Room	99,000	162,800	14②	AF2-1DA
19	AF2-1DA/AF2-1DA	None	Room	92,800	162,000	13②	AF2-1DA
20	AF2-1DA/AF2-1DA	None	1200	109,000	140,000	10	AF2-1DA
22	AF2-1DA/AF2-1DA	None	1200	106,000	138,000	8	AF2-1DA

② Heat Treatments

H.T. 5071 - (Inconel 718 aging treatment)
 1300°F/8 hours to 1150°F in 2 hours and
 hold for 8 hours at 1150°F.

AMSS544 - (Waspaloy aging treatment)
 1550°F/4 hours; 1400°F/16 hours.

④ Broke in punch marks

⑤ Broke outside gauge length

⑥ Unavailable

TABLE XVII. SUMMARY OF TENSILE-TEST
RESULTS ON ELECTRON-BEAM-
WELDED SPECIMENS

Material Combination	Post-Weld Heat Treatment	Test Temp (°F)	Mean Yield Strength (psi)	Mean Ultimate Strength (psi)	Mean Elongation (%)	Section Fractured
Inconel 718/ MAR-M 246	H.T. 5071	Room	127,633	133,233	2.8	MAR-M 246
Inconel 718/ MAR-M 246	H.T. 5071	1200	129,750	145,250	3.8	MAR-M 246
Waspaloy/ MAR-M 246	AMS 5544	Room	141,33	143,833	0.8	MAR-M 246
Waspaloy/ MAR-M 246	AMS 5544	1200	124,525	156,650	3.1	MAR-M 246
Waspaloy/ MAR-M 246	None	Room	66,300	122,833	40.0	Waspaloy
Waspaloy/ MAR-M 246	None	1200	57,933	101,866	33.7	Waspaloy

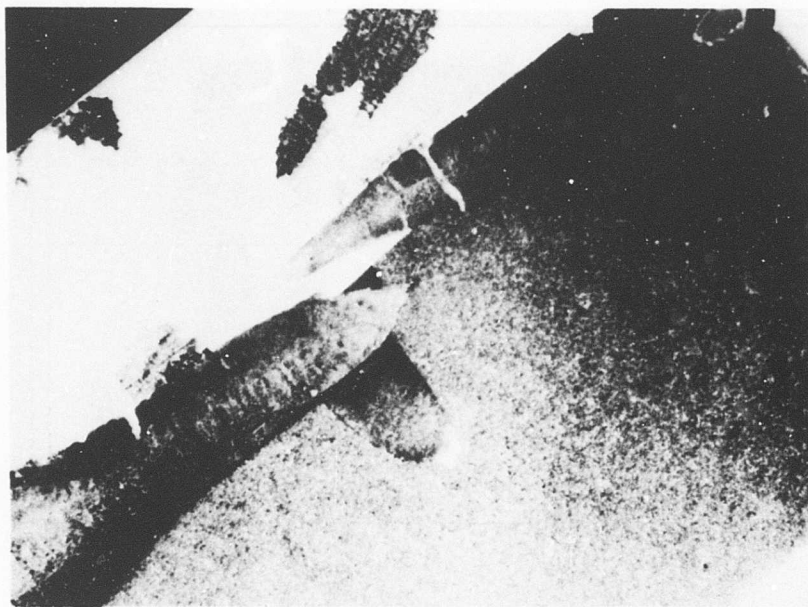


Figure 54. Electron-Beam-Welded Joint Produced by Welding From Both Sides. (Total Thickness is 0.790 Inch. Note the Mismatch of the Two Weld Spikes.)

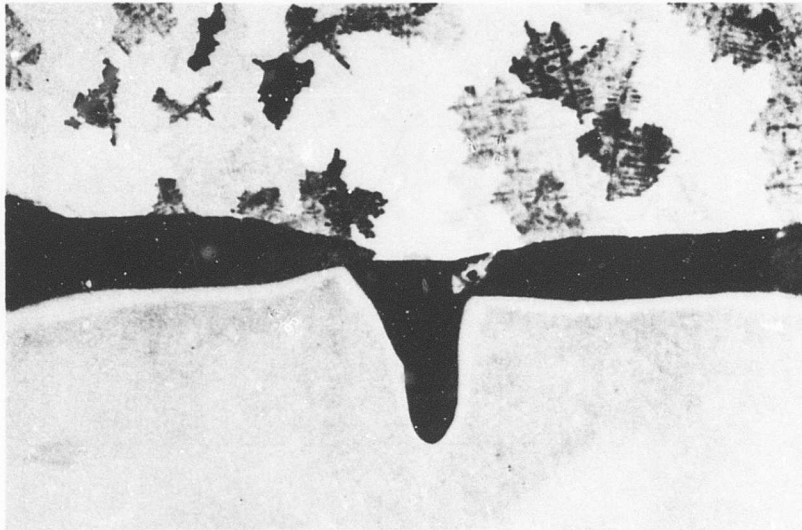


Figure 55. Electron-Beam-Welded Joint Produced by Welding From Both Sides. (Total Thickness is 0.790 Inch. Note the Void at the Weld Overlap Area.)

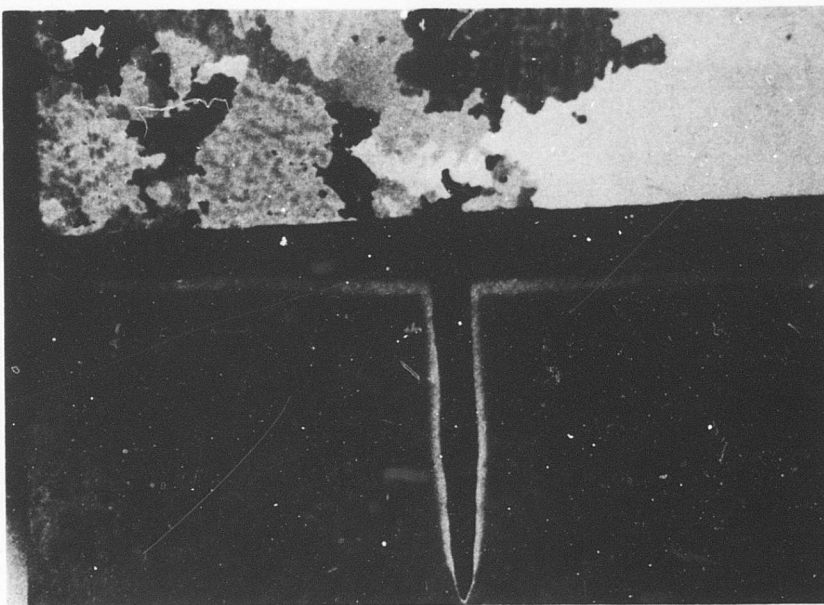


Figure 56. Single-Pass Electron-Beam-Welded Joint Developed for the Final Weld Specimens (X5).

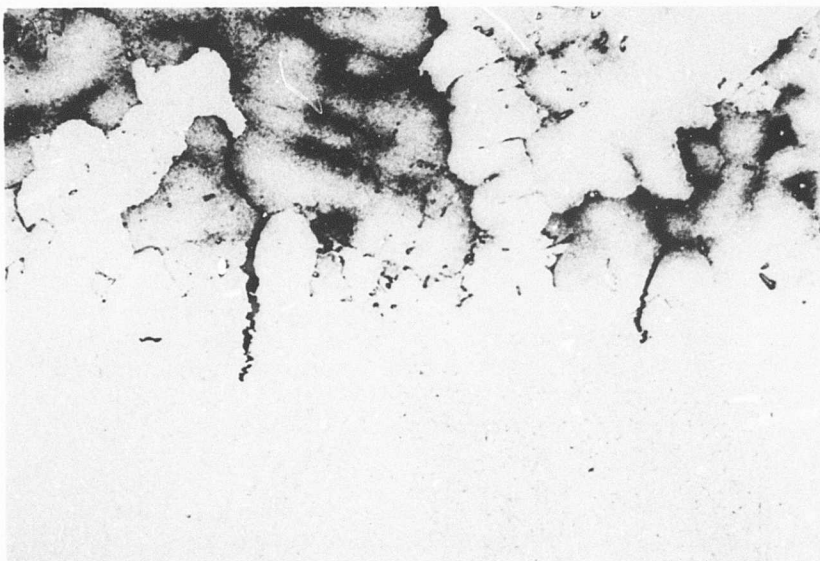


Figure 57. Example of the Minimum Amount of Cracking Achieved in Specimens Simulating Final Test Specimens. The Material Combination is MAR-M 246/Waspaloy (X100).

4.2.4 Cast Bonding

The technique of casting one material against a second material to form a metallurgical bond was evaluated as a candidate means for strut/shell joining. The intent in this case was to form the blade from sheet material, place the blade into a die, preheat, and cast the molten strut material into the sheet metal blade. In this manner the strut would be cast and joined to the shell in the same operation. In the final design, cooling-air passages could be formed by preplacing refractory-metal wires against the shell prior to casting of the strut. Once the casting was complete, the wires could be oxidized out, leaving passages in the cast material through which cooling air could be channeled.

4.2.4.1 Experimental Procedure

To evaluate this technique, a die was designed in which one material could be cast against a second material to form an overlap joint which, in turn, could be tested for shear strength. An example of the die and final specimen is shown in Figure 58. The bonding procedure consisted of placing a piece of sheet material into the die and casting the second material against it. Parameters considered were melt pouring temperature, die preheat temperature, sheet specimen surface finish, and casting atmosphere. After the initial investigation to evaluate the potential for forming a bond, molybdenum wires were preplaced on the sheet specimen, as shown in Figure 59. These wires were successfully oxidized out to form simulated cooling-air passages.

Melting and casting were performed in the vacuum induction furnace shown in Figure 60. The furnace contained two independent induction coils--one to heat the crucible for melting of the charge and one to heat the mold so that the sheet metal could be preheated. Casting procedure consisted of evacuating the furnace to a vacuum of 10^{-4} microns and then backfilling with argon to a pressure of 10 psia. During the evacuating operation the mold and crucible were heated slowly to allow outgassing. Once backfilling was complete, the melted and preplaced sheet metal were brought to the desired temperatures, as indicated by optical measurements. The molten metal was then cast against the sheet and allowed to furnace-cool in the argon atmosphere.

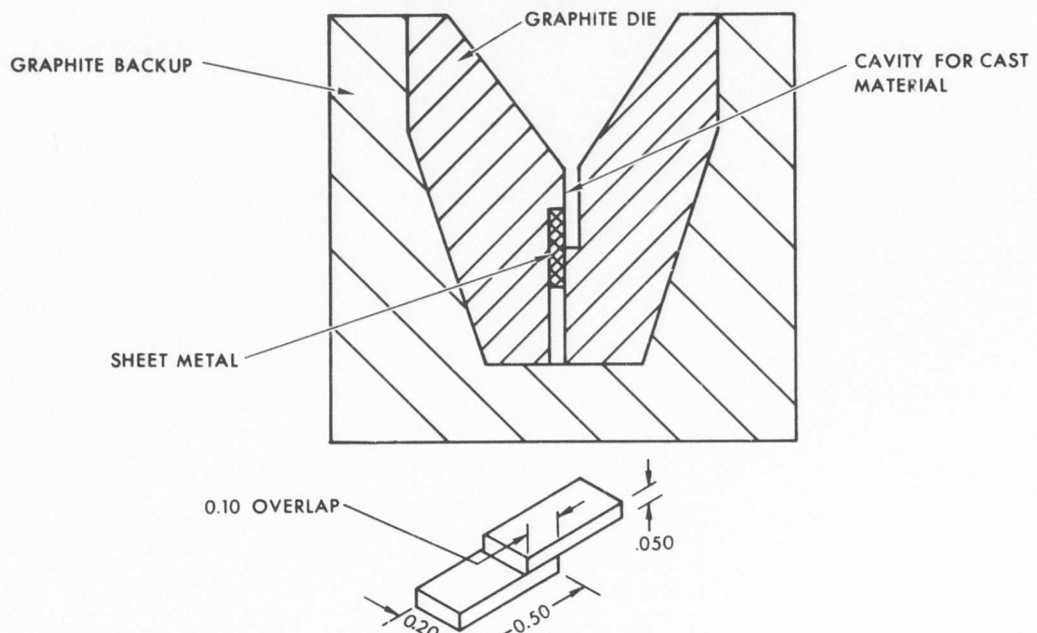
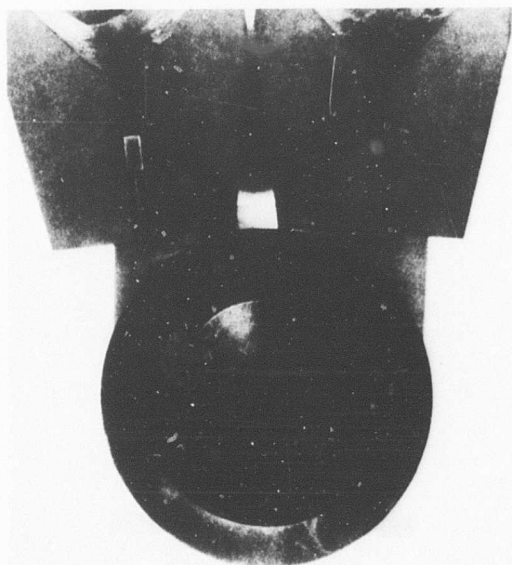
Shear strengths of the bonds were evaluated by use of the test apparatus that was used for the diffusion bonding shear test of Section 4.2.1.1, (see Figure 38). This device held the overlap specimen in such a manner that the shear strength could be determined by using a Riehle tensile testing machine to apply a shear load to the specimen.

Once the fabrication parameters and test data were determined, a series of specimens was prepared with preplaced molybdenum wires (0.040 inch in diameter) on the sheet material. After casting, the wires were removed by alternate exposures to an oxidizing atmosphere (1500°F) and to a potassium hydroxide solution, which left simulated cooling-air passages. These specimens were subsequently shear tested.

4.2.4.2 Test Results and Conclusions

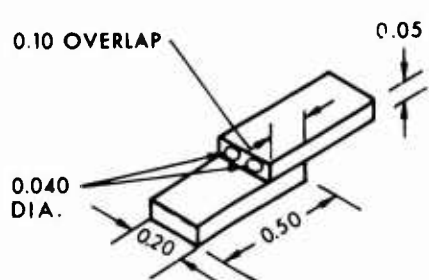
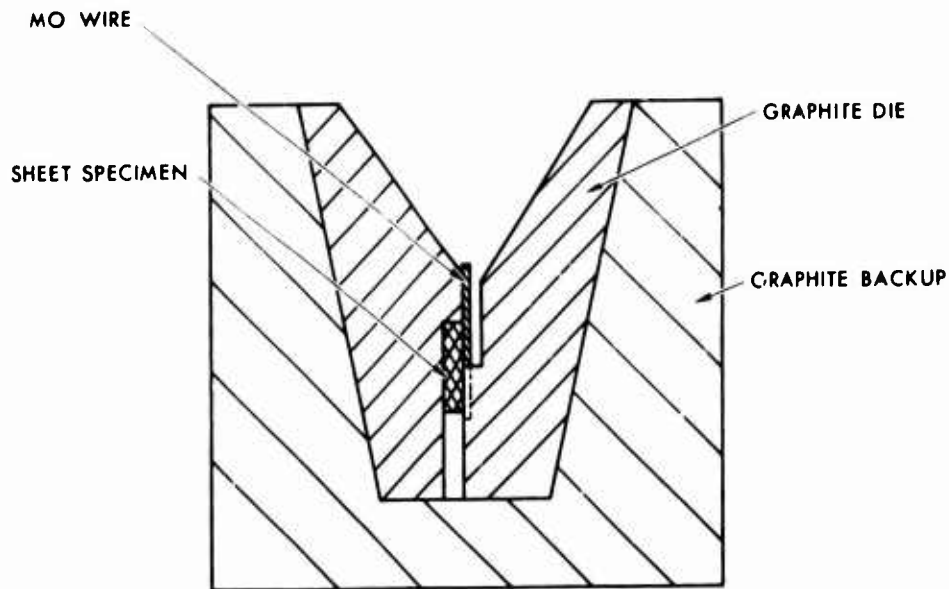
Initial attempts to form a cast bond consisted of casting MAR-M 246 against AiResist 213 with use of a melt temperature of 2650°F and a die temperature (temperature of the AiResist 213 sheet) of 1200°F. The sheet specimen was prepared by polishing through 600-grit followed by a cleaning operation. These parameters produced only a superficial bond. A series of specimens was then prepared with use of a melt temperature of 2750°F and a mold temperature of 1650°F. Although a good bond was produced under these conditions, metallographic examination indicated some cracking in the cast material, as shown in Figure 61. An increase in mold temperature to 2000°F resulted in good bonds; thus, the final bonding parameters selected were a 2750°F melt temperature and a 2000°F mold temperature. Two examples of joints produced under these conditions are shown in Figure 62. The apparent differences in the joints indicate the amount of variability possible from joint to joint.

Results of shear testing are summarized in Table XVIII. Although good shear strengths were achieved in some cases, the large variation in strengths indicates some lack of reproducibility. However, the feasibility of this technique was demonstrated. Additional development effort could well prove it to be an effective method of forming intricate cooling passages in a cooled blade. However, the evaluation was terminated at this point since the principal attachment effort was directed toward the strut/disk joint rather than the sheet metal shell/strut joint.



(DIMENSIONS, IN.)

Figure 58. Die Arrangement for Forming Cast-Bonding Test Specimens.



(DIMENSIONS, IN.)

Figure 59. Die Arrangement and Specimen Produced by Cast Bonding With Preplaced Molybdenum Wires.

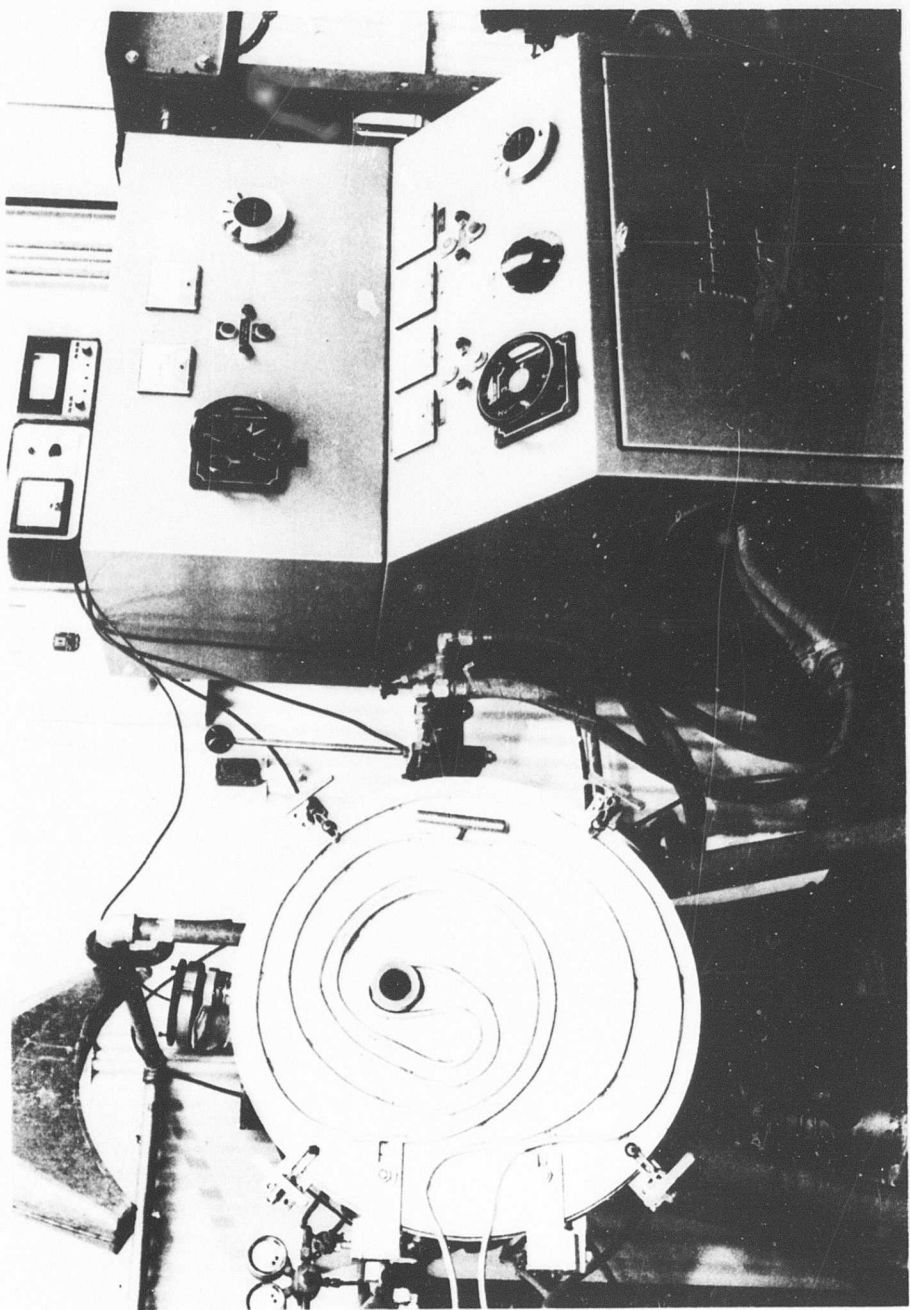


Figure 60. Vacuum Induction Furnace.

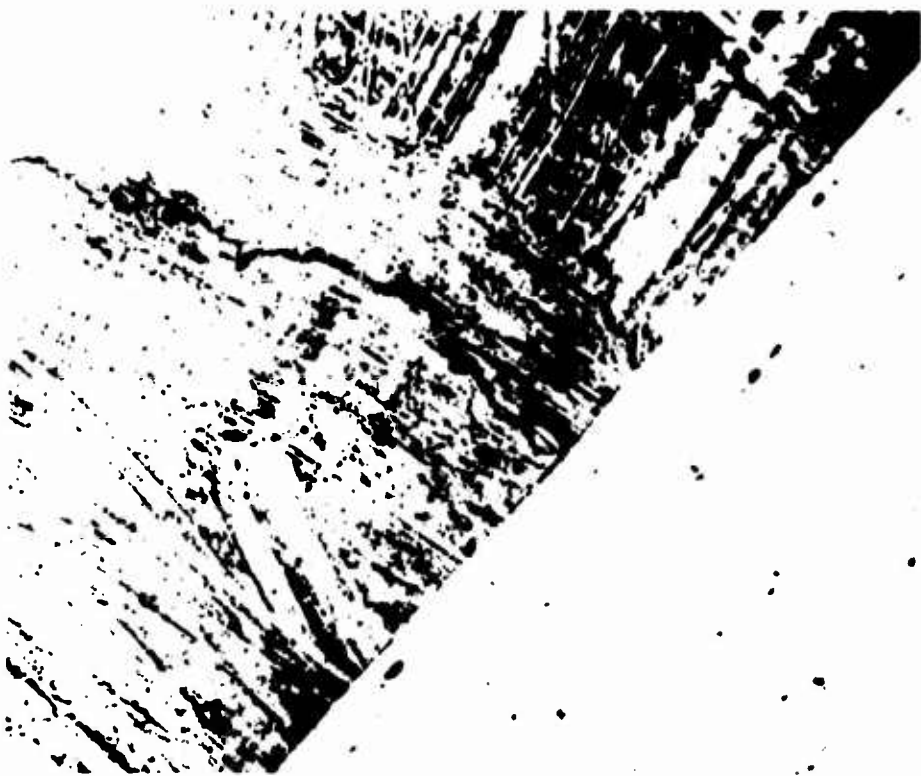


Figure 61. Photomicrograph of the Interface of a Cast Bond Showing Cracking in the Cast Material Typical of That Resulting From Insufficient Preheat of the Sheet Material (X200).

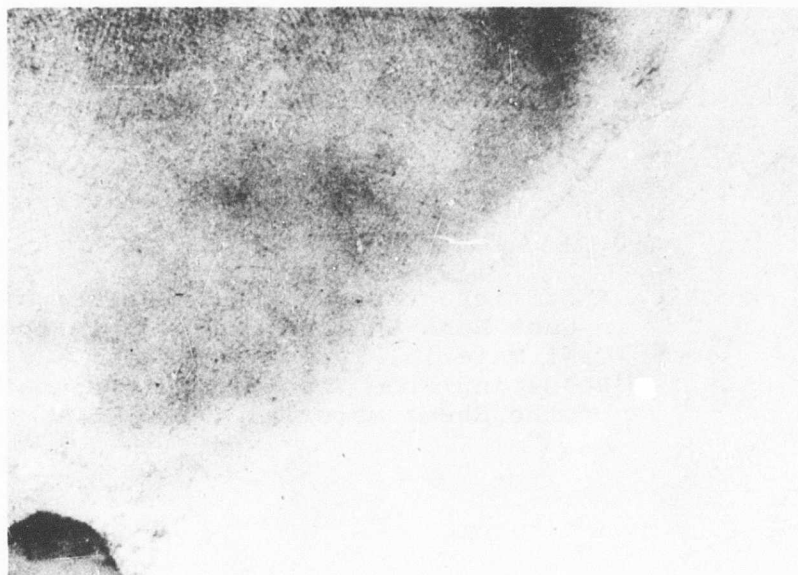
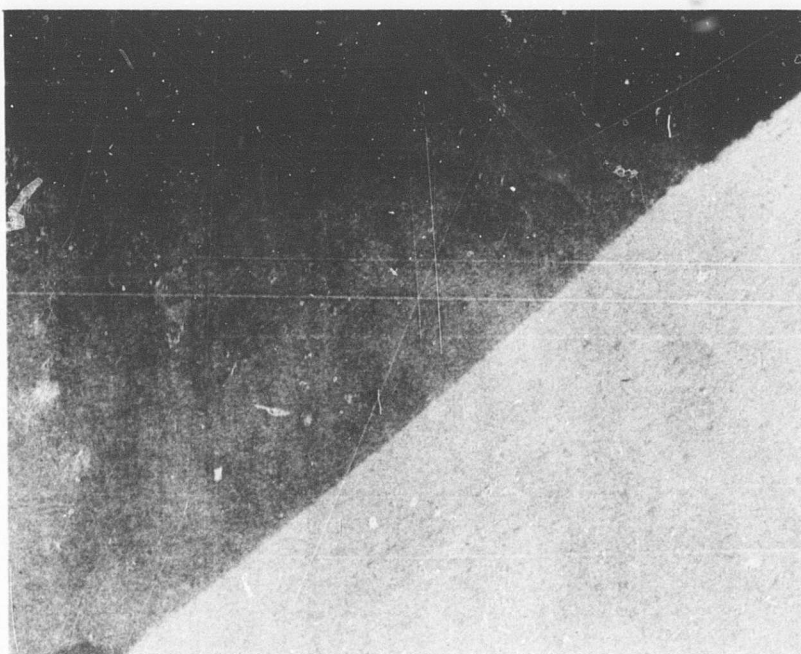


Figure 62. Examples of Cast-Bonded Joint
Produced Using Final Casting
Parameters (X50).

TABLE XVIII. RESULTS OF SHEAR TESTING
CAST-TO-SHEET BONDED SPECIMENS

Specimen No.	Specimen Description	Bonding Conditions Mold Temp/Melt Temp	Apparent Shear Stress (psi)
C-1	MAR-M 246/AIR* 213	2000°F/2700°F	57,800
C-2	MAR-M 246/Rene' 41	2000°F/2750°F	19,300
C-8	MAR-M 246/AIR 213	2000°F/2750°F	19,500
C-9A	MAR-M 246/AIR 213	2000°F/2750°F	5700
C-9B	MAR-M 246/AIR 213	2000°F/2750°F	21,400
C-10	* *MAR-M 246/AIR 213	2000°F/2750°F	64,200
C-11	* *MAR-M 246/AIR 213	2000°F/2750°F	51,300
C-12	* *MAR-M 246/AIR 213	2000°F/2750°F	31,900
C-13	* *MAR-M 246/Rene' 41	2000°F/2750°F	13,200
C-14	* *MAR-M 246/Rene' 41	2000°F/2750°F	68,500

*AIR - AiResist

**Replaced Mo Wire (0.040-in. diam) removed chemically.

4.3 SELECTION OF FINAL CANDIDATE JOINING PROCESSES

4.3.1 Strut/Disk Attachment

The candidate joining processes and associated material combinations selected for final testing are listed below:

1. Diffusion bonding with blade material of MAR-M 246 and disk material of Inconel 718.
2. Brazing with blade material of MAR-M 246 and disk material of Waspaloy.
3. Electron-beam welding with blade material of MAR-M 246 and disk material of Waspaloy.

4.3.2 Shell/Strut Attachment (Feasibility Study)

The preliminary joining evaluation for the shell/strut attachment indicated the following:

1. Diffusion bonding was shown to be a feasible technique. However, additional development would be required to achieve bonding in the component geometries required for a blade.
2. Shell/strut joining could be accomplished by brazing. However, this type of joint is considered unattractive because of the relatively low stress-rupture life of the braze alloys at the operating temperature of the shell/strut joint.
3. The cast-bonding technique offered a potential means of forming the strut and shell/strut bonding in one operation. Use of preplaced wires that can be subsequently removed to form cooling-air passages was shown to be a feasible approach. However, additional development of the cast-bonding technique is required to produce scale-size specimens.

5. FINAL SPECIMEN FABRICATION AND TESTING

This section describes the final specimen design, fabrication, and testing activities that concluded the blade/disk fabrication program.

The objectives of this program phase were to design, fabricate, inspect, test, and evaluate the test results of the final specimens. These specimens (diffusion-bonded, brazed, and electron-beam-welded) were configured to closely simulate the actual requirements for a turbine rotor.

5.1 SPECIMEN DESIGN

The final specimen design was based on the accumulated technology and experience gained from the aerothermodynamic design, mechanical design, and fabrication technology development efforts described in Sections 2, 3, and 4. The specimens were designed to simulate as closely as possible the geometry that would be required for the blade-disk attachment of an actual turbine rotor.

Subsequent subparagraphs describe the design for the diffusion bonded, brazed, and electron-beam-welded specimens, respectively.

5.1.1 Diffusion-Bonded Specimen Design

The specimen that was designed to simulate the diffusion-bonded attachment design concept is shown in Figure 63. The threaded end of the illustrated specimen simulates the blade pedestal element of the attachment. The pin-joint end simulates the two disk halves. The geometry of the final specimen design differed from that of the diffusion-bonded rotor design (Figure 24) as follows:

1. The bonded surfaces of the final specimen are defined by a rectangle rather than by the trapezoidal configuration of the diffusion-bonded rotor design.
2. No cooling-air entry holes were included in the final specimen design. Considerations of bond joint strength versus the load-carrying ability of the blade pedestal element of the attachment showed that the holes would have negligible effect upon the strength of the attachment.

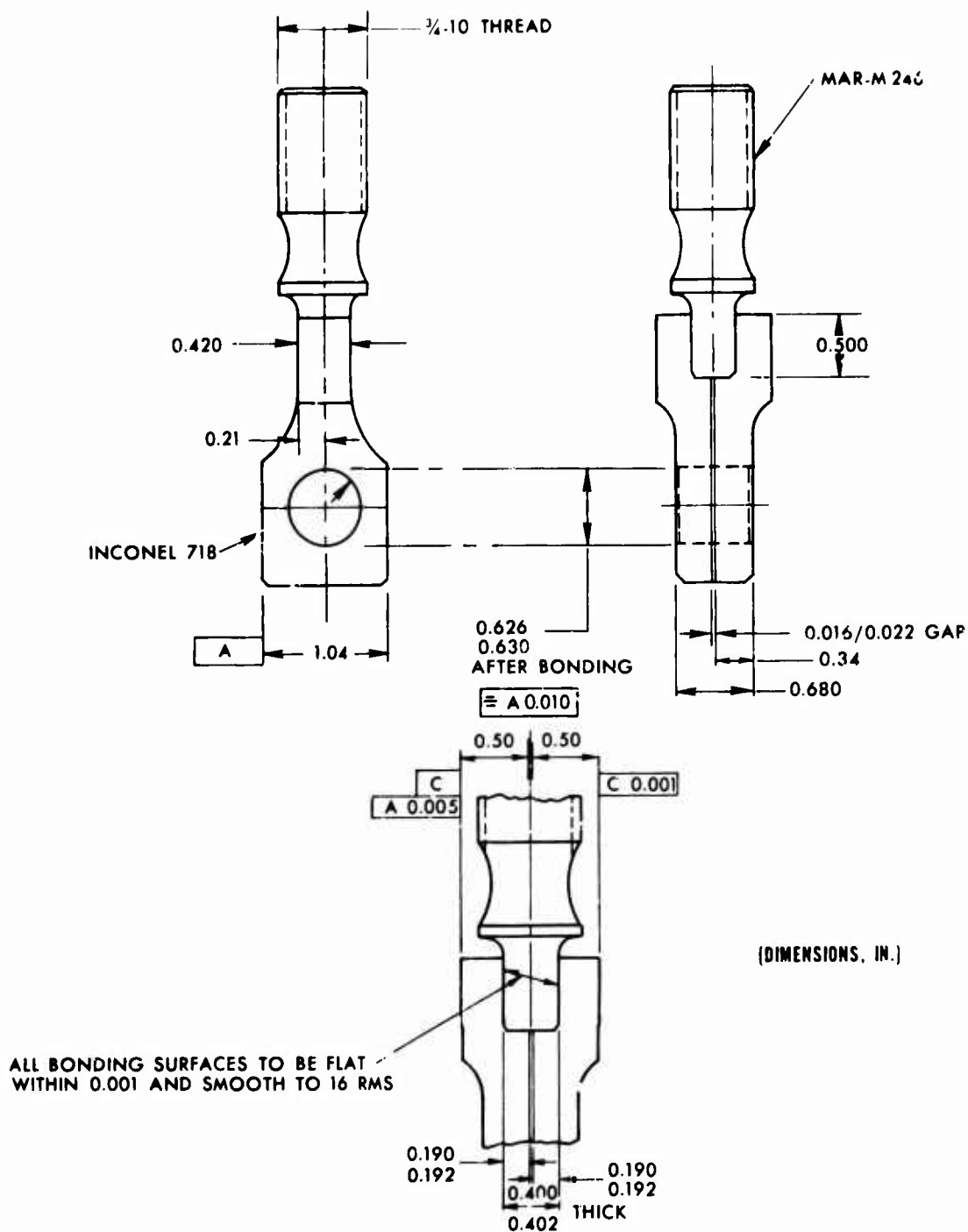


Figure 63. Diffusion-Bonded Final Specimen Design.

3. The disk elements of the final specimen were not designed to include simulation of the holes that relieve stress concentrations in the rotor assembly. Considerations of bond joint strength versus the load-carrying ability of the disk elements of the final specimen showed that the holes would have negligible effect upon the strength of the attachment.

5.1.2 Brazed Specimen Design

The specimen that was designed to simulate the brazed attachment concept is shown in Figure 64. The female component of the illustrated specimen simulates the blade pedestal element of the attachment, and the male component simulates the disk. The geometry of the final specimen design differed from that of the brazed-joint rotor design (Figure 25) as follows:

1. No cooling-air entry holes were included in the final specimen design. Analysis of the design indicated that these holes would have a negligible effect upon the strength of the attachment.
2. A full radius was provided at the bottom of the slotted blade pedestal of the final specimen rather than the two-radius configuration shown for the brazed-joint rotor design in an attempt to minimize stress concentrations.

5.1.3 Electron-Beam-Welded Specimen Design

The specimen that was designed to simulate the electron-beam-welded attachment concept is shown in Figure 65. The upper component simulates the blade pedestal element of the attachment. The other component simulates the disk. No differences from the geometry of the electron-beam-welded rotor design (Figure 26) were allowed in this final specimen design. The reason for this complete compliance is that the geometry of the joint, including the cooling-air entry passage, is considered to have a strong effect upon low-cycle-fatigue and stress-rupture-life characteristics of the attachment. Additionally, it was believed that welding the specimens individually would not provide a true simulation of the welding requirements associated with fabrication of a complete rotor assembly. Therefore, the specimens were welded in groups of six to more nearly simulate the attachment of blades to a rotor disk.

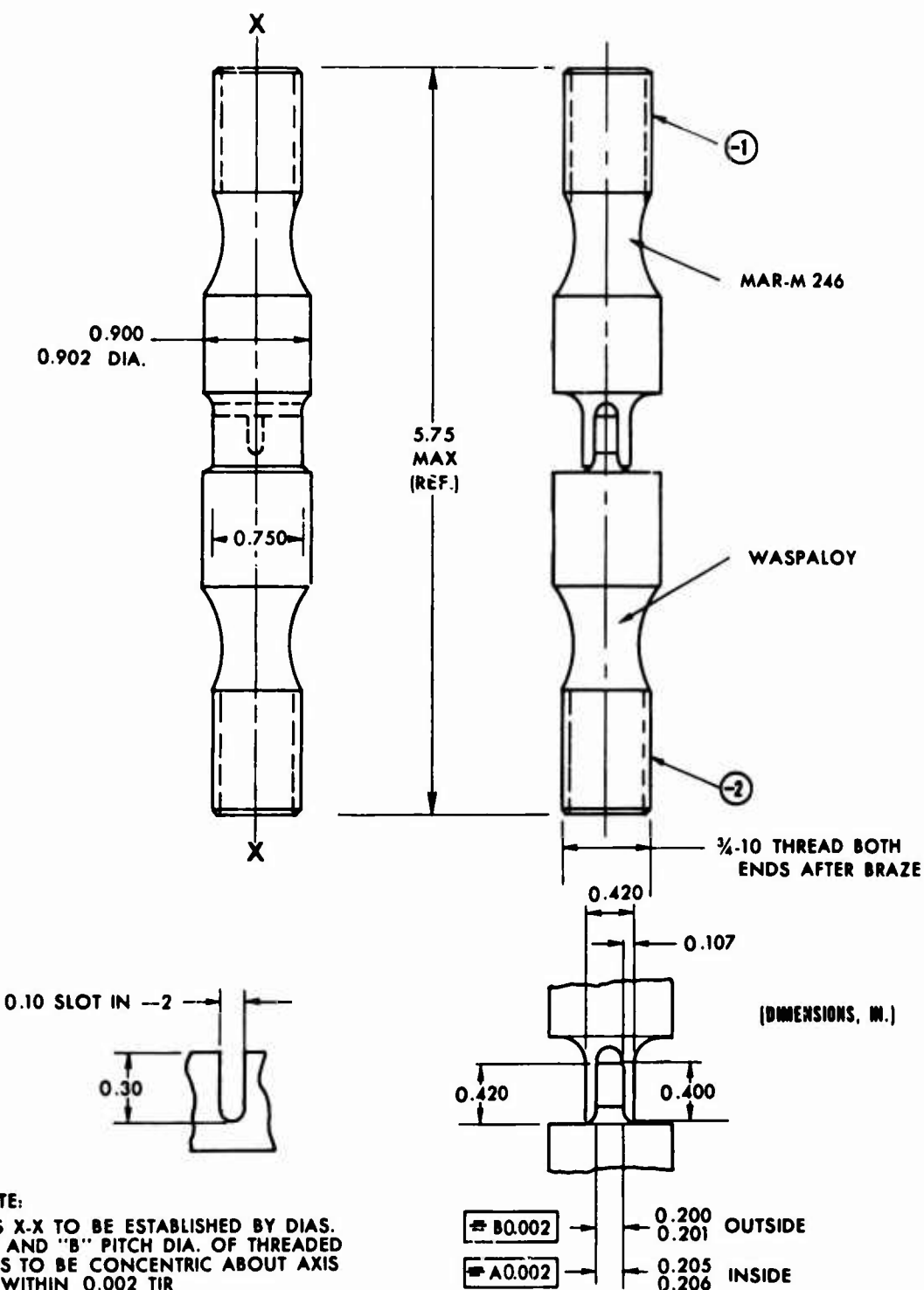


Figure 64. Brazed Final Specimen Design.

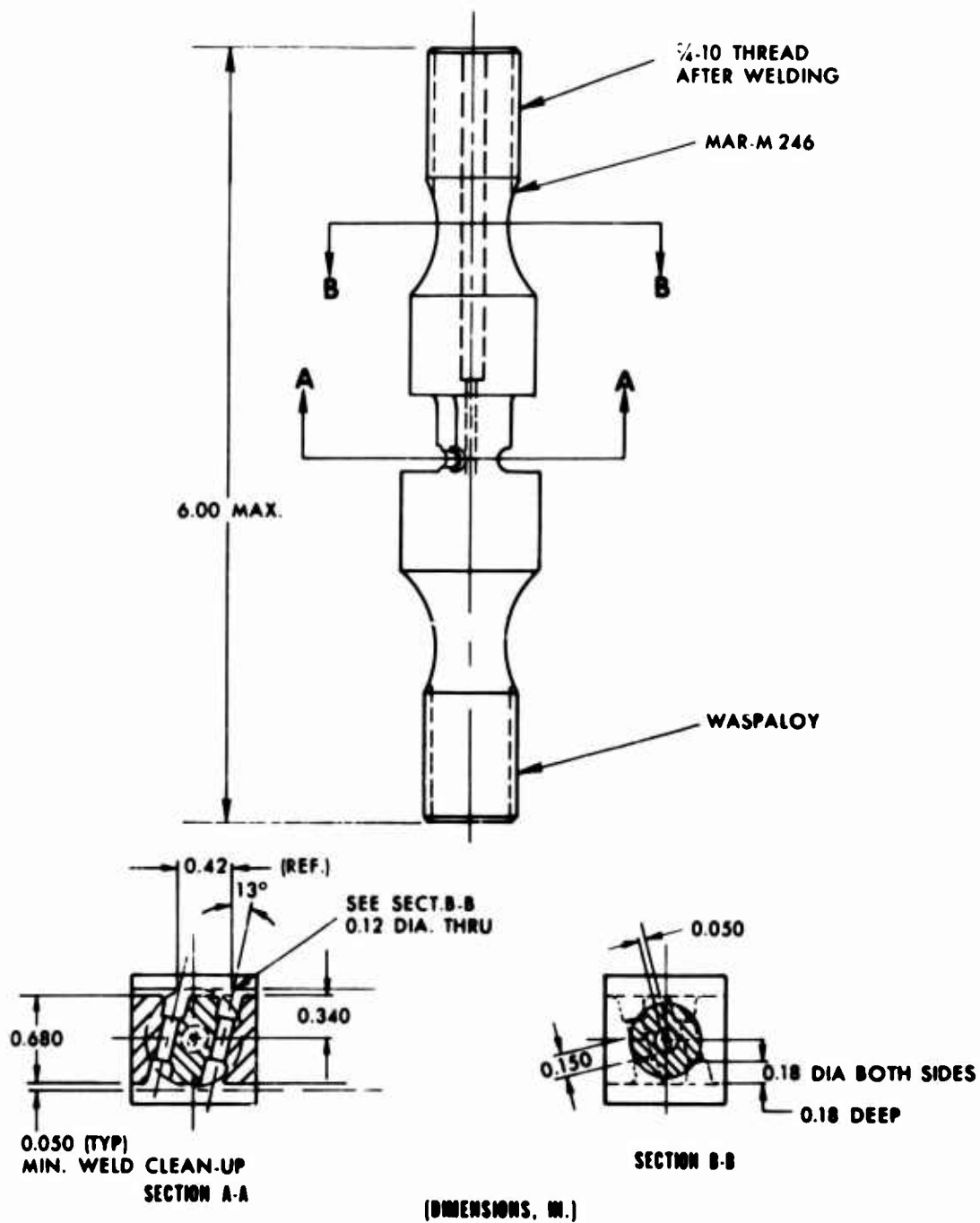


Figure 65. Electron-Beam-Welded Final Specimen Design.

5.2 SPECIMEN FABRICATION

Three alloys were required for fabrication of the final specimens: Inconel 718, Waspaloy, and MAR-M 246. The wrought materials (Inconel 718 and Waspaloy) were purchased in the form of bars 1.25 by 3.25 inches in cross section and 1 foot in length. The Inconel 718 was purchased to specification AMS 5662B in the solution heat-treated condition, and the Waspaloy material was purchased to Specification AMS 5707B in the precipitation heat-treated condition and was solution heat-treated (1850°F for 4 hours) prior to machining. The MAR-M 246 material was purchased in the form of cast blocks 1.25 by 1.25 by 3 inches in size. Casting was performed in inoculated molds in an attempt to produce the small grain size considered desirable for welding.

Certified compositions for each of these three types of material are listed in Table XIX.

Subsequent subparagraphs describe the fabrication sequence for the diffusion-bonded, brazed, and electron-beam-welded specimens.

TABLE XIX. CERTIFIED COMPOSITIONS FOR MATERIALS
USED IN THE FINAL TEST SPECIMENS

Element	Inconel 718	Waspaloy	MAR-M 246
C	0.043	0.038	0.14
Mn	0.10	0.03	0.10
P	0.008	0.007	-
S	0.006	0.004	0.003
Si	0.16	0.10	0.10
Cr	18.60	19.91	8.76
Ni	52.40	Bal.	Bal.
Cu	0.03	0.02	-
Mo	3.18	4.27	2.42
Ti	0.89	3.00	1.40
Cb/Ta	5.10	-	1.55
Al	0.55	1.31	5.50
Co	-	14.23	9.90
Zr	-	0.06	0.03
Fe	-	0.70	0.10
B	-	0.006	0.011
W	-	-	9.98

5.2.1 Diffusion-Bonded Specimen Fabrication

The fabrication sequence for the diffusion-bonded specimens is shown in Figures 66 through 70. Figure 66 shows the component parts of the specimen after preliminary machining. The center piece (threaded) was of MAR-M 246 to simulate the blade pedestal element, and the top and bottom pieces were machined from Inconel 718, simulating the disk. Although the preliminary test specimens described in Section 4.2.1.1 were polished to a No. 3 finish, the final specimens were left "as ground" with a surface finish of approximately 16 rms. This value was considered to be the practical limit for surface finish that could be tolerated in economically feasible designs of this type. An interface diffusion aid, consisting of 0.0005-inch nickel plating applied to the MAR-M 246 surfaces, was utilized for the diffusion-bonded attachment.

Figures 67 and 68 show the final specimen as assembled and as tack-welded prior to the bonding operation. Tack welding was required to ensure the maintenance of alignment during assembly of the specimen into the pressing die. These welds were superficial and in all cases were broken upon the application of bonding pressure, since some deformation occurred in the components. The final specimens were assembled with a shim in place, as shown in Figure 67, in order to maintain a small gap at the end and thus allow for some deformation without contact on surfaces that were not to be bonded.

The assembled and tack-welded final specimens were bonded in the graphite die shown in Figure 69. The specimens were placed in the die in such a way that the total load applied by the press was carried across the surfaces to be bonded. Equipment and procedures used for bonding were identical with those used for the diffusion-bonding preliminary test evaluations of Section 4.2.1. The die assembled with the final specimen in place was positioned in the pressing furnace, and the furnace chamber was evacuated to less than 1 micron pressure. As in the preliminary test, heating of the specimen to 1800°F was accomplished by induction heating of the graphite die, and the temperature was measured by a thermocouple positioned in the die wall. Once the required temperature was reached, the pressure was increased to 12,900 psi at the bonding interfaces and held for 30 minutes. These conditions resulted in the small amount of deformation of the specimen during the bonding that is required to help ensure a more complete joint contact. However, additional temperature or pressure application would have resulted in excessive deformation.

Upon completion of the bonding operation, the final specimens were final-machined as shown in Figure 70. Final machining was followed by heat treatment to develop full properties of the Inconel 718 material. The 1800°F temperature used for bonding was in the solution-heat-treating range for the Inconel 718 material; therefore, only the precipitation heat treatment was required. This consisted of 1325°F for 8 hours, cooling at 100°F per hour to 1150°F, and holding for 8 hours.

After completion of heat treatment, the specimens were ready for inspection and test. A clevis-type holder was prepared, as shown in Figure 71, for use on the pin joint end of the specimen during testing.

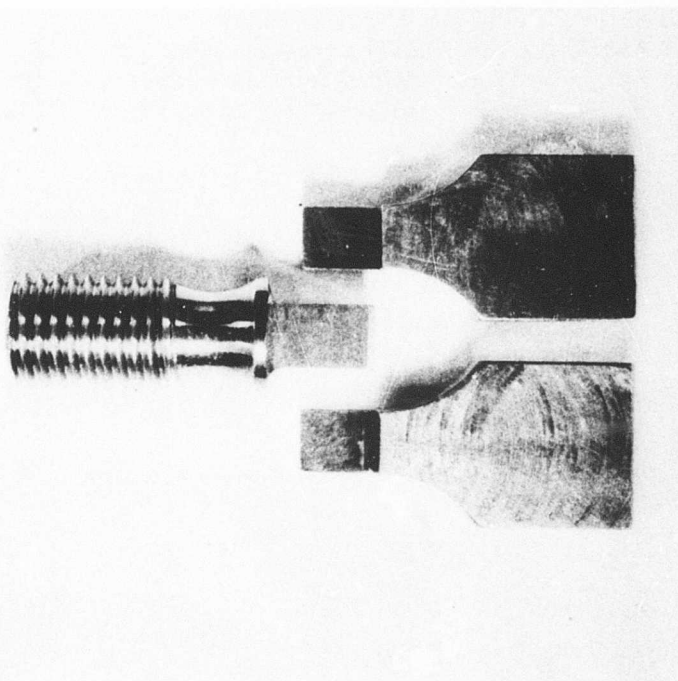


Figure 66. Machined Diffusion-Bonded Final Specimen Elements Before Assembly.

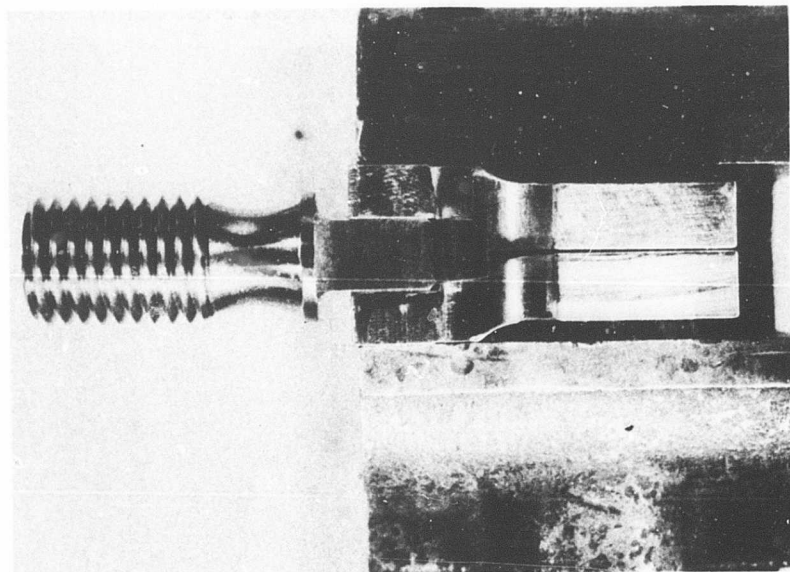


Figure 67. Diffusion-Bonded Final Specimen Assembled in Vice With Shim Installed Prior to Tack Welding.

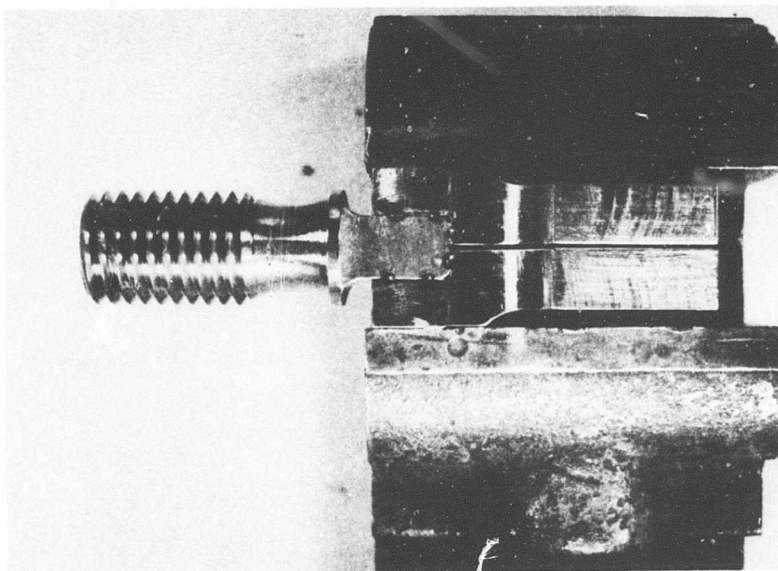


Figure 68. Diffusion-Bonded Final Specimen With Shim Removed and Tack Welding Complete.

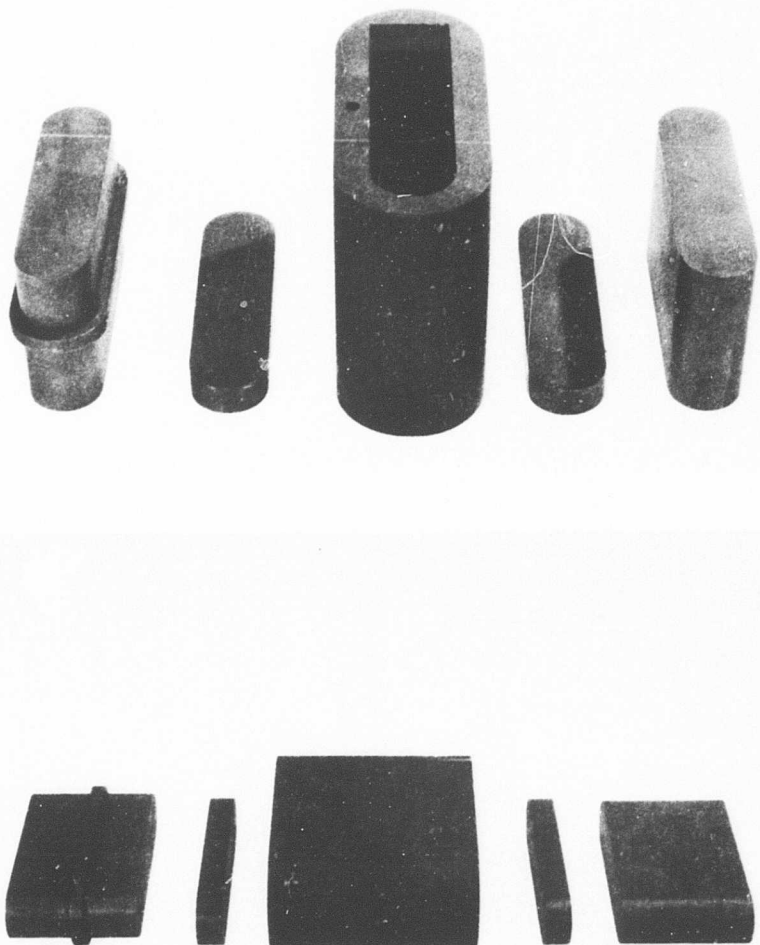


Figure 69. Two Views of the Graphite Die Assembly
Used During the Diffusion Bonding
Operation on the Final Specimen.

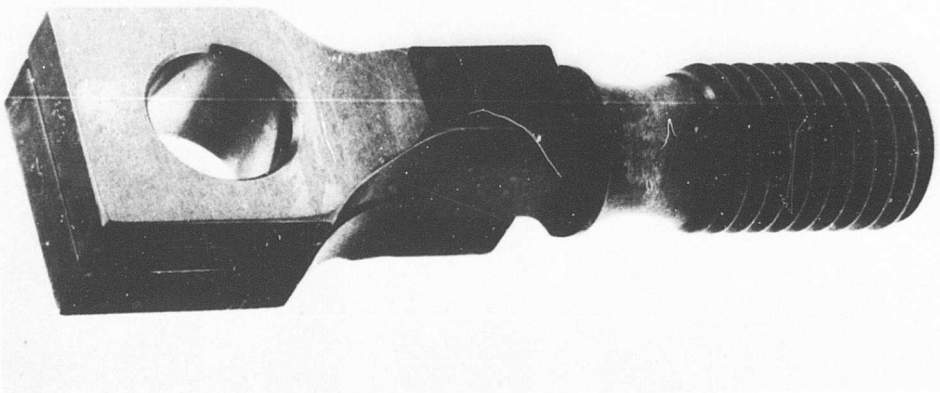


Figure 70. Diffusion-Bonded Final Specimen
After Completion of Bonding Operation
and Final Machining.

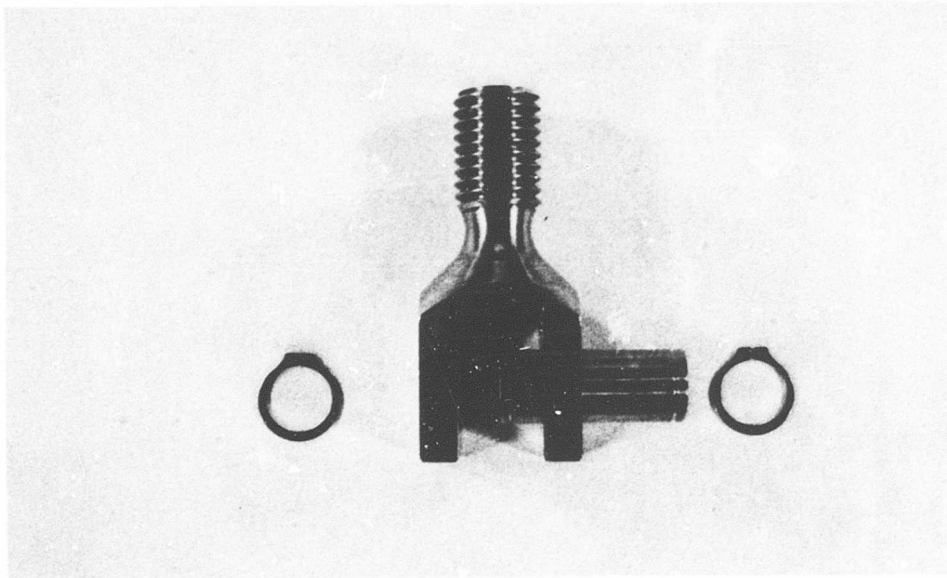


Figure 71. Clevis Assembly Used for Testing
of the Diffusion-Bonded Specimens.

5.2.2 Brazed Specimen Fabrication

The fabrication sequence for the brazed specimens is shown in Figures 72 through 76. Figure 72 shows the component parts of the specimen after preliminary machining. Materials used were MAR-M 246 to simulate the blade pedestal element and Waspaloy to simulate the disk. The portions of the final specimens upon which brazing flow was required were nickel-plated (0.0004 inch) to ensure adequate wetting of the surfaces. Nicrobraz 30 brazing powder in a paste form was preplaced on the final specimens prior to assembly in a jig.

The jig (Figure 73) consisted of a V-block on which the two parts could be clamped and held in proper alignment during the tack welding of spacers, as shown in Figure 74. These spacers served to maintain specimen alignment and gap during the brazing operation. Prior to brazing, a small excess of powder was placed in the fillet area to allow "feeding" of the joint during the brazing cycle.

As in the preliminary test evaluations of 4.2.2, brazing was performed in a vacuum furnace at a pressure of 0.5 micron and with a cycle of $2150^{\circ} \pm 10^{\circ}\text{F}$ for 20 minutes. An example of an as-brazed specimen is shown in Figure 75. Following the brazing cycle, specimens were heat-treated to develop full properties in the Waspaloy material. This treatment consisted of a stabilization treatment at 1550°F for 4 hours (air-cool) followed by a precipitation heat treatment at 1400°F for 16 hours (air-cool). Spacers were then cut, as shown in Figure 76, and the specimens were ready for test.

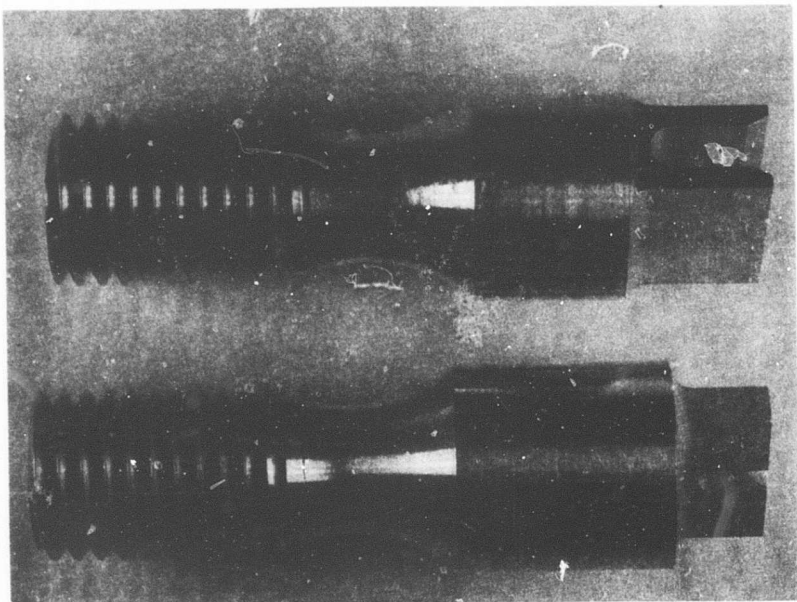


Figure 72. Component Parts of the Brazed Final Specimen After Final Machining.

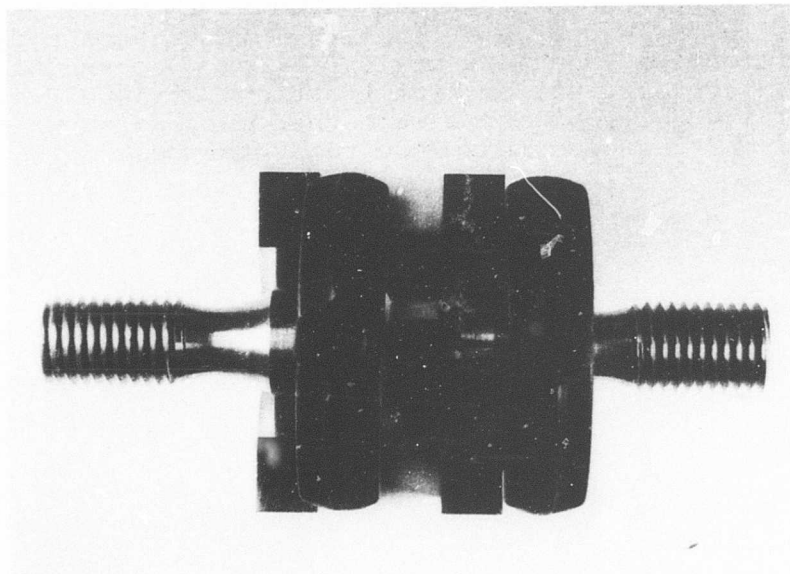


Figure 73. Assembly Jig With the Brazed Final Specimen in Place.

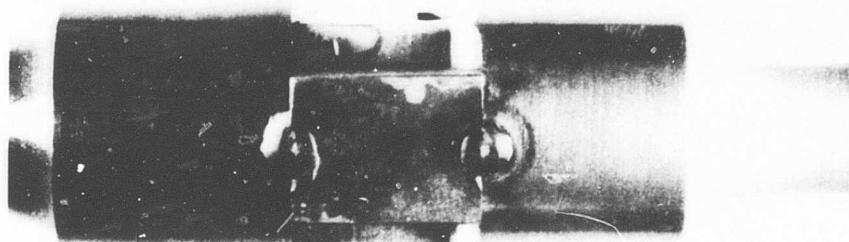


Figure 74. Spacers Tack-Welded in Place on
Brazed Final Specimen.

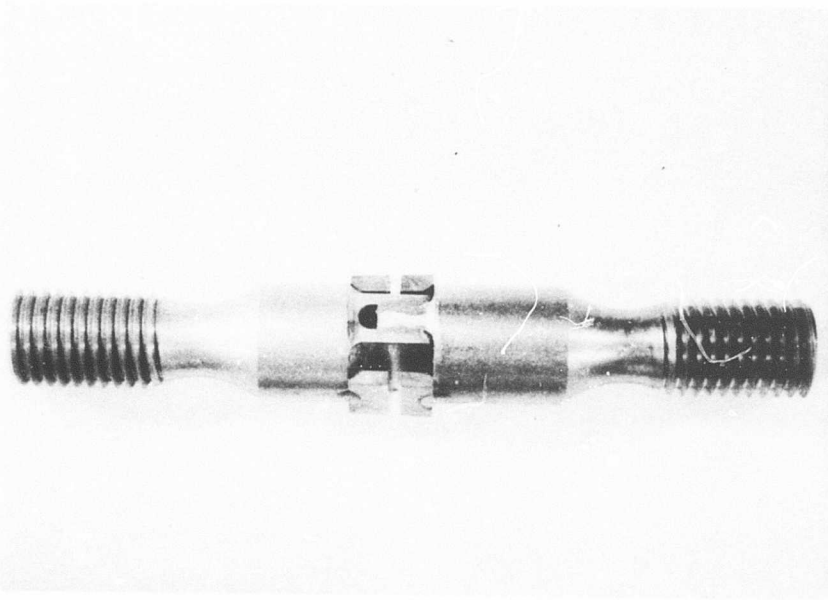


Figure 75. Final Specimen After Completion
of Brazing Operation.

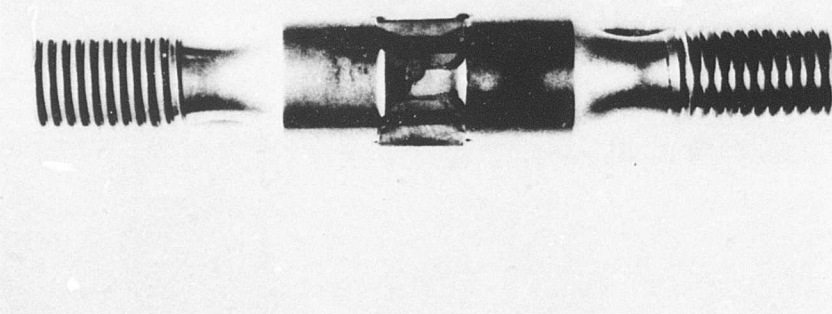


Figure 76. Brazed Final Specimen Ready for Testing (Spacers Have Been Cut).

5.2.3 Electron-Beam-Welded Specimen Fabrication

The fabrication sequence for the electron-beam-welded specimens is shown in Figures 77 through 85. Figure 77 shows the machined Waspaloy block that simulated the disk material. As shown in the figure, a single-pass weld was run the length of the block to simulate the weld that would be required to join the two halves of the disk together. A section through this weld is shown in Figure 78. Blocks of the alloy MAR-M 246 (blade pedestal material) were given a heat treatment of 2000°F for 2 hours prior to machining into the geometry shown in Figure 79. Experience gained during the electron-beam-welding preliminary test evaluations had shown that such a heat treatment tended to reduce the severity of weld cracking in the MAR-M 246.

Machined MAR-M 246 blade pedestal blocks, with MAR-M 246 alloy spacers, were assembled with the large Waspaloy disk block as shown in Figure 79 and were clamped into the welding jig as shown in Figure 80. The jig was designed to hold six of the MAR-M 246 alloy blade pedestal blocks against a Waspaloy disk block (Figure 77) during the welding operation. Due to the geometry of the blade pedestal blocks, spacers were required between each of the six blocks at the "root-end" to permit an uninterrupted single-pass weld. A slight relief was machined in the "root-end" of the spacer at the spacer/pedestal interface. This relief was machined to help simulate an actual rotor configuration where the blades are spaced 0.003 to 0.005 inch apart.

The assembled blocks (in the welding fixture) were welded by a single-pass electron-beam weld with use of the parameters listed in Table XX. In order to ensure complete and uniform penetration, a weld backup strip was used, as shown in Figure 81. Figures 82 and 83 show front and back views, respectively of a final specimen with the weld backup strip removed. The welded assemblies were given a stress-relieving heat treatment consisting of:

1. Heat to 1000°F and hold 30 minutes.
2. Heat to 1840°F rapidly and hold for 2 hours.
3. Argon-fan-cool in furnace to achieve as rapid a cooling rate as possible.

The stress-relieving heat treatment served to relieve welding stresses and to solution the Waspaloy material so that it could respond to subsequent heat treatment.

The assemblies were then cut apart, and individual specimens, as shown in Figure 84, were final-machined, including the hole through the blade pedestal base, to simulate a cooling-air passage. The final step in specimen preparation was the heat treatment of the specimen to develop full properties in the Waspaloy material. This treatment consisted of:

Stabilization	1550°F for 4 hours and air-cool
Precipitation treatment	1400°F for 16 hours and air-cool

Following this final heat treatment the specimens were ready for test. Figures 85 and 86 show front and back views of the joint-test section of an electron-beam-welded final specimen.

**TABLE XX. ELECTRON-BEAM WELDING PARAMETERS
USED FOR FINAL TEST SPECIMENS**

Material - Waspaloy/MAR-M 246	Vacuum - 1 x 10 torr
Penetration - 0.790 inch	Operator Name - R. Custer
E. B. Machine Serial No. - H.S. 335	Gun Type - R-40
Accelerating Voltage - KV 140	Gun to Work Distance - 6"
Beam Current - ma	Beam Deflection - None
Travel Speed - I.P.M.	Joint Type - Butt/backup
Pot. Setting - Speed	215

SPECIAL TECHNIQUES: Spot-tack each blade and spacer.

140 Kv

3 ma

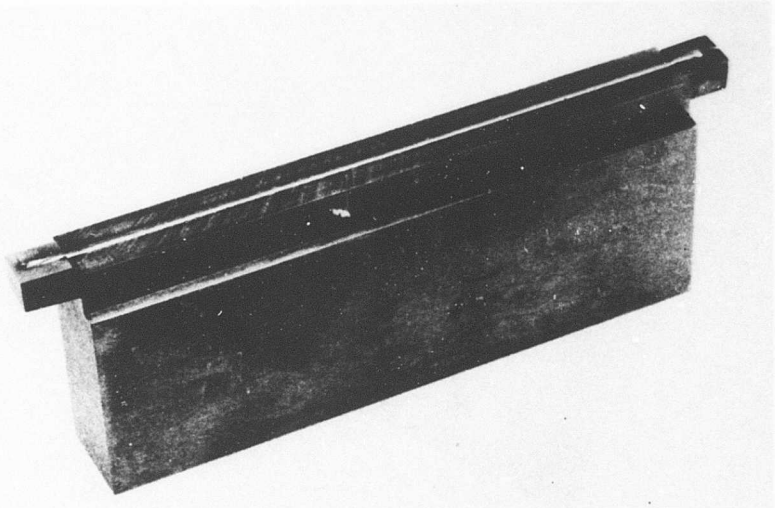


Figure 77. Machined Waspaloy Block That Simulated the Disk Element of the Electron-Beam-Welded Final Specimen.

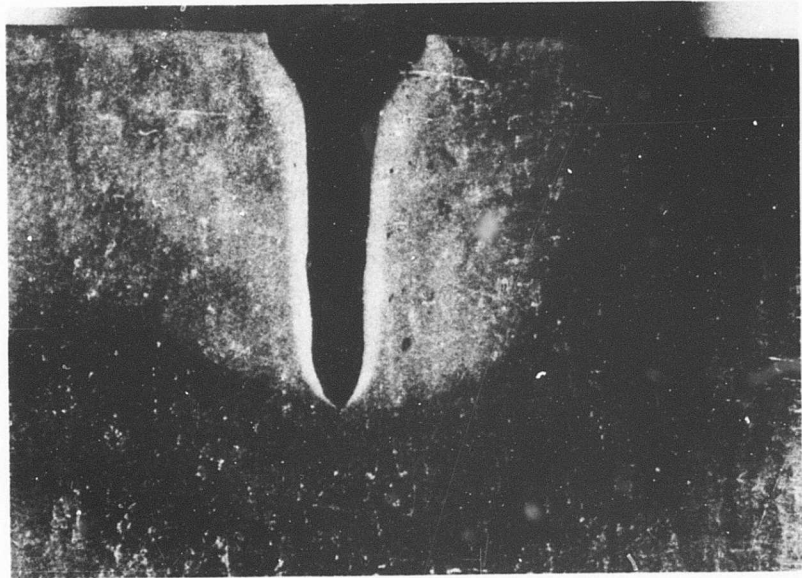


Figure 78. Section Through Single-Pass Weld of Electron-Beam-Welded Final Specimen Disk Element.

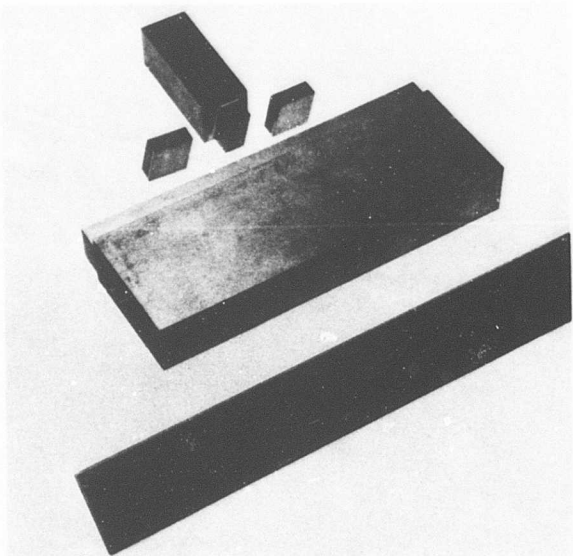


Figure 79. Elements of Electron-Beam-Welded Final Specimens Prior to Joining.

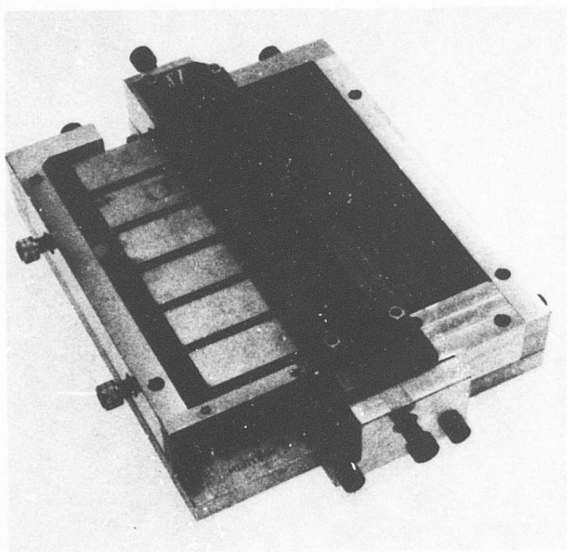


Figure 80. Elements of Electron-Beam-Welded Final Specimens Clamped in Welding Jig.

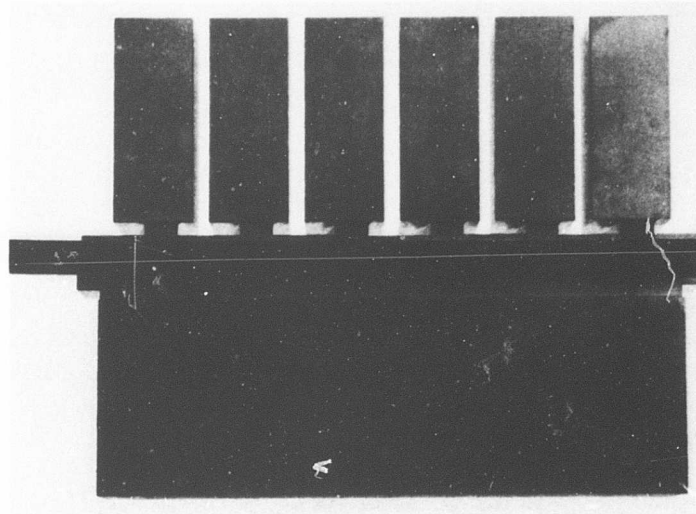


Figure 81. Electron-Beam-Welded Final Specimen With Backup Strip in Place.

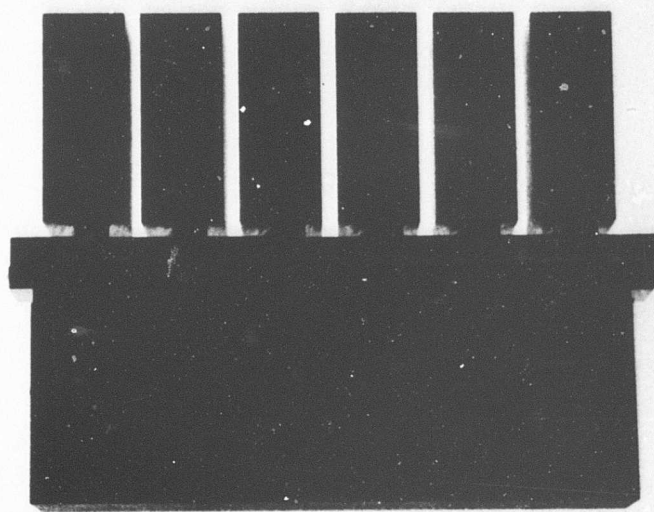


Figure 82. Front View of an Electron-Beam-Welded Final Specimen With Weld Backup Strip Removed.

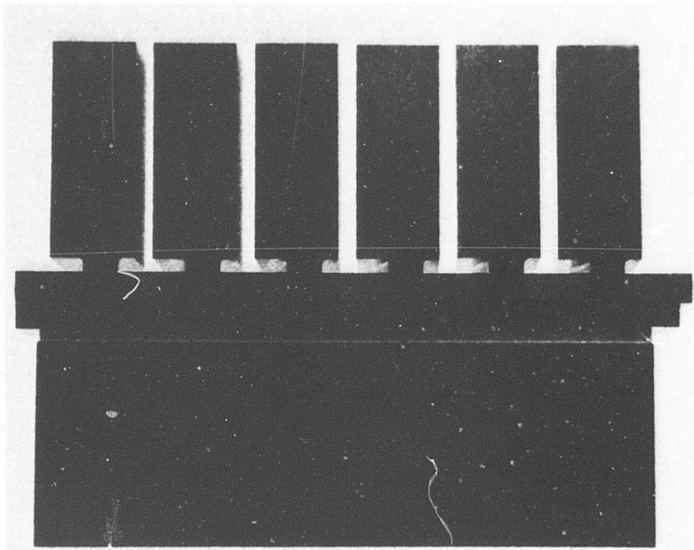


Figure 83. Back View of an Electron-Beam-Welded Final Specimen With Weld Backup Strip Removed.

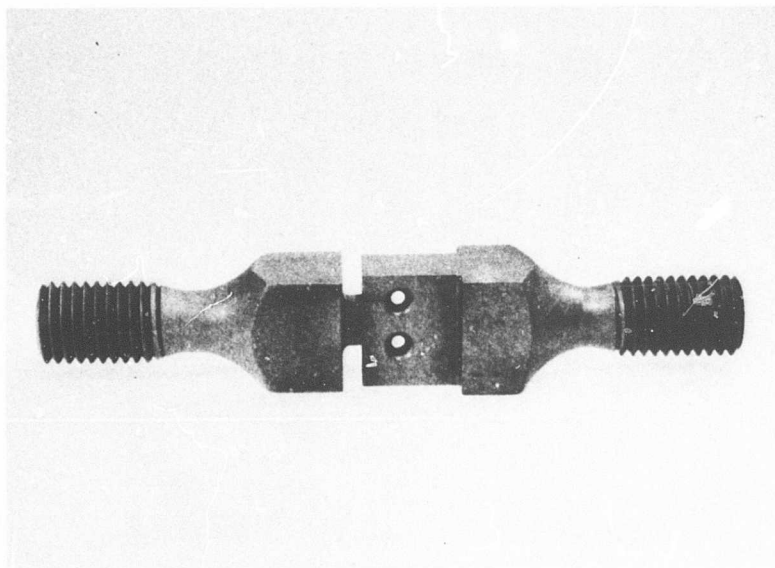


Figure 84. Electron-Beam-Welded Final Specimen After Completion of Final Machining.

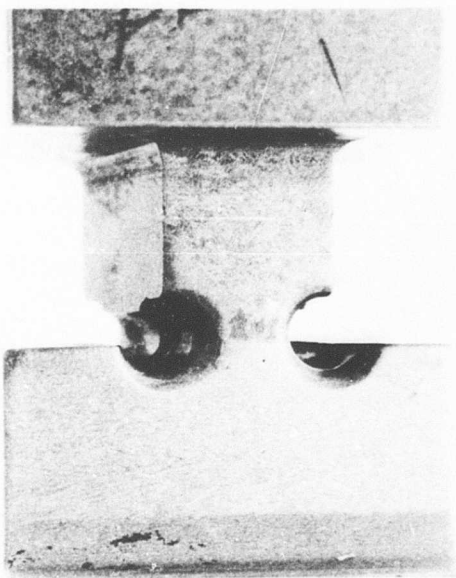


Figure 85. Front View of Joint-Test Section of an Electron-Beam-Welded Final Specimen.

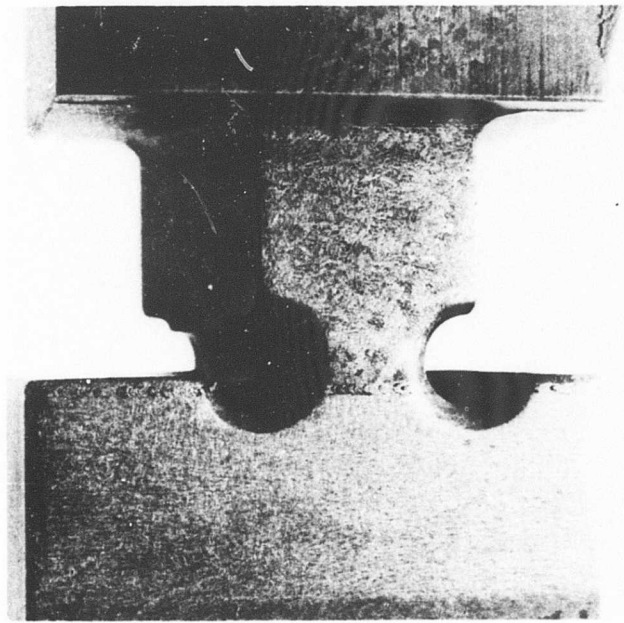


Figure 86. Back View of Joint-Test Section of an Electron-Beam-Welded Final Specimen.

5.3 INSPECTION OF FINAL SPECIMENS

All three types of the final specimens were macroscopically examined for defects prior to testing to determine the effectiveness of inspection procedures. In addition, selected specimens of each type were sectioned and inspected microscopically. Subsequent subparagraphs present the inspection results for the diffusion-bonded, brazed, and electron-beam-welded specimens, respectively.

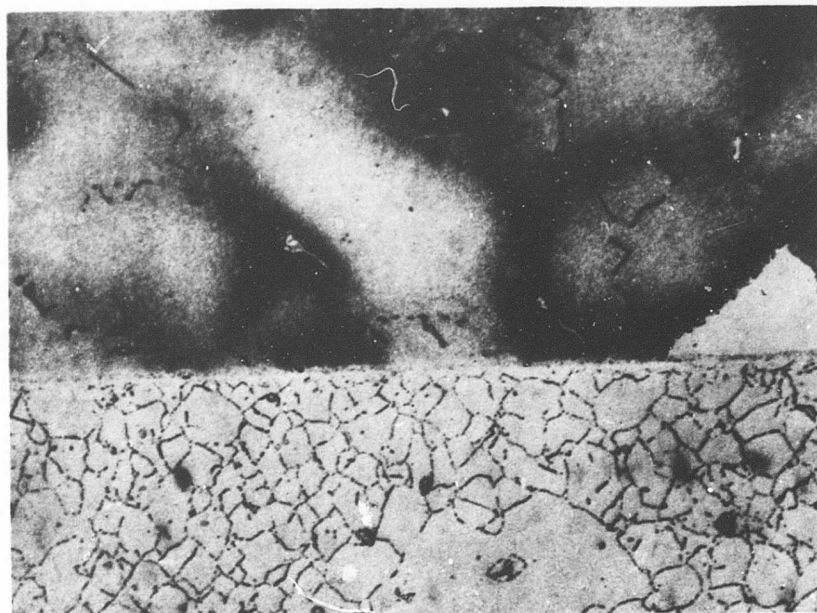
5.3.1 Diffusion-Bonded Specimens

The diffusion-bonded specimens could not be readily inspected for quality of the bond. The best control check was found to be a micrometer measurement of the width of the two Inconel 718 portions of the specimen transverse to the direction of loading and in the bonded region. In this area, on a specimen subjected to the proper bonding conditions, the Inconel 718 material yielded in compression and bulged to give a maximum measurable width of from 0.005 to 0.010 inch greater than the prebonded width. Both of the Inconel 718 pieces were measured on each specimen, and the specimen was rejected if the deformation was not within the required limits on each side.

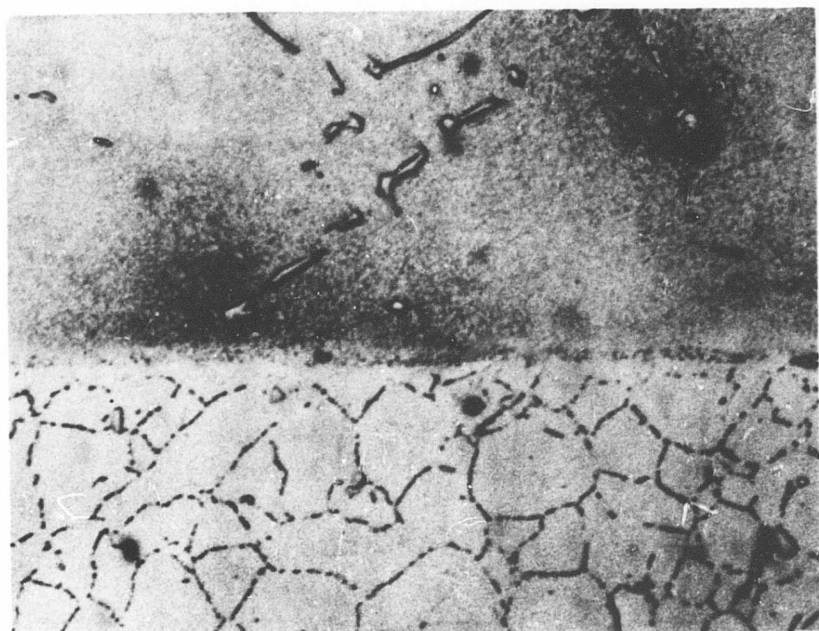
Metallographic examination of typical joints indicated two possible bond conditions, as shown in Figures 87 and 88. A good bond is shown in Figure 87, as evidenced by apparent complete diffusion of the nickel interface material and a bond line showing essentially no defects such as voids or inclusions. Figure 88 shows a less desirable bond condition; the bond line is somewhat discontinuous due to small voids. It was not possible to nondestructively inspect the joint to evaluate the bond quality, and it was also found that a single bond might, at various points, show both acceptable and non-acceptable bond conditions.

5.3.2 Brazed Specimens

Brazed specimens were examined visually for braze flow, and selected specimens were sectioned for metallographic examination. A typical brazed joint is shown in Figure 89. The specimens examined metallographically indicated the brazed joints to be of uniform and consistent quality.

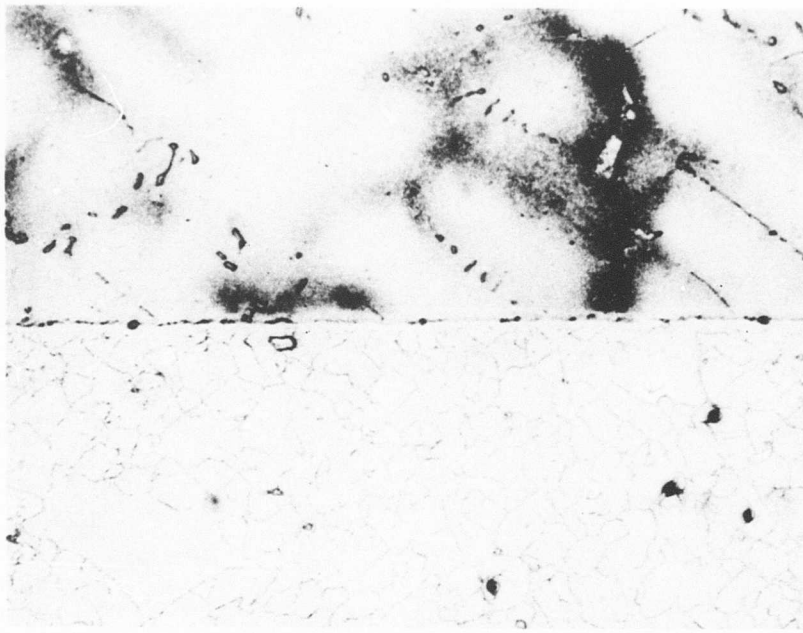


X200

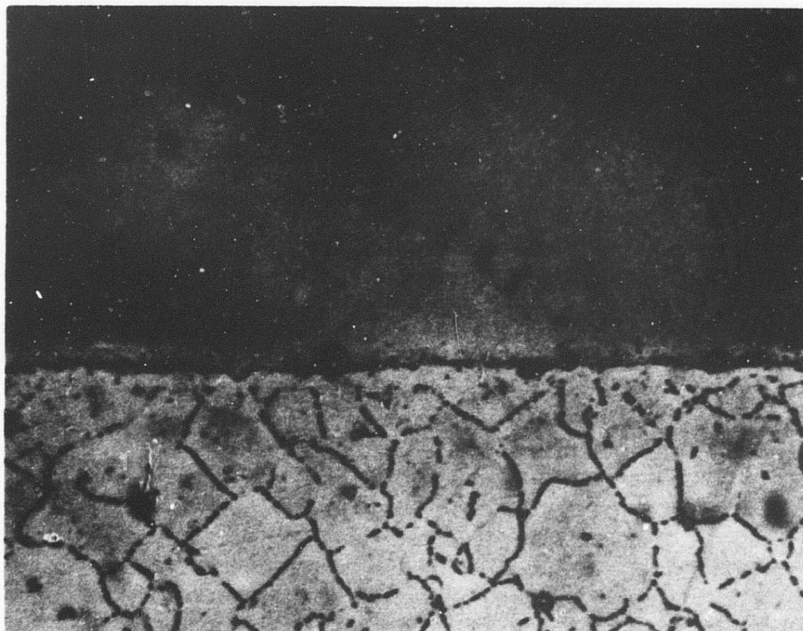


X500

Figure 87. Photomicrographs of a Typical Bonded Joint of a Diffusion-Bonded Final Specimen Showing No Defects.



X200



X500

Figure 88. Photomicrographs of a Typical Bonded Joint of a Diffusion-Bonded Final Specimen Showing Defects.

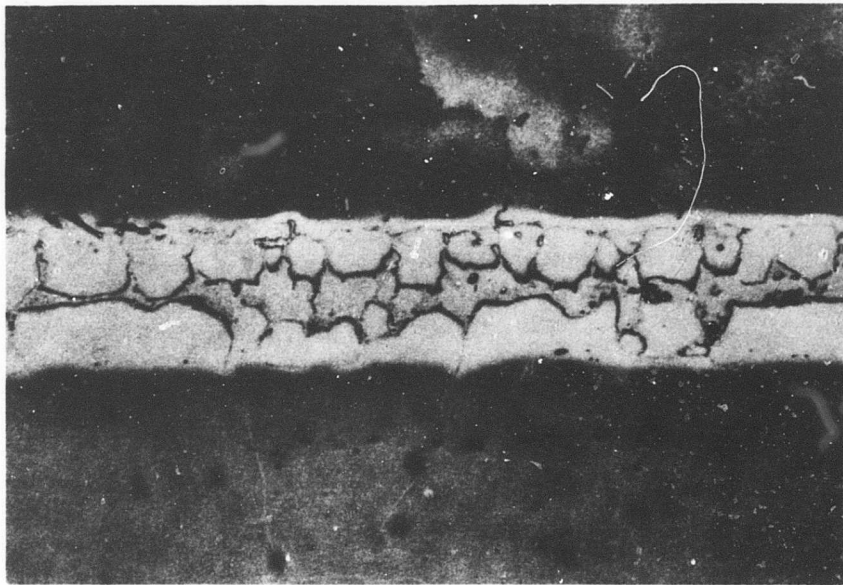


Figure 89. Photomicrograph of a Typical Joint of a Brazed Final Specimen (X200).

5.3.3 Electron-Beam-Welded Specimens

Each of the electron-beam-welded specimens was inspected by the use of dye-penetrant methods, and selected specimens were sectioned for metallographic examination. All specimens were found to have at least minor indications in the region of the rivet holes when examined by penetrant techniques. Examples of the indications and of the discontinuities producing them are shown in Figure 90.

Figure 91 is a photomicrograph of a typical weld spike produced in the final specimens. Cracking at the interface of the weld zone and the MAR-M 246 material, as shown in Figure 92, was expected. This type of cracking, although now minimized by adjusting welding parameters, was present in the large size electron-beam-welded specimens of the preliminary test evaluation described in Section 4.2.3. The most severe cracking found in the final specimens is shown in Figure 93.

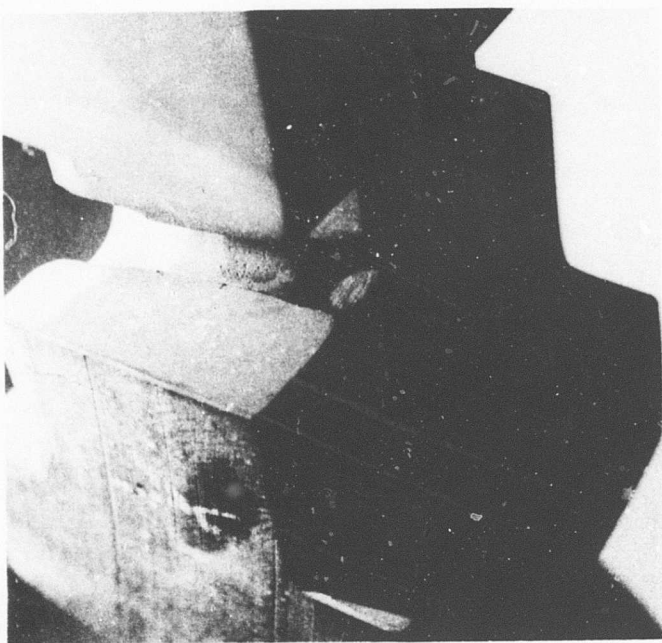
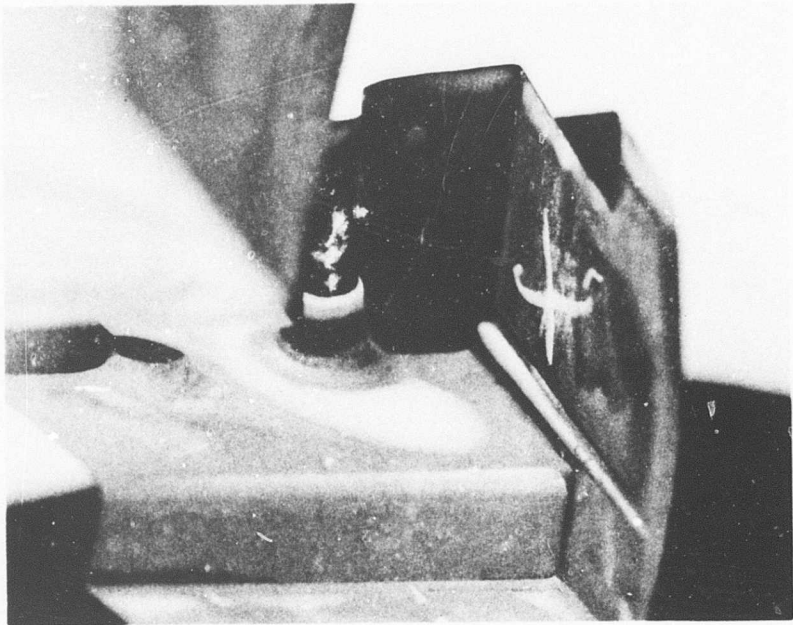


Figure 90. Example of Indications Revealed by Dye-Penetrant Inspection of an Electron-Beam-Welded Final Specimen.

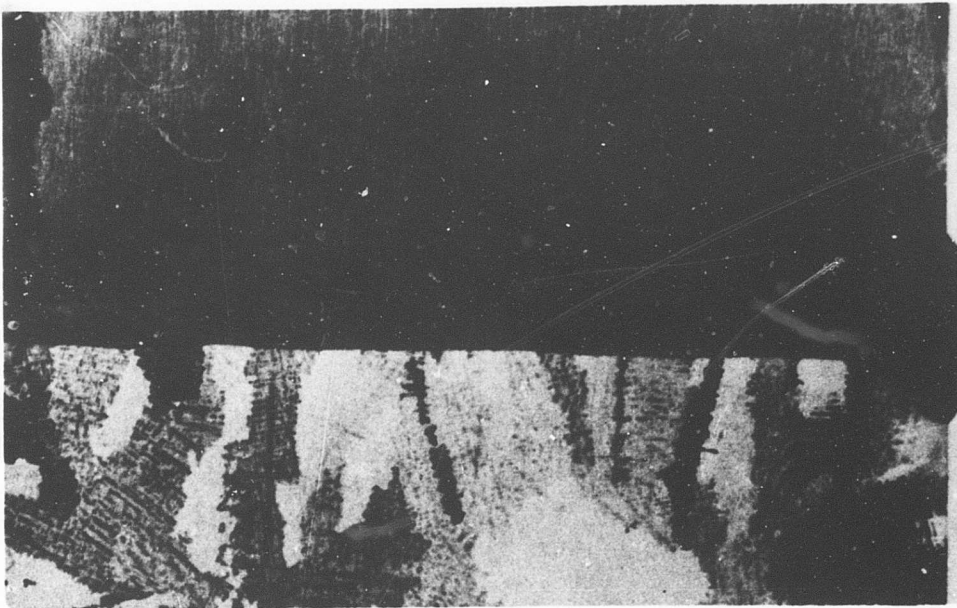


Figure 91. Typical Weld Spike Produced in an Electron-Beam-Welded Final Specimen (Depth Penetration 0.790 Inch).

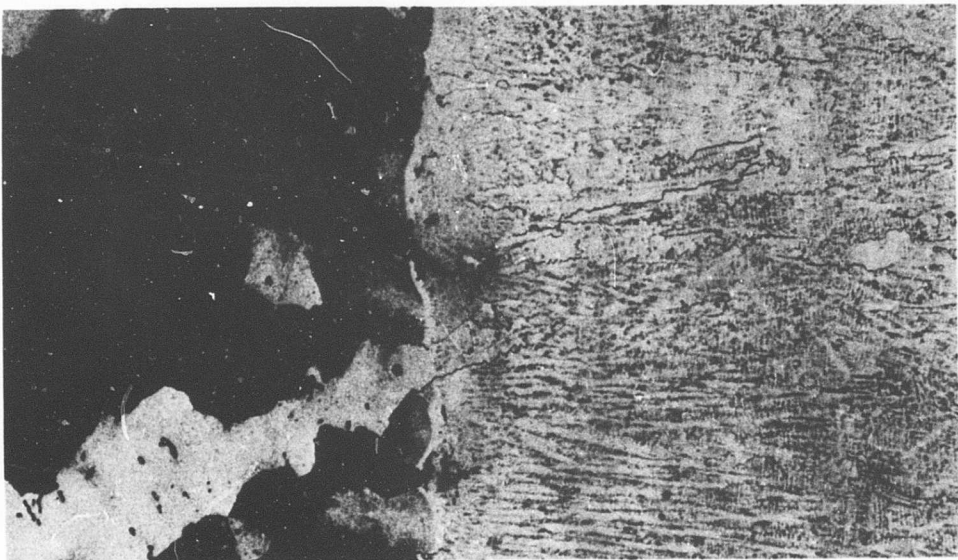


Figure 92. Typical Cracking at the Weld Zone Interface of an Electron- Beam-Welded Final Specimen.

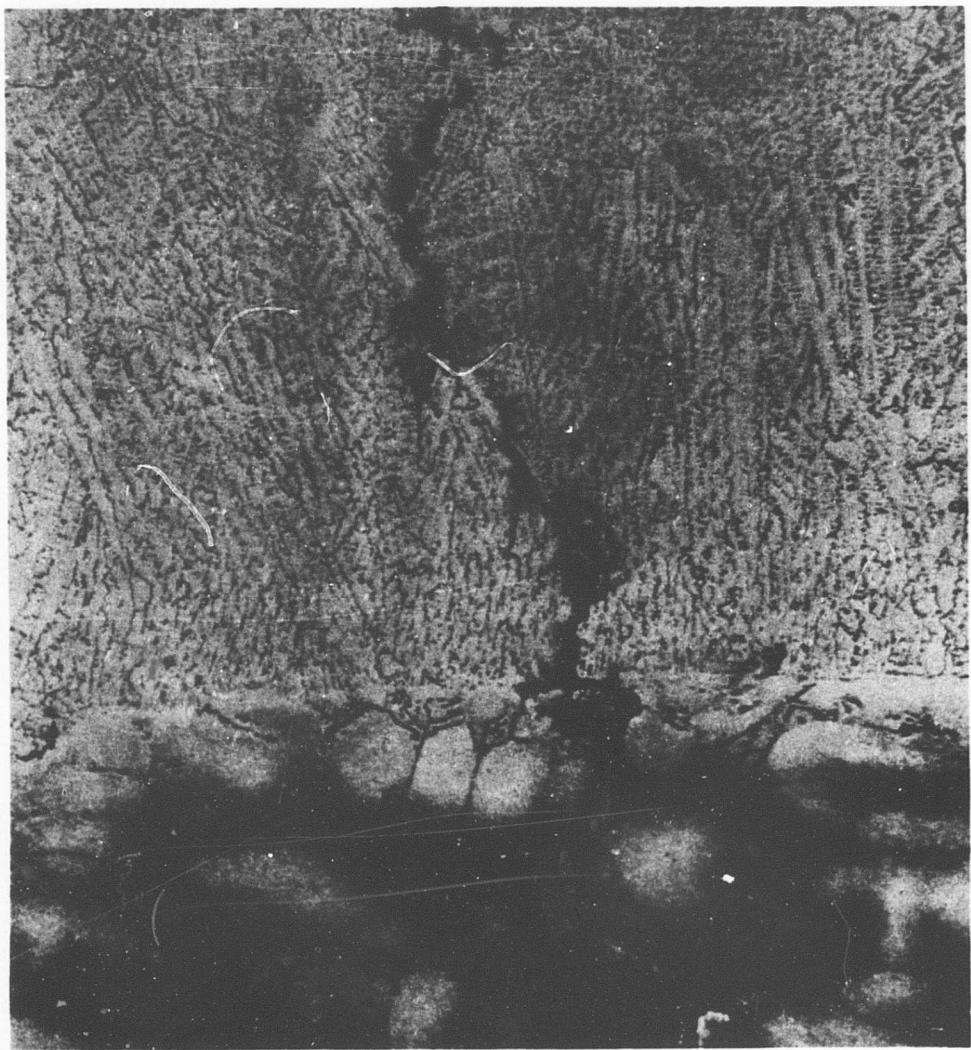


Figure 93. Photomicrograph of the Most Severe Cracking Found in an Electron-Beam-Welded Final Specimen (X100).

5.4 FINAL SPECIMEN TESTING

The final specimens were subjected to a test program that comprised tensile, stress-rupture, and low-cycle fatigue type testing at 1200°F. A description of the test procedures and a comparison of the acquired test data from the diffusion-bonded, brazed, and electron-beam-welded test specimens are presented for each type of testing in subsequent subparagraphs.

5.4.1 Tensile Testing

All tensile tests were performed in air at 1200°F by use of conventional test techniques. Specimens were brought to temperature and allowed to soak for 20 minutes prior to testing. Load was applied at a rate of 0.04 inch per minute.

Test results for the three types of final specimens are shown in Table XXI. The data indicate that the strength developed per unit of joint area is greatest for the electron-beam-welded joint and least for the diffusion-bonded joint. Total load capability was essentially equivalent for the brazed and the electron-beam-welded joints and was poorest for the diffusion-bonded joints. Both the diffusion-bonded and the brazed joints failed by shearing at the joining surfaces, as shown in Figures 94 and 95, respectively.

The electron-beam-welded specimens failed in the MAR-M 246 material adjacent to the weld zone. Figure 96 shows two typical failed electron-beam-welded specimens, and Figure 97 shows two types of fracture surfaces observed and also shows the location of the simulated cooling-air passages.

TABLE XXI. TENSILE TEST RESULTS

Joining Technique	Specimen No.	Test Temp. (°F)	Ultimate Load (lb)	Ultimate Stress (psi)
Diffusion bonding	2	1200	8350	22,100
Diffusion bonding	6	1200	5680	15,800
Diffusion bonding	9	1200	5550	15,200
Diffusion bonding	11	1200	6900	19,100
Brazing	1	1200	18,475	44,600
Brazing	2	1200	16,200	39,000
Brazing	11	1200	17,150	41,300
Brazing	20	1200	14,875	35,800
Electron-beam welding	2-3	1200	17,300	105,000
Electron-beam welding	3-3	1200	16,100	97,800
Electron-beam welding	3-4	1200	19,750	119,500
Electron-beam welding	4-6	1200	18,050	109,400
Electron-beam welding	5-5	1200	15,200	92,300

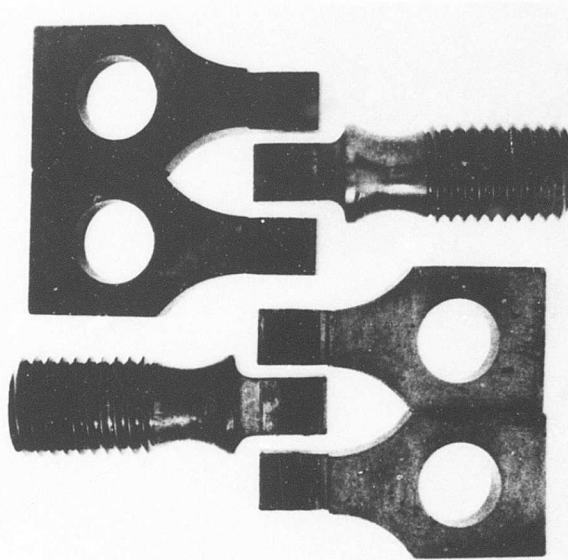


Figure 94. Tensile Failure of a Diffusion-Bonded Final Specimen.

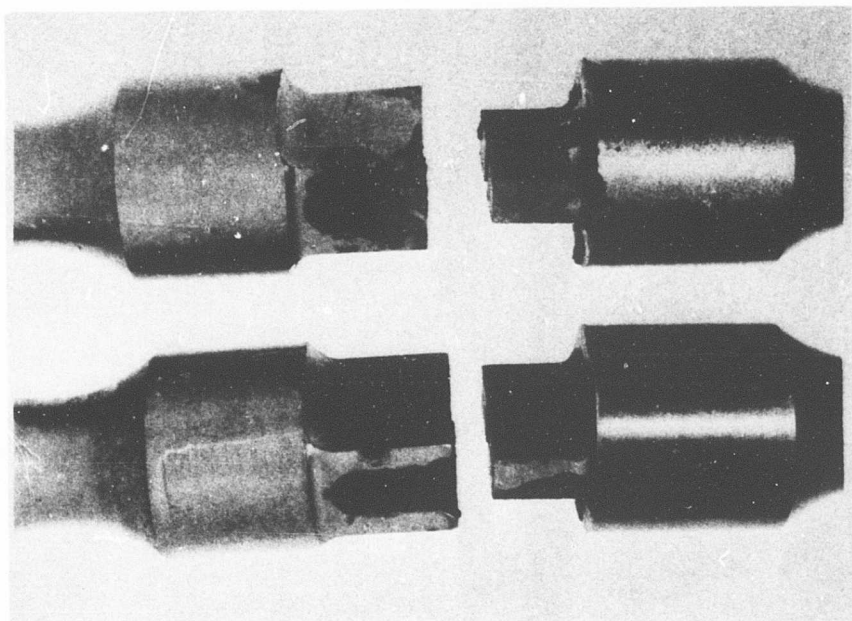


Figure 95. Tensile Failure of a Brazed Final Specimen.

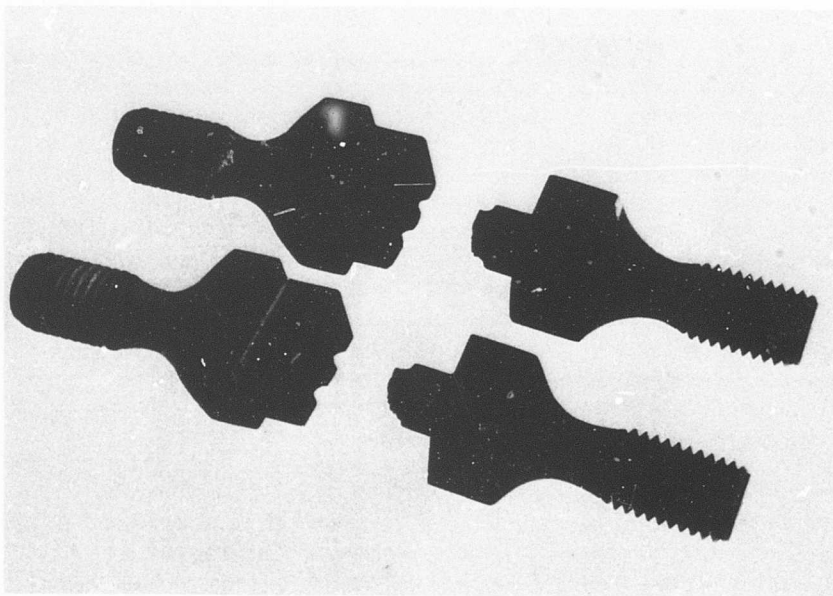


Figure 96. Tensile Failure of Electron-Beam-Welded Final Specimen.

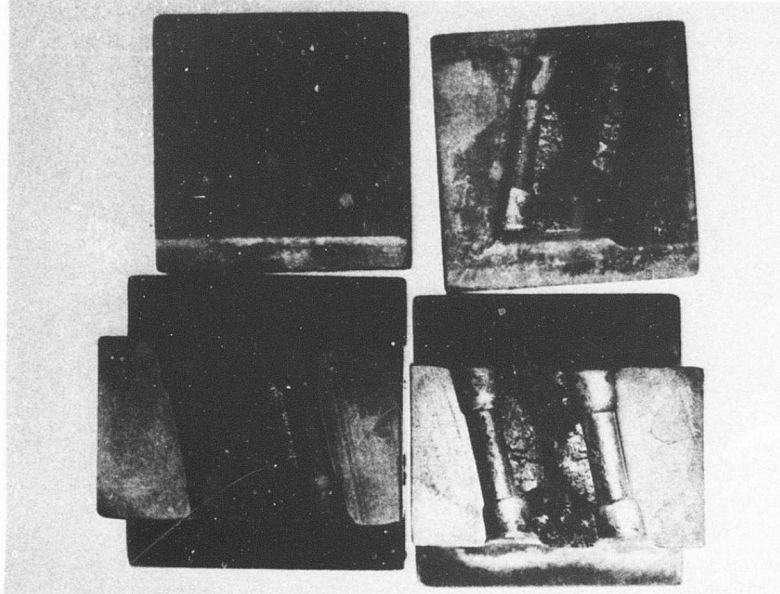


Figure 97. Fracture Surfaces of Two Electron-Beam-Welded Final Specimens Showing Variation of Fracture Appearance in Tensile Failure.

5.4.2 Stress-Rupture Testing

Stress-rupture testing was performed at 1200°F by use of conventional test techniques. Test results are tabulated in Table XXII and shown graphically in Figures 98 and 99. Figure 98 indicates that the stress-rupture strength per unit of joint area is greatest for the electron-beam-welded specimens and least for the diffusion-bonded specimens. Table XXII, however, shows the greatest inconsistency in test data to be in the electron-beam-welded data, which indicates some lack of reproducibility. The same data are plotted in Figure 99 on the basis of specimen load rather than stress. The data of Figure 99 illustrates that, for the specific specimen designs used, the welded and the brazed specimens were very nearly equivalent in their load-carrying capacity and were superior to the diffusion-bonded specimens.

Failure modes for the diffusion-bonded and the brazed specimens were identical with those observed in the tensile test specimens of Section 5.4.1. The diffusion-bonded specimens failed by shearing at the bond interface and the brazed specimens by shearing through the brazed material.

The electron-beam-welded specimens, however, showed a fracture mode differing from that observed either in the tensile or fatigue testing. Figure 100 shows an example of the typical fracture surfaces resulting from stress-rupture failures. Portions of the fracture face had a smooth appearance, with the smooth region corresponding to the Waspaloy/weld zone interface, as shown in Figure 101. This type of fracture occurred on all stress-rupture electron-beam-welded specimens regardless of the welded block from which they were machined. This indicates that the fracture was a general characteristic of the welded specimens and of the testing mode rather than of individual specimen differences.

At the test temperature of 1200°F, the MAR-M 246 material had a greater stress-rupture strength than the Waspaloy material, thus tending to force failure to occur in the Waspaloy. As a result, the actual failure appears to have originated in the heat-affected zone of the Waspaloy. The fracture followed the interface between the Waspaloy and the weld zone until it intercepted transverse cracks through the weld, after which it progressed across the weld and into the MAR-M 246 material where fracture was completed. In addition, transverse cracks terminating at the Waspaloy interface could contribute to crack initiation. This analysis indicates that the limiting factors in utilization of the electron-beam welding technique are (a) the stress-rupture strength which can be achieved in the heat-affected zone of the Waspaloy and (b) the extent that the weld cracking can be minimized.

TABLE XXII. STRESS-RUPTURE TEST RESULTS

Joining Technique	Specimen No.	Test Temp. (°F)	Load (lb)	Stress (psi)	Life (hr)
Diffusion bonding	19	1200	2500	6900	422.4+
Diffusion bonding	13	1200	3000	8300	23.0
Diffusion bonding	14	1200	3000	8300	*
Diffusion bonding	15	1200	3000	8300	*
Diffusion bonding	18	1200	3440	9500	133.0
Diffusion bonding	16	1200	4000	11,000	2.6
Brazing	6	1200	8100	15,600	400.0+
Brazing	12	1200	8240	19,900	92.6
Brazing	8	1200	7920	20,200	283.0
Brazing	19	1200	9400	22,200	91.0
Brazing	5	1200	10,300	24,800	22.3
Brazing	9	1200	11,400	27,500	14.0
Brazing	10	1200	11,400	27,500	*
Electron-beam welding	3-6	1200	13,000	78,900	18.1
Electron-beam welding	4-4	1200	13,000	78,900	900.0+
Electron-beam welding	2-6	1200	15,000	91,000	278.3
Electron-beam welding	4-3	1200	16,000	97,000	1.1
Electron-beam welding	5-4	1200	16,000	97,000	2.1**
Electron-beam welding	5-3	1200	17,000	101,500	*

*Broke on loading.

**Failed in MAR-M 246 material away from test section.
+Test discontinued--no failure.

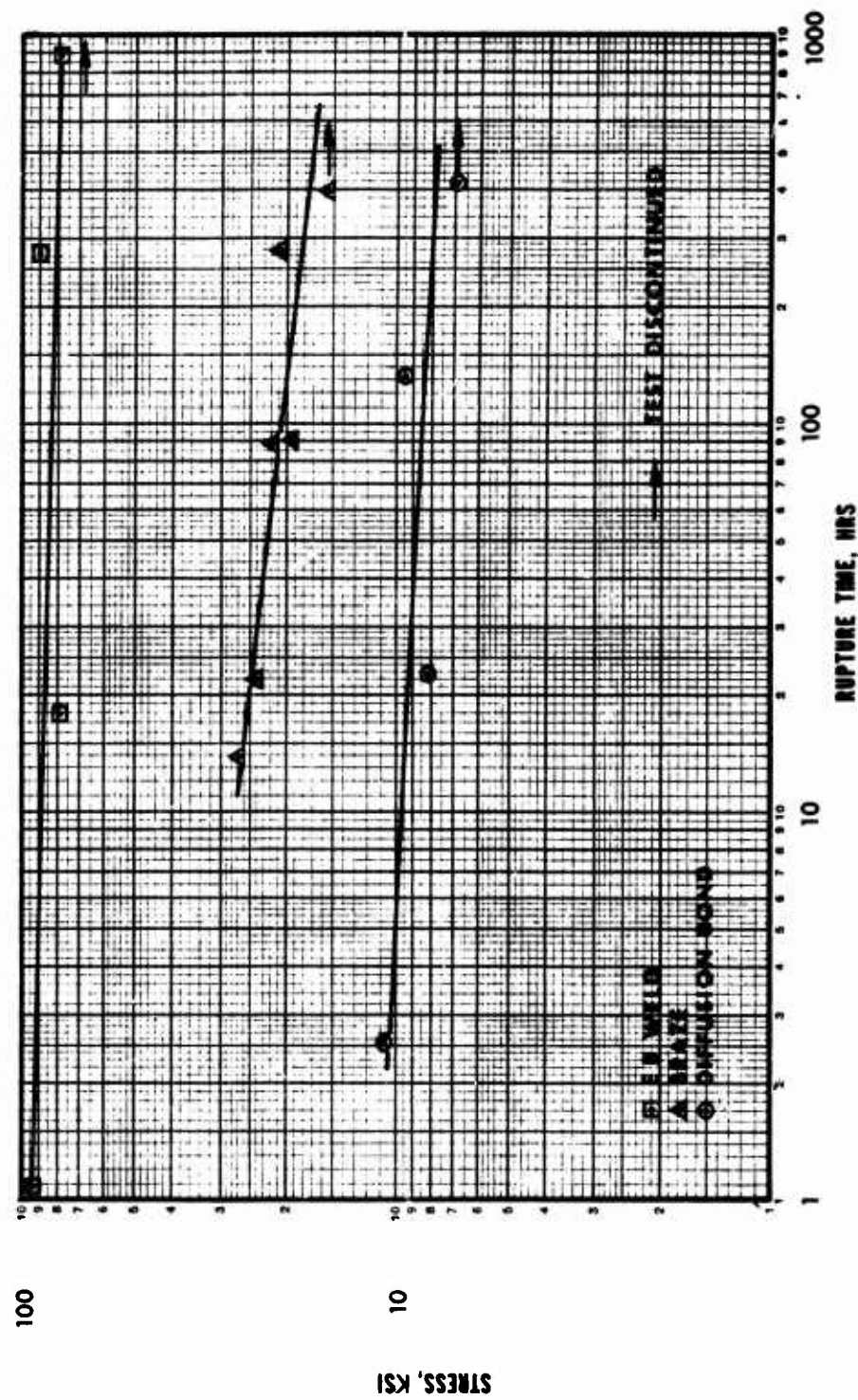


Figure 98. Stress-Rupture Data Plotted as Stress Versus Rupture Time.

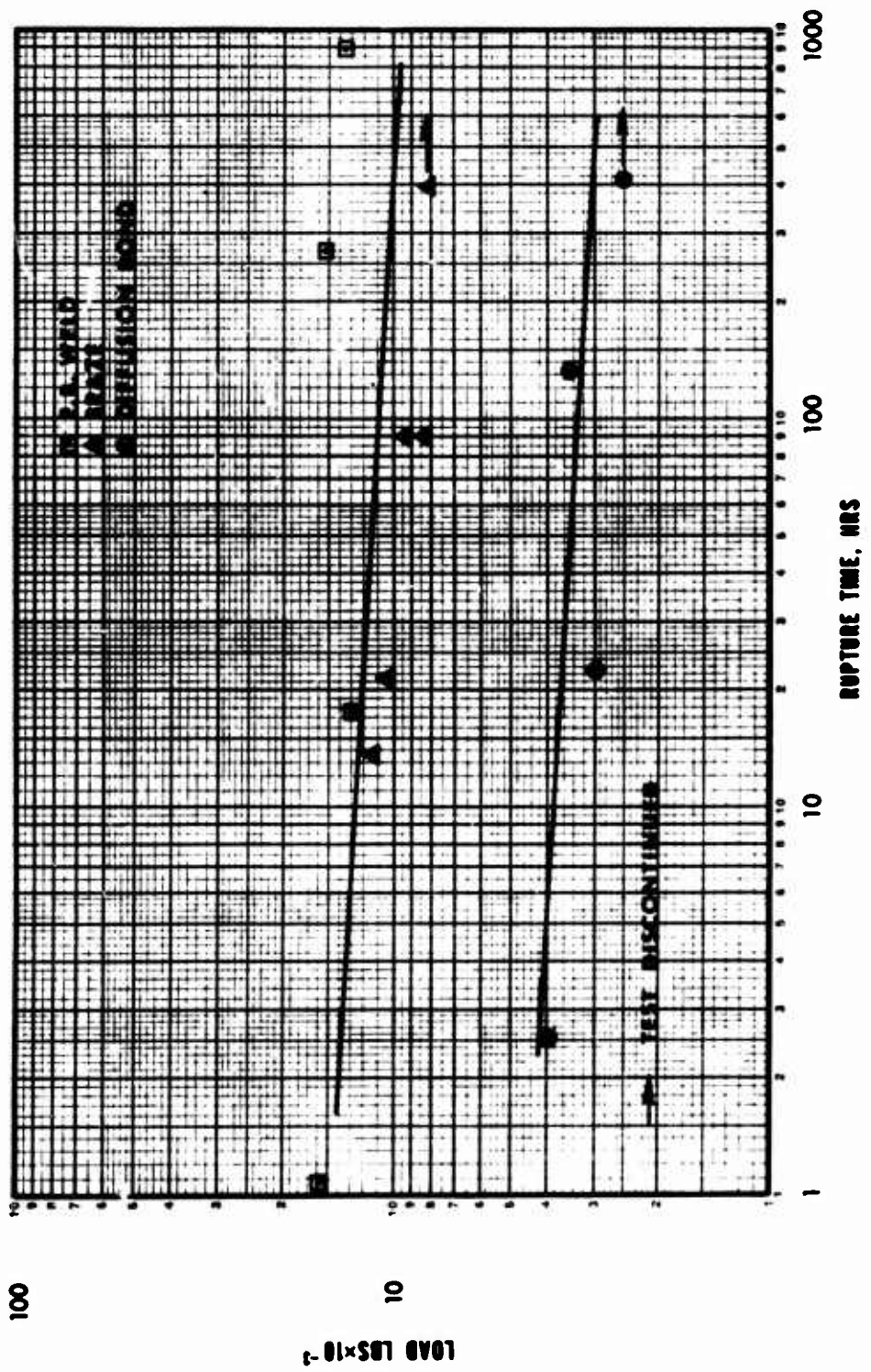


Figure 99. Stress-Rupture Data Plotted as Load Versus Rupture Time.

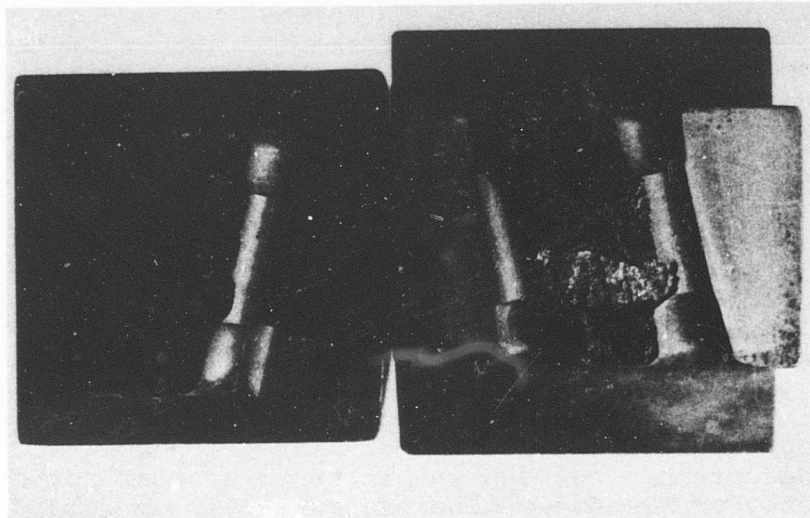


Figure 100. Typical Example of Fracture Surfaces Resulting From Stress Rupture Failure of Electron-Beam-Welded Final Specimen.

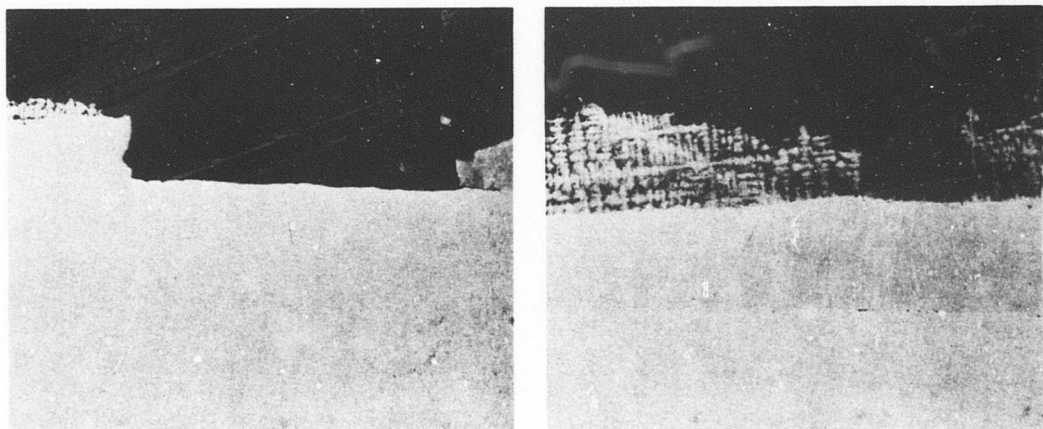


Figure 101. Stress-Rupture Failure of Electron-Beam-Welded Final Specimen Showing Smooth Fracture Face Corresponding to Waspaloy/Weld Zone Interface (X15).

5.4.3 Low-Cycle Fatigue Testing

Low-cycle fatigue testing was performed at 1200°F by the use of a closed-loop electrohydraulic test system. All loading was in tension with cycling from zero stress to the maximum stress desired and back to zero at a rate of 1000 cycles per minute.

Test data are shown in Table XXIII and are plotted in Figure 102. The best fatigue strength was shown by the electron-beam-welded specimens and the poorest by the diffusion-bonded specimens. Figure 102 shows the poor correlation of the diffusion-bonded specimens, which indicates a possible lack of reproducibility in bonding.

Failure in the diffusion-bonded specimens occurred by shearing at the bonded interface. Post-test inspection revealed no apparent differences between specimens to account for the inconsistency of the data. The brazed specimens failed, as shown in Figure 103, by fracture across either one or both of the MAR-M 246 alloy portions of the specimen. When failure occurred across only one portion, the other joining surface sheared through the braze.

In the electron-beam-welded specimens, failure occurred in the MAR-M 246 material adjacent to the weld zone. As in the case of the electron-beam-welded specimens that failed in tension, two types of fracture surfaces were observed. Figure 104 shows a relatively smooth failure as opposed to a more coarse fracture surface. No correlation could be made as to the relative strengths of specimens displaying the different fracture appearances.

TABLE XXIII. FATIGUE TEST DATA

Joining Technique	Specimen No.	Test Temp (°F)	Maximum Load (lb)	Maximum Stress (psi)	Cycles to Failure
Diffusion bonding	3	1200	4000	11,100	10,000 ⁺
Diffusion bonding	4	1200	5000	13,800	23,400
Diffusion bonding	20	1200	5250	14,500	3
Diffusion bonding	12	1200	5500	15,200	24
Diffusion bonding	5	1200	6000	16,600	107
Diffusion bonding	10	1200	6000	16,600	123
Brazing	4	1200	7500	18,000	6750
Brazing	18	1200	8000	19,200	10,400
Brazing	3	1200	8500	20,500	5265
Brazing	7	1200	9000	21,600	5175
Brazing	14	1200	10,000	24,200	3200
Brazing	13	1200	12,000	28,900	2630
Brazing	15	1200	12,500	30,200	1410
Electron-beam welding	3-2	1200	9000	54,500	36,400
Electron-beam welding	4-2	1200	9500	57,500	13,450
Electron-beam welding	2-4	1200	10,000	61,000	4600
Electron-beam welding	4-5	1200	10,500	63,800	3250
Electron-beam welding	3-5	1200	11,000	66,800	15,570
Electron-beam welding	2-5	1200	12,000	73,000	1350

⁺Test discontinued--no failure.

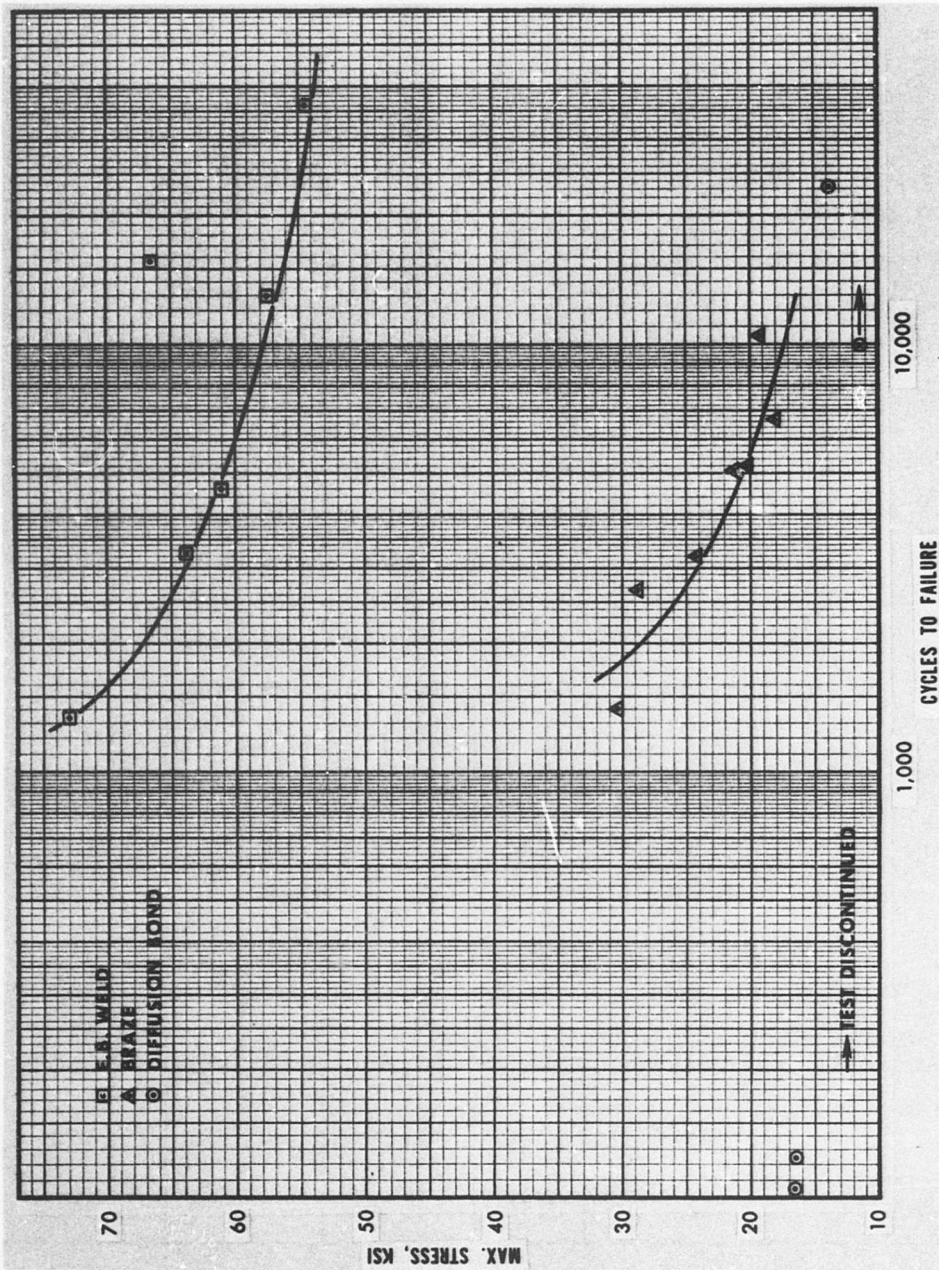


Figure 102. Low-Cycle Fatigue Failure Data for Three Types of Final Specimens.

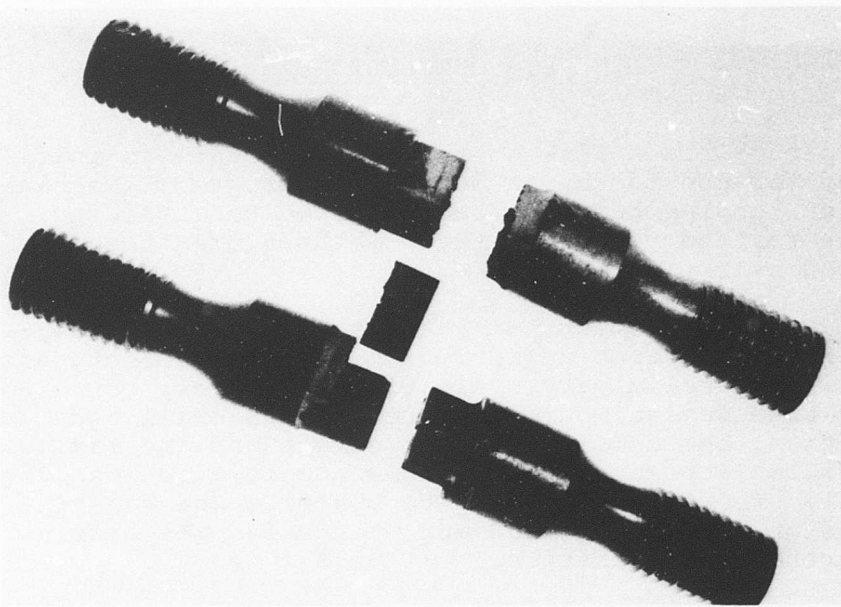


Figure 103. Two Modes of Low-Cycle Fatigue Failure of Brazed Final Specimens.

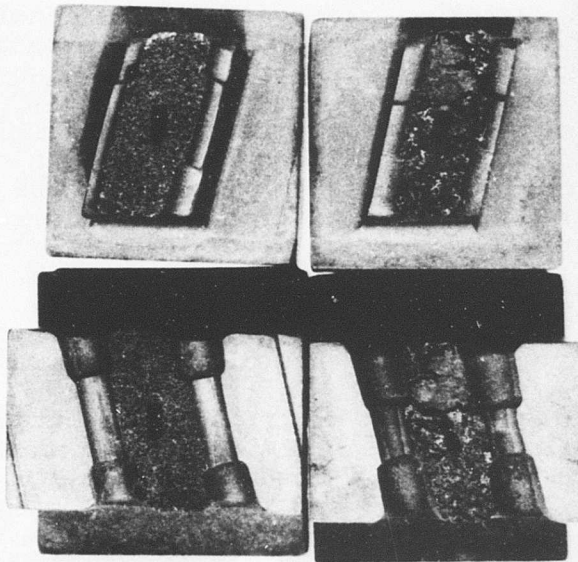


Figure 104. Low-Cycle Fatigue Failure of Electron-Beam-Welded Final Specimen--Smooth Fracture Surface is Shown on Left and Coarse Fracture Surface is Shown on Right.

6. CONCLUSIONS

Four types of blade/disk attachment methods were initially selected for consideration during the program: Mechanical, diffusion bonding, brazing, and electron-beam welding. Conclusions reached regarding these methods of attachment are presented below.

Several mechanical means of attachment were examined, and the conventional fir-tree attachment method was selected for consideration. Preliminary evaluations, however, revealed that the fir-tree design would require a large axial width disk. In addition, the combined fillet stress and the maximum combined fillet stress of the attachment elements made the design marginal. Therefore, efforts to optimize the fir-tree attachment design were terminated and the design was eliminated from further consideration.

Development and evaluation of the diffusion-bonding attachment method were pursued throughout the program. Materials used in the diffusion-bonded final test specimens were MAR-M 246 to simulate the blade pedestal element and Inconel 718 to simulate the disk. Although the diffusion-bonding attachment method offered certain advantages, it was concluded from results of the final specimen low-cycle fatigue and stress-rupture testing that this method of blade/disk attachment is inadequate. A design shear stress level of 35,000 psi appeared to be achievable on the basis of preliminary tests, but the low-cycle fatigue and stress-rupture test results indicate that only a much lower strength level could be expected. Although some probabilities exist that the 16-rms surface finish of the diffusion-bonded final specimens (selected out of consideration to the economical feasibility of the design) contributed to the reduced joint-strength properties, the low strength level of the diffusion-bonded joint and the relatively heavy disk make this approach unattractive.

Development and evaluation of the brazing attachment method were also pursued throughout the program. Materials used in the brazed final test specimens were MAR-M 246 to simulate the blade pedestal element and Waspaloy to simulate the disk. It was concluded from results of the final specimen low-cycle fatigue and stress-rupture tests that this joining method is eligible for consideration as a candidate for rotational test evaluation. Although the final tests did not reveal any dramatic improvements over the preliminary test values, the results did show that the design shear stress level of 17,500 psi is not unrealistic for the larger bonding area. At this stress, the Larson-Miller parameter (with use of a constant

of 20) would be approximately 37.5. At the maximum joint temperature of 1200°F, the corresponding rupture life would be 400 hours.

While the design goal of 1000 hours was not met, a reduction in stress level from 17,500 psi to approximately 15,000 psi would meet the design-life objective. Low-cycle fatigue life would also be satisfied, since the assumption of one start per hour (1000 starts total) could be met by a stress as high as 20,000 psi. This design concept may be modified to provide a lower shear stress in the joint by extending the joint surfaces radially inward. However, modifications of this type would add to the load carried by the disk and would further increase the axial disk dimensions. It is believed that development of a stronger brazing alloy would produce greater improvement in this design concept than geometric modifications would achieve.

Development and evaluation of the electron-beam-welding attachment method were pursued throughout the program. Materials used in the electron-beam-welded final test specimens were MAR-M 246 to simulate the blade pedestal element and Waspaloy to simulate the disk. It was concluded from results of the final specimen low-cycle fatigue and stress-rupture tests that this joining method produced a joint strength that exceeded design requirements. However, elimination of the weld joint microcracking would be necessary before this joining method could be considered for rotational test evaluation. It is possible that the stress required to propagate the cracks would be above the applied stress in a practical design; however, further testing would be required for verification. It is concluded that the design stress level in the joint of this attachment method is sufficiently below the average failure stress at 1000 hours to indicate feasibility of the design.

As a secondary effort to the blade/disk attachment activities, a preliminary evaluation was made to study the feasibility of developing a strut-supported sheet metal blade (shell/strut attachment). Joining methods that were examined included diffusion bonding, brazing, and cast bonding. Conclusions reached during the preliminary evaluation are presented below.

The diffusion-bonding concept of joining was shown to be a feasible method for consideration in shell/strut attachment. The degree of success that might be achieved by using this process would depend strongly upon the development of a bonding procedure, such as gas-pressure bonding, that would allow application of an isostatic load over the blade surface to be bonded.

The brazing concept of joining was not shown to be a desirable method for consideration in shell/strut attachment. The relatively low stress-rupture life of the existing braze alloys corresponding to the operating temperatures of the shell/strut joint make this method of joining unattractive for development considerations.

The cast-bonding concept was shown to be a feasible method for consideration in the development of a strut-supported sheet metal blade. By this method, the strut and shell/strut bonding are formed in one operation. Use of preplaced wires or cores that can be subsequently removed chemically to form cooling-air passages was shown to be a reasonable approach to pursue. Additional development would be required before this method could be used to produce scale-size specimens.

7. RECOMMENDATIONS

It is recommended that additional development and test efforts be considered for both the brazing and electron-beam-welding methods of blade/disk attachment.

For the brazing process, rotational testing of full-scale rotors is recommended to substantiate the joint strength obtained in the final specimen testing. Ultimate tensile strength can best be determined by rotor-overspeed destructive testing in a whirlpit. The low-cycle fatigue strength can be determined by rotor cyclic testing in a whirlpit. Determination of the joint-stress-rupture life can best be obtained by sectioning the rotor and subjecting the specimens to testing in a conventional creep-test machine.

For the electron-beam-welding process, research efforts to eliminate the weld joint microcracking are recommended. It is believed that this refinement would result in a substantial improvement in attachment reliability, particularly with respect to stress-rupture strength. Also, additional stress-rupture testing at reduced stress levels is recommended. If results from the additional testing revealed an improvement in the consistency of joint strength data, then full-scale rotors should be fabricated and evaluated by rotational testing as described in the preceding paragraph.

LITERATURE CITED

1. Stewart, Warner L., Whitney, Warren J., and Wong, Robert Y., A STUDY OF BOUNDARY LAYER CHARACTERISTICS OF TURBOMACHINE BLADE ROWS AND THEIR RELATION TO OVERALL BLADE LOSS, ASME Trans., J. of Basic Engr., Paper No. 59-A-23, 1959.
2. Stewart, Warner L., Glassman, Arthur J., and Vanco, Michael R., EXAMINATION OF AXIAL-FLOW TURBINE BLADE-LOADING CHARACTERISTICS USING DIFFUSION PARAMETERS, ASME PAPER 67-WA/GT-8, March 1967.
3. Zweifel, O., THE SPACING OF TURBOMACHINE BLADING, ESPECIALLY WITH LARGE ANGULAR DEFLECTION, The Brown Boveri Review, Vol. 436, Decimal Index 621-226.2, December 1945.
4. Whitney, Warren J., Stewart, Warner L., and Miser, J.W., EXPERIMENTAL INVESTIGATION OF TURBINE-STATOR-BLADE OUTLET BOUNDARY LAYER CHARACTERISTICS AND COMPARISON WITH THEORETICAL RESULTS, NACA RM E55K24, Washington, D.C., March 1956.
5. Monson, S.S., DIRECT METHOD OF DESIGN AND STRESS ANALYSIS OF ROTATING DISKS WITH TEMPERATURE GRADIENT, NACA Report 952, Washington, D.C., 1950.

APPENDIX
LITERATURE SURVEY

A survey was made of Government agencies and technical literature to review existing blade/disk attachment methods and to evaluate current technology apropos to: (a) material types and property strength of superalloys, (b) rotor fabrication technology, (c) mechanical attachment methods, and (d) material joining processes, including welding techniques, brazing, and diffusion bonding. The survey was conducted in parallel with the aerothermodynamic design activity.

Recent activities devoted specifically to blade attachment problems were found to be primarily concerned with space power applications. The inherent design differences of the space power components from the subject turbine are such that most of the technology evaluated was not useful to the blade/disk problems encountered in this program.

A considerable amount of technical literature was found that described fabrication techniques, various joining processes, and methods of joint strength testing. This information was useful in the mechanical design, fabrication, and test activities of this program.

Some of the more pertinent publications directly applicable to the diffusion-bonding, brazing, and electron-beam-welding attachment methods that were evaluated during this program are listed by category on the following pages.

DIFFUSION BONDING

Kaarlela W. T., and Margolis, W. S., ALLOY EFFECTS IN THE LOW PRESSURE DIFFUSION BONDING OF SUPERALLOYS, General Dynamics Corporation, Fort Worth, Texas; Welding Journal 48th, Detroit, Michigan, April 1967, Supplement Vol. 46, June 1967, pp 282-288.

King, J. P. Jr., Roberlotto, R. B., and Dillingham, A. C. Jr., DIFFUSION BONDING OF TITANIUM AND BERYLLIUM, North American Rockwell Corporation, Air Force Systems Command, Wright-Patterson Air Force Base, Ohio, Technical Report AFML-TR-67-388, December 1967.

Cogan, R. M., DEVELOPMENT OF A MANUFACTURING PROCESS FOR FABRICATED DIFFUSION HOLLOW BLADES, Aircraft Engine Group, General Electric Company, Cincinnati, Ohio; Advanced Fabrication Techniques Branch, Manufacturing Technology Division, Air Force Materials Laboratory, Air Force Systems Command, Wright Patterson Air Force Base, Ohio, Contract AF33615-68-C-1215, Project No. IR-883-8(1), February and May 1968.

Meiners, Kenneth E., GAS-PRESSURE AND THERMONAC DIFFUSION BONDING AT BATTELLE COLUMBUS LABORATORIES, Materials Development Division, Battelle Memorial Institute, unpublished.

Crane, C. H., and Lovell, D. F., DIFFUSION WELDING OF DIS-SIMILAR METALS, Welding Journal, Vol. 46, No. 1, January 1967.

Obrrut, J. J., DIFFUSION WELDING--THE QUEST FOR PERFECT JOINTS, Iron Age Metalworking, Vol. 4, No. 8, August 1965.

Orrok, Neale E., APPLICATION OF DIFFUSION BONDING, Metal Progress Vol. 89, No. 6, June 1966.

BRAZING

Smeltzer, D. E., Malik, R. K., Hammer, A. N., and Compton, W. A., DEVELOPMENT OF JOINING PROCESSES FOR TITANIUM FOILS, Solar Division of International Harvester Company; Air Force Materials Laboratory, Research and Technology Division, Air Force Systems Command, Wright-Patterson Air Force Base, Ohio, Technical Report AFML-TR-67-305, Vols. I and II, September 1967.

BRAZING AND BRAZING ALLOYS, A Report Bibliography, NASA SP-5026, Washington, D. C., 1967.

Schwartz, M. M., BRAZING BREAKTHROUGH JOINS REFRACTORY HONEYCOMB, Tool Manufacturing Engineer, Vol. 58, No. 3, March 1967, pp 33-35.

King, E. J., EFFECT OF GE 8100 BRAZE ALLOY ON THE PROPERTIES OF HAYNES 25 AND INCONEL 702, Bell Aerosystem Laboratory Report BLR 63-4(M), Buffalo, N. Y., March 1963.

THE SOUNDNESS AND STRENGTH OF HIGH-TEMPERATURE VACUUM-BRAZED JOINTS, The British Non-Ferrous Metals Research Association, Report A.1249, London, England, September 1959.

HIGH-TEMPERATURE STRESS-TO-RUPTURE PROPERTIES OF BRAZED JOINTS IN HEAT-RESISTING ALLOYS, The British Non-Ferrous Metals Research Association, Report A.1250, London, England, September 1959.

BRAZE LAP JOINTS AT HIGH TEMPERATURE, A Report Bibliography,
ARB NO. 067955, Arlington, Virginia, 1967.

ELECTRON-BEAM WELDING

Beer, R., FABRICATION OF LIGHTWEIGHT TURBINE COMPONENTS USING ELECTRON BEAM WELDING FOR THE ATTACHMENT OF SHEET METAL BLADES TO DISKS AND SHROUDS, Aerojet-General Corporation, Sacramento, California, Report No. NASA CR-54814, AGC8800-49, Contract No. NAS3-2555, Washington, D. C., October 1966.

Lubin, Barry T., A CORRELATION OF ELECTRON BEAM WELDING PARAMETERS, Dynatech Corp., Cambridge, Massachusetts, ASME Paper 66-WA/MET-18, 1967.

Engquist, R. D., PARAMETERS AFFECTING ELECTRON BEAM WELDING, ASM Metals Park, Ohio, Tech. Report No. C7-19.2, 1967.

Miller, K. J., ELECTRON AND LASER BEAM WELDING, ASM Metals Park, Ohio, ASTME WES-54, 1967.

Wiffen, E. L., ELECTRON BEAM WELDING, Mach and Tool Blue Book, Vol. 61, December 1966, pp 109-111.

Fletcher, M. J., ELECTRON BEAM WELDING, Engl. Elect. J., Vol. 20, No. 5, September-October 1965, pp 15-20.

BRAZE LAP JOINTS AT HIGH TEMPERATURE, A Report Bibliography,
ARB NO. 067955, Arlington, Virginia, 1967.

ELECTRON-BEAM WELDING

Beer, R., FABRICATION OF LIGHTWEIGHT TURBINE COMPONENTS USING ELECTRON BEAM WELDING FOR THE ATTACHMENT OF SHEET METAL BLADES TO DISKS AND SHROUDS, Aerojet-General Corporation, Sacramento, California, Report No. NASA CR-54814, AGC8800-49, Contract No. NAS3-2555, Washington, D. C., October 1966.

Lubin, Barry T., A CORRELATION OF ELECTRON BEAM WELDING PARAMETERS, Dynatech Corp., Cambridge, Massachusetts, ASME Paper 66-WA/MET-18, 1967.

Engquist, R. D., PARAMETERS AFFECTING ELECTRON BEAM WELDING, ASM Metals Park, Ohio, Tech. Report No. C7-19.2, 1967.

Miller, K. J., ELECTRON AND LASER BEAM WELDING, ASM Metals Park, Ohio, ASTME WES-54, 1967.

Wiffen, E. L., ELECTRON BEAM WELDING, Mach and Tool Blue Book, Vol. 61, December 1966, pp 109-111.

Fletcher, M. J., ELECTRON BEAM WELDING, Engl. Elect. J., Vol. 20, No. 5, September-October 1965, pp 15-20.

Unclassified

Security Classification

DOCUMENT CONTROL DATA - R & D

(Security classification of title, body of abstract and indexing annotation must be entered when the overall report is classified)

1. ORIGINATING ACTIVITY (Corporate author) The AiResearch Manufacturing Company of Arizona, 402 S. 36 St. Phoenix, Arizona		2a. REPORT SECURITY CLASSIFICATION Unclassified
		2b. GROUP
3. REPORT TITLE AN INVESTIGATION OF TURBINE BLADE/DISK ATTACHMENT METHODS FOR SMALL, COOLED GAS TURBINES		
4. DESCRIPTIVE NOTES (Type of report and inclusive dates) Final Report		
5. AUTHOR(S) (First name, middle initial, last name) J. L. Helmbrecht, R. F. Kirby, and F. Weber		
6. REPORT DATE January 1970	7a. TOTAL NO. OF PAGES 184	7b. NO. OF REFS 5
8a. CONTRACT OR GRANT NO. DAAJ02-68-C-0119	9a. ORIGINATOR'S REPORT NUMBER(S) USAAVLABS Technical Report 69-91	
b. PROJECT NO. Task 1G162203D14413	9b. OTHER REPORT NO(S) (Any other numbers that may be assigned this report) AiResearch assigned number, PE-8031-R	
c.		
d.		
10. DISTRIBUTION STATEMENT This document is subject to special export controls, and each transmittal to foreign governments or foreign nationals may be made only with prior approval of US Army Aviation Materiel Laboratories, Fort Eustis, Virginia 23604		
11. SUPPLEMENTARY NOTES	12. SPONSORING MILITARY ACTIVITY US Army Aviation Materiel Laboratories Fort Eustis, Virginia	
13. ABSTRACT This report describes the analytical, experimental, and developmental efforts that were conducted to design, fabricate, test, and evaluate turbine-rotor blade to rotor disk (blade/disk) attachment methods for an air-cooled turbine rotor in a small gas turbine engine. This investigation was launched because the combination of factors that are necessary to satisfy the design requirements of a small cooled gas turbine has made it increasingly difficult to utilize conventional blade attachment means. Specifically, the program was directed toward achieving a suitable attachment method for an axial turbine with an inlet temperature of 2400°F, an airflow rate of 4.0 lb/sec, a tip speed of 1500 ft/sec, and matched to a compressor having a 10:1 pressure ratio. Detail aerothermodynamic design activities were conducted to determine a turbine design that would provide optimum specific fuel consumption (SFC) and specific horsepower (sp hp). The design included an optimization study to obtain the best compromise of turbine efficiency, cooling geometry, blade and disk stress effects, and fabrication considerations. Detailed mechanical design activities were conducted in parallel with fabrication technology development efforts to establish the materials, designs, joining methods, and fabrication techniques necessary to determine feasible means of blade/disk attachment. Results of these activities showed that diffusion-bonding, brazing, and electron-beam-welding blade/disk attachment methods possess the greatest potential for application in the subject turbine design. A secondary purpose of the mechanical design and fabrication development activities was to study the feasibility of developing the strut-supported sheet metal blade (shell/strut attachment) that was revealed by the aerodynamic optimization study to be the most effective blade cooling configuration. Full evaluation of the shell/strut attachment was beyond the scope of this program; however, it was determined that both diffusion-bonding and cast-bonding concepts of joining could be considered as feasible methods to develop for the purpose of shell/strut attachment. A final fabrication and test activity was conducted to complete evaluations of the three blade/disk attachment methods. Final specimens were designed, fabricated, inspected, and subjected to tensile, stress-rupture, and low-cycle fatigue testing at 1200°F. Evaluation of the final specimen test results revealed that (a) the diffusion-bonding method of joining was unsatisfactory for blade/disk attachment due to insufficient joint strength, (b) the brazing method of joining produced a joint strength approaching design requirements and could be considered as a candidate method for rotational test evaluation, and (c) the electron-beam-welding method of joining produced a joint strength that exceeded design requirements. Further evaluation will be necessary to resolve microcracking in the weld joint before rotational test evaluations can be considered.		

DD FORM 1 NOV 64 1473 REPLACES DD FORM 1473, 1 JAN 64, WHICH IS
OBsolete FOR ARMY USE.**Unclassified**

Security Classification

Unclassified

Security Classification

14. KEY WORDS	LINK A		LINK B		LINK C	
	ROLE	WT	ROLE	WT	ROLE	WT
Turbine Blade/Disk Attachment Brazing Diffusion Bonding Electron-Beam Welding Sheet Metal Blade/Strut Attachment Cast Bonding						

Unclassified

Security Classification

222-70